

A Nano-Stepping Robotic Instrumentation Platform

by

Adam Joseph Wahab

B.Eng., McGill University (2006)

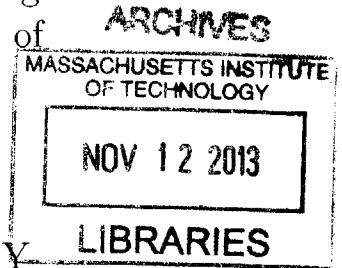
S.M., Massachusetts Institute of Technology (2008)

Submitted to the Department of Mechanical Engineering
in partial fulfillment of the requirements for the degree of

Doctor of Philosophy in Mechanical Engineering

at the

MASSACHUSETTS INSTITUTE OF TECHNOLOGY



August 2013
[SEPTEMBER 2013]

© Massachusetts Institute of Technology 2013. All rights reserved.

Author

Department of Mechanical Engineering

August 27, 2013

Certified by

Ian W. Hunter

Hatsopoulos Professor of Mechanical Engineering

Thesis Supervisor

Accepted by

David E. Hardt

Chairman, Department Committee on Graduate Theses

A Nano-Stepping Robotic Instrumentation Platform

by

Adam Joseph Wahab

Submitted to the Department of Mechanical Engineering
on August 27, 2013, in partial fulfillment of the
requirements for the degree of
Doctor of Philosophy in Mechanical Engineering

Abstract

The development of an Autonomous Nano-stepping Tool (ANT) system is presented. Each ANT is a small, tripodal, robotic instrument capable of untethered precision motion within a quasi-three-dimensional workspace of arbitrary size. The project aimed to address limitations of conventional benchtop micro/nanoscale measurement and manipulation systems by offering a low-cost, scalable alternative with comparable performance and extended functionality and flexibility. The design, fabrication, and evaluation the various electrical, mechanical, and software subsystems are discussed. Device prototypes are introduced along with a platform-agnostic interface for remote monitoring and control. The device step size and its frequency dependence are examined. A novel, high-resolution capacitive probe concept is detailed and characterized as an example of an inexpensive, low-power, sensor technology with which an ANT may be equipped to perform scanning probe microscopy. Several positioning schemes are discussed, including a distributed vision-based approach which utilized a custom cross-correlation processor.

Thesis Supervisor: Ian W. Hunter

Title: Hatsopoulos Professor of Mechanical Engineering

Acknowledgments

The author wishes to express his most heartfelt appreciation to his thesis advisor, Professor Ian W. Hunter, for providing the opportunity to be a member of the MIT BioInstrumentation Laboratory - a truly unique and world-class facility. Prof. Hunter has been generously supportive of the author's curious nature, providing freedom to explore and experience in realms of science and engineering beyond those that were directly related to this work.

The author's thesis committee, which also includes Professor Martin L. Culpepper and Professor Derek Rowell, has provided precious guidance, patience, and insight that has proven invaluable.

The author is indebted to his parents, Randy and Maret Wahab, and his brother, Matthew, for their unmatched patience and support, and without whom, none of this would have been possible.

Endless thanks are due to Kate Melvin, Administrative Assistant II, for being so very helpful, upbeat, and dependable.

Thanks are also owed to Leslie Regan, Administrator for the MIT Department of Mechanical Engineering's Graduate Office, who, on more than one occasion, has done all but bend the laws of physics on the author's behalf.

Dr. Cathy Hogan, Senior Research Scientist and friend, has been instrumental in making the author's experience in the BILab so pleasant by providing advice, support, and entertainment.

A special round of thanks are to be distributed equally among Dr. Dan Burns, Aaron Gawlik, Dr. Brian Hemond, and Kasia Piotrowska for providing much mirth and ensuring that the author's humanity remained largely intact.

The author also wishes to acknowledge financial assistance provided by Natural Sciences and Engineering Research Council of Canada (NSERC), the Intelligence Advanced Research Projects Activity (IARPA) and the Massachusetts Institute of Technology-Singapore University of Technology and Design (MIT-SUTD) alliance, whose funds covered costs incurred throughout the hardware development process.

THIS PAGE INTENTIONALLY LEFT BLANK

Contents

| | | |
|----------|---------------------------------------|-----------|
| 1 | Introduction | 17 |
| 1.1 | Motivation | 18 |
| 1.2 | Microrobots & Applications | 20 |
| 2 | Design | 25 |
| 2.1 | Micro/Nano-Stepping | 25 |
| 2.1.1 | Gaits | 25 |
| 2.1.2 | Stick-Slip Mechanics | 26 |
| 2.1.3 | Piezoelectric Actuators | 32 |
| 2.1.4 | Analytical Deflection Model | 34 |
| 2.2 | Subsystems | 38 |
| 2.2.1 | Core Subsystem | 38 |
| 2.2.2 | Locomotion Subsystem | 40 |
| 2.2.3 | Communication Subsystem | 43 |
| 2.2.4 | Instrumentation Subsystem | 44 |

| | | |
|----------|----------------------------------|-----------|
| 3 | Prototype Development | 45 |
| 3.1 | Mark I | 45 |
| 3.2 | Mark II | 47 |
| 3.3 | Mark III | 50 |
| 3.4 | Mark IV | 53 |
| 3.5 | Mark V | 57 |
| 4 | Stepping Characteristics | 63 |
| 4.1 | Apparatus | 63 |
| 4.2 | Measurement Procedure | 65 |
| 4.3 | Results | 65 |
| 5 | Control and Monitoring | 69 |
| 5.1 | Firmware | 69 |
| 5.2 | Motion Primitives | 69 |
| 5.3 | Communication Protocol | 71 |
| 5.4 | Heading Estimation | 73 |
| 5.5 | Server-Side Hardware | 73 |
| 5.6 | Server | 74 |
| 5.7 | User Interface | 75 |
| 5.7.1 | Joystick | 77 |

| | | |
|----------|--|------------|
| 5.7.2 | Plotting | 77 |
| 6 | Instrumentation Example: Capacitive Probe | 79 |
| 6.1 | Probe Fabrication | 79 |
| 6.2 | Measurement Electronics | 80 |
| 6.3 | Evaluation | 81 |
| 7 | Positioning | 87 |
| 7.1 | Positioning Systems | 87 |
| 7.2 | Centralized Positioning | 87 |
| 7.2.1 | Position Sensitive Device | 88 |
| 7.2.2 | Digital Imaging Sensor | 91 |
| 7.3 | Distributed Positioning | 93 |
| 8 | Conclusions | 101 |
| 8.1 | Contributions | 101 |
| 8.2 | Next Steps: Considerations for Future Work | 102 |
| A | Tapped Inductor Boost Converter | 107 |
| B | Linear Actuator | 109 |
| B.1 | Lorentz Force Linear Motor | 109 |
| C | ANT Revision 1K Schematic | 111 |

List of Figures

| | | |
|------|---|----|
| 2-1 | Stick-slip locomotion involves lifting, pushing (stick), and sliding (slip). | 26 |
| 2-2 | Circular contact subjected to a steady normal load P_o and an oblique force F . Load distribution A corresponds to the case without slip, while B corresponds to the case where slip occurs in the annulus $c \leq r \leq a$. Adapted from [27]. | 28 |
| 2-3 | A leg undergoing transverse deflection; the step size is approximately equal to the projection of the deflection amplitude onto the stepping surface. | 33 |
| 2-4 | The BVD model for a piezoelectric element. | 33 |
| 2-5 | Simulated frequency response of the BVD impedance model displaying first resonance. | 35 |
| 2-6 | Deflection of a piezoelectric tube scanner subjected to an excitation potential applied to one of its four outer electrodes. | 35 |
| 2-7 | Simulation results depicting the first six resonant modes of a scanning tube (PZT-5H) terminated with a spherical element (aluminum oxide). | 37 |
| 2-8 | Frequency response of the unloaded leg assembly as predicted by numerical model. | 38 |
| 2-9 | Map of ANT subsystems. | 39 |
| 2-10 | Tapped-inductor boost converter. | 41 |
| 2-11 | (a) A cascaded transistor high voltage switching circuit. (b) The same circuit realized using a monolithic load switch IC. | 42 |

| | | |
|------|---|----|
| 3-1 | Assembled Mark I prototype. | 46 |
| 3-2 | Leg mounting jig. | 48 |
| 3-3 | Mark 2 flex PCB prior to final assembly. | 49 |
| 3-4 | Mark II prototype. | 50 |
| 3-5 | Mark III rigid-flex PCB assembly. | 51 |
| 3-6 | Mark III prototype. | 52 |
| 3-7 | Mark IV rigid PCB assembly prior to final assembly stage. | 54 |
| 3-8 | Revised leg mounting jig. | 55 |
| 3-9 | Mark IV prototype. | 56 |
| 3-10 | Mark V rigid-flex assembly prior to folding. | 57 |
| 3-11 | Mark V prototype with a capacitive probe is shown mounted on the bottom chassis apex. | 58 |
| 3-12 | Mass distribution for Mark V prototype. Total measured mass was 0.0142 kg. | 59 |
| 3-13 | Breakdown of component costs for Mark V prototype. Total cost was \$525 (USD). | 60 |
| 3-14 | Approximate distribution of average power consumption during continuous stepping. The total power draw was 1.245 W. | 61 |
| 4-1 | Optical measurement apparatus used for determining both leg deflection and step size. Red arrows depict the laser path. | 64 |
| 4-2 | Measured frequency response of an unloaded leg subjected to single electrode excitation. | 66 |
| 4-3 | Measured body displacement during uni-axial stepping. | 67 |
| 4-4 | Average step size as a function of frequency for a range of excitation voltages. | 67 |

| | | |
|-----|--|----|
| 5-1 | USB radio dongle (20 mm × 45 mm). From left to right: micro-USB port, USB-to-UART converter, microcontroller, radio transceiver, and chip antenna. | 74 |
| 5-2 | ANT network structure. | 74 |
| 5-3 | A screen capture of the ANTS UI. Basic status and control registers and the manual control joystick are visible. | 76 |
| 5-4 | The ANTS UI plotting section allows users to easily monitor multiple asynchronous data streams in real-time. New canvas layers were dynamically generated as additional data streams are added. Notice how each layer was updated independently as new data is pushed from the server to the client. | 78 |
| 6-1 | Cross-sectional representation of capacitive probe illustrating the layered construction. | 80 |
| 6-2 | Apparatus for characterizing the capacitive probe microscope. Red arrows depict the laser path, blue arrows indicate the motion axes. | 82 |
| 6-3 | Measured edge response. | 83 |
| 6-4 | Computed resolution of a capacitive probe based on 10%-90% criterion. | 84 |
| 6-5 | Computed line spread function. | 84 |
| 6-6 | Computed line spread function. | 85 |
| 7-1 | Proposed approaches for position measurement. | 88 |
| 7-2 | A gantry system that was constructed to explore the use of a PSD for two-dimensional positioning. | 90 |
| 7-3 | The scan path used for mapping the relationship between the two PSD voltage output channels and absolute position within the workspace. | 90 |
| 7-4 | Spatial plots of normalized PSD amplifier output voltages (a) V_x and (b) V_y | 92 |

| | | |
|------|---|-----|
| 7-5 | The pixel-by-pixel shifting process that occurs when computing the cross-correlation.. | 93 |
| 7-6 | An overview of the FPGA subsystems and signal flow. Note that the “Binarize” process is shown in grey, as it may be omitted for implementations where increased dynamic range and resolution are required. | 95 |
| 7-7 | A 8-bit pipelined cross-correlation processor design. | 97 |
| 7-8 | The binary cross-correlation pipeline, wherein expensive multipliers and adders have been replaced by AND gates and population counters. | 97 |
| 7-9 | An $N \times N$ pixel frame and $M \times M$ pixel template shown with offset $u = v = 0$, corresponding with the start of a new cross-correlation computation. | 98 |
| 7-10 | Imaging system hardware prototype (20 mm \times 50 mm). The camera module is located on the far right-hand side of the PCB. The FPGA is located on the reverse side, directly opposite the camera. | 99 |
| A-1 | Characteristic time series representations of primary inductor current i_p and voltage V_p and secondary inductor current i_s and voltage V_s during a single switch cycle at steady state. Adapted from [28]. | 108 |
| B-1 | Simulation results depicting the magnetic flux for a potential actuator geometry: C-frame (4 mm \times 5 mm \times 2 mm), cylindrical NdFeB magnet (N42, ϕ 1.5 mm). The left-hand side illustrated the flux density when a 100 mA current is passed through the coil. | 110 |
| B-2 | A collection of experimental coils wound to test various fabrication techniques and examine feasibility. The leftmost two coils were wound with 150 μ m diameter wire, while the two on the right were wound with 50 μ m diameter wire. A ϕ 1.5 mm permanent magnet is included on the left-hand side for scale. | 110 |
| C-1 | Microcontroller, oscillator, and LEDs. | 111 |

| | | |
|-----|---|-----|
| C-2 | Switching regulators and load switches. | 112 |
| C-3 | Radio transceiver. | 112 |
| C-4 | IMU, I ² C switch, CDC, and regulator. | 113 |
| C-5 | PCB module interconnects. | 113 |
| C-6 | High voltage switches and piezoelectric load connections. | 114 |

THIS PAGE INTENTIONALLY LEFT BLANK

List of Tables

| | | |
|-----|--|----|
| 1.1 | A qualitative comparison of several major efforts for developing microrobotic instruments. | 21 |
| 5.1 | ANT configuration and data registers. | 70 |
| 5.2 | Communication packet structure. | 71 |
| 5.3 | Network address assignment. | 72 |
| 5.4 | Data packet payload structure. | 72 |
| 5.5 | ANT protocol commands, where Node A and Node B represent two devices running the ANT firmware. | 73 |
| 7.1 | Camera output signals. | 95 |

THIS PAGE INTENTIONALLY LEFT BLANK

Chapter 1

Introduction

The design and development of a miniature robotic instrument capable of performing precision positioning and measurement tasks is presented. Chapter 1 summarizes motivating factors that served as driving elements for this body of work along with the project vision. Pertinent background information regarding the development microrobotic instruments and applications thereof are also provided. Chapter 2 focuses on the design methodology, with both high-level and detailed descriptions of the device architecture and its key subsystems. Chapter 3 introduces several of the completed hardware prototypes, highlighting incremental refinements and culminating in a final device variant that is characterized in Chapter 4. Several schemes to enable closed-loop position control are described in Chapter 7, accompanied by preliminary designs for associated hardware. A platform-independent framework for control and monitoring tasks, along with a touch-enabled user interface are presented in Chapter 5. Lastly, Chapter 8 contains some concluding remarks summarizing key developments that have resulted from this project, as well as thoughts and suggestions directed at any future development efforts.

1.1 Motivation

The field of microrobotics has evolved as an attempt to sidestep many of the limitations imposed by conventional laboratory instrumentation, related to: (i) maximum sample size, (ii) throughput capacity, (iii) cost, and (iv) ease of use.

Maximum Sample Size Generally, samples are transported to a benchtop instrument for analysis or processing. Such instruments typically have workspaces that limit the maximum sample size, potentially requiring a user to destructively remove an appropriately-sized section. Inversion of this classic paradigm introduces a different scenario, wherein a user would instead transport the instrument to their sample – for example, instances where a user wishes to inspect portions of a silicon wafer or a multi-well plate as an intermediate processing step. An implication of the aforementioned paradigm shift is that the instrument be made sufficiently small and portable¹ in order to be manageable.

Throughput Sufficiently compact microrobotic devices may alleviate so-called “mechanical congestion”, where the number of concurrent operations within a given workspace is limited by the size of an instrument’s probe(s) or positioning mechanism. One can imagine a scenario where microrobotic instruments are operating cooperatively to measure the change in conductivity of a length of conducting polymer nanowire held taut between two devices as they also quantify the stress-strain characteristics. Situations like the former are not feasible with conventional positioning systems (*e.g.*, cartesian arrangements of linear stages).

Microrobotic devices may also be used to produce scalable instruments. Multiple microrobotic AFMs may operate within the footprint of a conventional benchtop microscope, concurrently imaging sections of a large sample or perhaps a range of different samples.

¹The reduction in device size may, in turn, allow for greater flexibility, giving rise to new usage scenarios. One example being a microrobotic manipulator operating inside the confinements of an scanning electron microscope (SEM) imaging chamber.

Cost More often than not, conventional benchtop instruments are often prohibitively expensive for small companies, educational institutions, and individuals alike. Lower capital costs translate into a lower barrier-to-entry and greater accessibility.

The matter of cost extends beyond actually obtaining instruments. Precision machines often include recurring costs, such as regular maintenance and occasional recalibration. Proprietary software required for instrument use may need periodic updates or mandate that the user pay recurring licensing fees. Enabled, in part, by the commoditization of integrated electronics and MEMS technologies, financially tractable meso- and microscale instruments may be realized with capabilities that meet or exceed those of their conventional counterparts. Low cost instruments may be disposed of and replaced should they become contaminated or irreparably damaged.

Ease of Use Sophisticated laboratory instruments often rely upon a proprietary software interface for controlling hardware and collecting data. Referencing years of experience training graduate and undergraduate to how to operate a variety of scientific instruments, the author will attest to the unintuitive design of most provided software provided by instrument manufacturers and the resulting negative impact it has on productivity.

The closed nature of proprietary software is often limiting. Users may not be granted a means to access configurable system parameters, effectively quenching prospects of exploratory applications that tend to arise in research laboratories. In many cases, users create custom software, which interfaces with hardware via manufacturer provided device drivers and APIs. Instrument software may cease to function following required updates to operating systems and third-party software. Manufacturers may be acquired, go out of business, or simply cease development efforts, resulting in termination of software support. Loss of software support usually signifies the start of a countdown towards an instrument's end of life.

Instrument manufacturers occasionally opt to develop software for a single platform (*i.e.*, Microsoft® Windows), when in reality professionals and students in all fields of science and engineering use veritable cornucopia of different operating systems (*e.g.*, UNIX® derivatives such as various flavors of Linux and Apple® OS X). Developing instrument software for a single platform creates a number

of potential obstacles for end-users, who must, in turn, make compromises. Purchase of an additional computer and/or operating system license may be necessary, increasing both system cost and hardware space requirements. An instrument may be purchased for subsequent integration with an existing system, the latter of which may use another platform, thus likely requiring costly design modifications.

Research and development is inherently difficult enough; tools destined for research laboratories and educational institutions should be designed to meet the needs of end-users and support their efforts, rather than forcing the reverse.

1.2 Microrobots & Applications

Although the idea of using micro/nano-stepping robots as a precision instrumentation platform is not new, success has often been curbed by technological and design limitations. Early development of miniature mobile robotic manipulators was motivated by the need to precisely manipulate samples under vacuum inside of a scanning electron microscope (SEM) [11, 32, 44] without requiring modifications to the stock chamber design.

Other efforts were spurred by the notion of replacing conventional macroscale systems used for nanoscale operations with swarms of mesoscale, autonomous robots, each equipped with interchangeable instruments and manipulators [37]. This approach, it was thought, would alleviate many of the limitations of existing systems, such as mechanical congestion resulting from the inherent bulk of macroscale machine components. The desire to produce instruments that were both versatile and scaleable was yet another source of motivation. Multiple robotic instruments could operate independently, performing tasks either in parallel, or cooperatively within workspaces of more or less arbitrary size. A qualitative comparison of several prominent efforts is provided in Table 1.1.

Size and mobility are key factors when considering microrobotic instruments. Smaller devices allow for greater instrument density, or more devices per unit of workspace area, potentially leading to


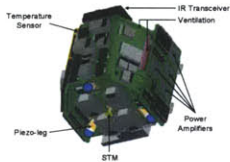


| Project | Years | Size | Mobility | Power |
|--|-----------|---|---|-------------------|
| MINIMAN [44]  | 1997–2002 | Large $84 \text{ mm} \times 75 \text{ mm} \times 40 \text{ mm}$ | Fast 30 mm s^{-1} Holonomic | Tether |
| NanoWalker [32]  | 1999–2005 | Mid-size $32 \text{ mm} \times 32 \text{ mm} \times 30 \text{ mm}$ | Fast $10\text{--}200 \text{ mm s}^{-1}$ Holonomic | Electrified Floor |
| MiCRoN [39]  | 2002–2005 | Small $12 \text{ mm} \times 12 \text{ mm} \times 12 \text{ mm}$ | Slow 0.2 mm s^{-1} Non-holonomic | Inductive Floor |
| I-SWARM [25]  | 2004–2008 | Small $3 \text{ mm} \times 3 \text{ mm} \times 2 \text{ mm}$ | Slow 0.3 mm s^{-1} Non-holonomic | Photovoltaic |

Table 1.1: A qualitative comparison of several major efforts for developing microrobotic instruments.

greater overall system throughput.

Mobility, referring to device speed and holonomicity, is just as critical. Fast, holonomic devices are able to spend less time positioning themselves and more time performing useful measurement and manipulation tasks, resulting in greater overall system throughput.

Yet another important consideration is how a device is to be powered. External power sources permit longer periods of operation than are attainable by devices utilizing on-board energy storage. Although a 100% duty cycle would help maximize potential system throughput, external power sources can be complex, costly, and have even been found to impose limits on system flexibility.

Piezoelectric materials are well suited for generating micro- and nano-stepping motions required for miniature robotic instruments [14, 23]. One attractive characteristic of piezoelectrics is their ability to generate small scale displacements from voltages that are large, resulting in an favorable signal-to-noise ratios (SNR). Furthermore, piezoelectric actuators have extremely high bandwidths allowing for thousands of cycles per second resulting in average stepping speeds on the order of $1 \times 10^2 \text{ mm s}^{-1}$. Additionally, piezoelectric actuators do generate magnetic fields, which may be unacceptable in certain applications (*e.g.*, manipulation of a sample within an SEM). All four of the projects compared in Table 1.1 use piezoelectric actuators, but exhibit a great deal of variation in size and mobility.

Legged microrobotic devices like the ones considered here may be considered as derivatives of the so-called Besocke-style scanning mechanism [13]. Besocke scanners consist of a circular plate supported by three piezoelectric scanning tubes, arranged 120° apart and terminated with sapphire or glass spheres. Excitation potentials cause the tubes to bend, imparting translational and rotational movements to the plate. However, unlike microrobotic devices, Besocke-style scanners are purpose-built stationary devices offering only a limited range of motion.

Some prior efforts experienced limited success on account of various subsystem integration issues and/or performance deficiencies. The majority of problems were closely linked to decisions made throughout the design process, rather than the underlying concept of using micro robotics for a given application.

In many ways, the ANTs project was a reimagining of the NanoWalker project, which was originated in the MIT BioInstrumentation Laboratory, with an emphasis on simplicity, integration, and efficiency. The NanoWalker design boasted an attractive balance between size and mobility. The device’s high speed resulted from both its pyramidal leg configuration, which increased the amount of lateral thrust produced when stepping, and its use of high voltages to drive the piezoelectric legs, producing large steps. It was also holonomic – capable of instantly rotating or translating in any direction within the plane. In addition to unmatched mobility, the NanoWalker was the only miniature robotic device of its size with sophisticated on-board data processing capabilities. Unfortunately, the high rates of travel and multiple onboard processors came with a price as typical power consumption was between 10 W to 30 W ²; values that are prohibitively high for operation from any practically-sized battery for a useful amount of time³. A special electrified surface was then developed to provide the NanoWalkers with sufficient power via conductive feet [31]. This approach created a number of new problems, such as arcing between the feet and surface and posing limitations on sample compatibility, requiring they be made of nonconductive materials sized to fit entirely beneath the NanoWalker so as not to interfere with the electrical contacts. The need for a specialized work surface greatly reduced overall system flexibility whilst increasing both cost and complexity.

Inefficient electronics were primarily responsible for the NanoWalker’s high power consumption. Aside from mobility considerations, several watts of heat generated in a volume roughly the size of a golf ball will inevitably lead to precision and reliability issues. Heating of structural and mechanical components may lead to unacceptable degradation of precision due to thermal expansion. Sensitive electronic components may suffer from significant thermal drift and noise or perhaps even fail outright. To address these concerns, a thermal management solution was adopted after the project moved from MIT to the University of Montréal: the workspace and devices were placed inside of a cryogenic cooling chamber [30, 33], further increasing complexity and cost while drastically decreasing system flexibility.

Instead of focusing on thermal management, a simpler solution might entail designing efficient

²Ideally, a 0.1 kg robot would only consume 0.02 W when traveling at a rate of 200 mm s⁻¹ under its own power.

³For 10 minutes of runtime from a lithium ion cell: (10 W)(600 s) = 6000 J. (6000 J)/(500 kJ kg⁻¹) = 0.012 kg. (6000 J)/(830 MJ m⁻³) = 7.230 × 10⁻⁶ m³.

electronics that generate less heat. Lower power dissipation equates to less power required to operate, obviating the need for an external power source and an elaborate cooling infrastructure, and resulting in greater system flexibility.

Considering the challenges encountered by the NanoWalker team, and bearing in mind the shortcomings of conventional benchtop instrumentation, a set of three core functional requirements were defined to which the ANT development efforts would adhere to: efficiency, autonomy, and low-cost.

Chapter 2

Design

The development of the mechanical and electrical systems to support untethered locomotion served as the project's primary design focus.

2.1 Micro/Nano-Stepping

2.1.1 Gaits

In the context of this work, we refer to a distinct stepping mode that results from a predefined sequence of input commands as a gait. Legged microrobotic devices that are capable of micro- and nanoscale motions typically utilize gaits that rely upon the stick-slip principle [22, 49]. Figure 2-1 illustrates key phases that comprise the stick-slip locomotion used by ANTs, wherein a lateral view of a tripodal device is shown translating from left-to-right. The device starts from a statically stable initial position with three points of contact with the work surface. An instant later, the front leg lifts, whilst the rear legs push the center of mass (located at the apex of the three legs) forward – the *stick* phase. The inertia of the body prevents the device from immediately falling forward on account of its now statically unstable configuration. Yet another instant later, the frontmost leg is lowered, and the rear two legs are accelerated forward to their original position with respect to the

body – the *slip* phase.

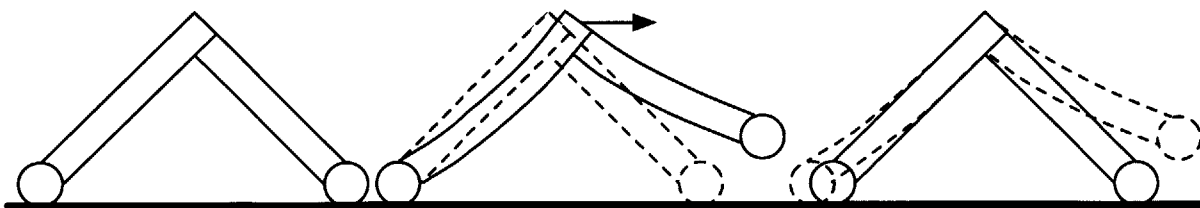


Figure 2-1: Stick-slip locomotion involves lifting, pushing (stick), and sliding (slip).

2.1.2 Stick-Slip Mechanics

The nonlinear frictional behavior exhibited at the foot-surface interface is described by the stick-slip phenomenon [49]. For small amplitude perturbations, corresponding to behavior in the stick regime, the lateral friction F_{lat} applied a foot undergoing lateral displacement $u(t)$ may be approximated by the Kelvin-Voight model. That is to say, a linear spring and Newtonian dashpot connected in parallel may be used to describe the in-plane contact forces between the foot and surface and the dissipative forces resulting from air resistance, respectively. Displacements in excess of that which corresponds to the the maximum static friction force F_o defined by the foot-surface interface will result in slip motion. In the slip regime, lateral friction may be approximated by a constant.

Mathematically, the aforementioned frictional loading may be expressed by the following piecewise relationship

$$F_{\text{lat}} = \begin{cases} K_{\text{lat}}u(t), & |u| < u_o \\ F_o, & |u| \geq u_o, \end{cases} \quad (2.1)$$

where K_{lat} is the lateral contact stiffness of the foot-surface interface, and u_o is the critical displacement corresponding to F_o . The value of K_{lat} depends on the contact radius a and the shear contact modulus G^* . For the case of Hertzian contact between a sphere of radius R and plane, we have

$$K_{\text{lat}} = 8aG^*, \quad (2.2)$$

and

$$a^3 = KP, \quad (2.3)$$

where $K = \frac{3R}{4E^*}$ and P is the static normal preload at the foot-surface interface. ANTs are supported by three legs, so we may define static normal preload P_o for each foot-surface interface as one third of device weight, *i.e.*,

$$P_o = \frac{1}{3}mg, \quad (2.4)$$

where m is the total device mass, and g is the acceleration due to gravity, which is assumed to be normal to the surface. The corresponding contact radius may then be denoted by a_o and defined by (2.3). The maximum static friction and static normal preload are related by the coefficient of friction μ , such that $F_o = \mu P_o$. The contact modulus of elasticity E^* and shear modulus G^* are defined in terms of the moduli of elasticity, shear moduli, and Poisson's ratios of the foot (1) and surface (2) as

$$E^* = \left(\frac{1 - \nu_1^2}{E_1} + \frac{1 - \nu_2^2}{E_2} \right)^{-1} \quad (2.5)$$

and

$$G^* = \left(\frac{2 - \nu_1}{G_1} + \frac{2 - \nu_2}{G_2} \right)^{-1}. \quad (2.6)$$

In the absence of slip, the traction, or shear load, may be taken as radially symmetric and everywhere parallel to the plane of the surface:

$$q_x(r) = q_o \left(1 - \frac{r^2}{a^2} \right)^{-1/2}, \quad (2.7)$$

where $q_o = \frac{Q_x}{2\pi a^2}$, with Q_x being the total instantaneous shear load. The no slip scenario only serves as a boundary case, since it would require shear loads to approach infinity along the contact circle periphery. To provide a more realistic model, we begin by accounting for the presence of micro-slip.

At the onset of sliding, the shear load distribution would take the form

$$q'(r) = \mu p(r) = \mu p_o \left(1 - \frac{r^2}{a^2} \right)^{1/2}, \quad (2.8)$$

for $r \leq a$. Prior to sliding, both stick and slip regions may coexist within the area of contact; the stick region being confined to a circle of radius c , and an annular region of micro-slip extending from $c \leq r \leq a$. In the absence of any external oblique forces, the shear load distribution within the stick region may be described as

$$q''(r) = -\frac{c}{a} p_o \left(1 - \frac{r^2}{c^2}\right)^{1/2}. \quad (2.9)$$

The radius of the stick region c may be expressed in terms of the total shear load Q_x :

$$\begin{aligned} Q_x &= \int_0^a 2\pi q'(r)rdr - \int_0^c 2\pi q''(r)rdr, \\ &= \mu P \left(1 - \frac{c^3}{a^3}\right). \end{aligned} \quad (2.10)$$

Rearranging (2.10), we obtain

$$\frac{c}{a} = \left(1 - \frac{Q}{\mu P}\right)^{1/3}, \quad (2.11)$$

which relates the non-slip contact radius to the applied normal and shear loads.

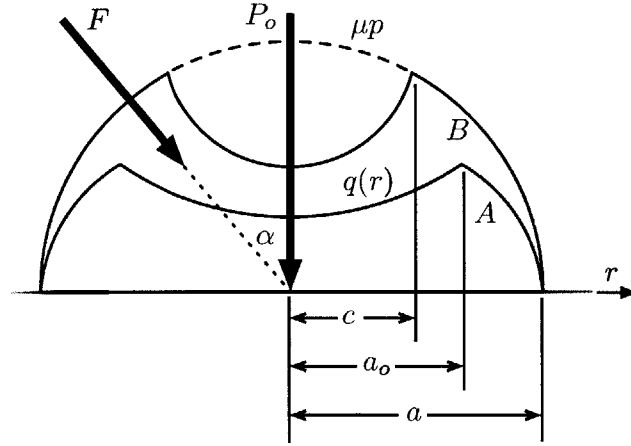


Figure 2-2: Circular contact subjected to a steady normal load P_o and an oblique force F . Load distribution A corresponds to the case without slip, while B corresponds to the case where slip occurs in the annulus $c \leq r \leq a$. Adapted from [27].

Stepping, introduces an additional force component F , which results from the deflection of the piezoelectric legs as they push the center of mass in a commanded direction. This oblique force acts

at an angle α with respect to the surface normal, as shown in Figure 2-2, incrementally contributing to the normal and shear loads as $dP = dF \cos \alpha$ and $dQ = dF \sin \alpha$, respectively. The contact radius, in turn, increases by an amount da , which may be found by differentiating (2.3):

$$\begin{aligned} 3a^2 da &= K dP, \\ &= K \frac{dQ}{\tan \alpha}. \end{aligned} \quad (2.12)$$

Similarly, an expression for the incremental change in traction may be obtained by differentiating (2.7):

$$dq(r) = \frac{dQ}{2\pi a} (a^2 - r^2)^{-1/2}. \quad (2.13)$$

Substituting (2.12) into (2.13) and integrating with respect to a yields expressions for the the shear load distribution $q(r)$ for a given contact radius a_1 :

$$q(r) = \begin{cases} \frac{3 \tan \alpha}{2\pi K} \left[(a_1^2 - r^2)^{1/2} - (a_0^2 - r^2)^{1/2} \right], & 0 \leq r \leq a_0 \\ \frac{3 \tan \alpha}{2\pi K} (a_1^2 - r^2)^{1/2}, & a_0 \leq r \leq a_1. \end{cases} \quad (2.14)$$

The normal pressure distribution is given in accordance with the Hertz theory as

$$\begin{aligned} p(r) &= \frac{3 (P_o + F \cos \alpha)}{2\pi a_1^3} (a_1^2 - r^2)^{1/2}, \\ &= \frac{3}{2\pi K} (a_1^2 - r^2)^{1/2}. \end{aligned} \quad (2.15)$$

In order for slip to occur, the shear load $q(r)$ must exceed the static friction $\mu p(r)$, thus a no slip condition arises when $\tan \alpha \leq \mu$. Consequently, a load that is mostly vertical does not give rise to micro-slip within the contact region, and results in a shear load distributions $q(r)$ that is similar to curve *A* in Figure 2-2.

Application of force at an angle that exceeds the angle of friction results in the formation an annular slip region at the edge of the circle of contact. The shear load distribution in this case would appear similar to curve *B* in Figure 2-2, where $q(r)$ follows an upper limit of $\mu p(r)$ throughout most of the contact region. The radial position of the annular slip region's inner boundary (and outer boundary

of the circular stick region) is determined by equilibrium of the shear loads. Invoking (2.11) and rearranging provides the following

$$1 - \frac{c^3}{a^3} = \frac{F \sin \alpha}{\mu (P_o + F \cos \alpha)}, \quad (2.16)$$

where we have rewritten the shear load Q and normal loads P in terms of F and P_o . In the limit as $c \rightarrow 0$, full sliding results, which would correspond to an oblique load of

$$F_{\text{slide}} = \frac{\mu P_o}{\cos \alpha (\tan \alpha - \mu)}. \quad (2.17)$$

The relative lateral displacement δ_x between the foot and surface due to partial slip may be estimated by¹

$$\delta_x = \frac{3\mu P}{16G^*} \left(\frac{a^2 - c^2}{a^3} \right), \quad (2.18)$$

noting that (2.11) may be substituted for c .

To obtain a rough estimate of the energy required to execute a single step cycle, we will consider the stick and slip phases separately. We begin by constraining our analysis to pure translation in the direction of one of the three piezoelectric legs, such that, during the stick phase, the foremost leg lifts whilst the two rear legs push forward.

Assuming that the leg excitation waveforms have been tuned such that the resulting dynamic thrust load F is less than F_{slide} , the total mechanical energy requirement is the sum of: (i) forward motion of the device mass m , (ii) losses within the piezoelectric material, and (iii) micro-slipping at the foot-surface interface, or

$$E_{\text{in}} = E_{\text{m}} + E_{\text{piezo}} + E_{\mu\text{slip}} + E_{\text{slide}}, \quad (2.19)$$

where E_{in} is the energy provided by the power electronics less any electrical inefficiencies, E_{m} is the useful work performed in moving the center of mass forward, E_{piezo} accounts for energy losses within the leg material, and $E_{\mu\text{slip}}$ is energy associated with micro-slipping, and E_{slide} represents energy dissipated through full-on sliding.

¹See [27] for a full derivation.

Considering a device mass m of 150 mg, undergoing a displacement of 1 μm , fitted with piezoelectric tubes with an efficiency of $\eta_{\text{piezo}} = 50\%$ and excited near their resonant frequency of 1 kHz. The Poisson's ratios and moduli of elasticity and rigidity are taken as $\nu_1 = 0.3$, $E_1 = 3.5$ GPa, $G_1 = 172.4$ GPa for a ruby foot[41] and $\nu_2 = 0.3$, $E_2 = 98$ GPa, and $G_2 = 64.1$ GPa for a silicon wafer surface [18]. The coefficient of friction at the foot-surface interface is taken to be $\mu = 0.3$. The pyramidal configuration of the legs results in an oblique force angle of approximately $\alpha = 35^\circ$.

Given the above parameter values, the energy required to move the body mass would be on the order of $E_m \approx 0.6$ μJ . Inefficiencies in the two active piezoelectric legs would roughly double the amount of energy required, thus $E_{\text{piezo}} \approx 0.6$ μJ . The energy associated with deformation of the walking surface may be approximated as the product of $F \sin \alpha$ and (2.18); for two legs, we have $E_{\mu\text{slip}} \approx 4.3$ nJ. Substituting the computed values into (2.19), provides a rough estimate of $E_{\text{in}} \approx 1.2$ μJ required during the stick phase.

During the slip phase, the foremost leg contacts the work surface and the rear legs move forward. We consider the interaction between the rear two feet and surface to be that of pure sliding and may assume that the rear legs move forward passively. That is to say, the legs return to their undeflected position using only energy stored during the stick phase and without any addition energy input by the power electronics. For the purpose of this analysis, we neglect the presence of hysteresis introduced by the both the piezoceramic material and the foot-surface interactions.

From (2.17) we may estimate the energy associated with the two rear legs passively sliding forward as being $E_{\text{slide}} \approx 0.9$ μJ . As mentioned, the legs are sliding using stored mechanical energy, so $E_{\text{piezo}} \approx 0$. We may also neglect the energy associated with micro-slip at the foremost foot-surface interface, thus we take $E_{\mu\text{slip}} \approx 0$.

Summing the above, we find that the resulting total energy balance becomes

$$E_{\text{in}} = E_{\text{m},1} + E_{\text{piezo},1} + E_{\mu\text{slip},1} + E_{\text{slide},1} - (\eta E_{\text{piezo},1} - E_{\text{slide},2}), \quad (2.20)$$

where subscripts 1 and 2 indicate if a term is associated with the stick or slip phase, respectively. Substituting in the above numerical quantities, we find that the net Energy required to perform

a single stepping cycle is approximately 1.8 μJ . The stepping cycle efficiency may then be estimated as the ratio of the energy required to move the body mass forward to the total energy required. Substituting our estimated values we find that the projected stick-slip stepping efficiency is approximately 0.33%.

2.1.3 Piezoelectric Actuators

As previously mentioned, stepping motions are produced using piezoelectric scanning tubes as legs. In this section, we briefly examine some of the electrical and mechanical models that were used to match the drive electronics with the leg material and geometry.

As one might expect, the stepping performance of a legged robot depends on a number of geometric parameters associated with a given leg design. A diagram indicating several key parameters is provided in Figure 2-3. The thin-walled, tubular leg has a circular cross-section and is terminated with a spherical foot. We assume that the body mass, situated at the top of the leg, is sufficiently large so as to provide an approximately fixed boundary condition. The step size δs may then be approximated as the projection of the foot displacement δx normal to the leg's center axis that results from a unilateral transverse deflection. For a given excitation potential, increasing the leg's length L , while decreasing the diameter d and wall thickness h will produce larger step sizes but may result in undesirable structural compromises, such as a reduction in load bearing capacity and overall device rigidity.

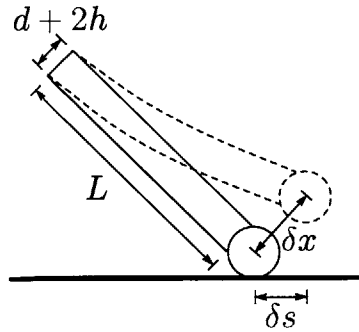


Figure 2-3: A leg undergoing transverse deflection; the step size is approximately equal to the projection of the deflection amplitude onto the stepping surface.

Electrical Impedance Model

A model of the electrical load presented by the piezoelectric tubes was developed prior to designing the drive electronics. The response of a piezoelectric material varies as a function of both the excitation voltage frequency and amplitude.

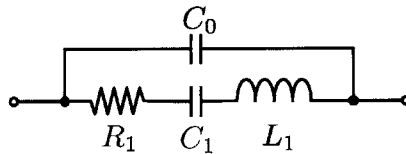


Figure 2-4: The BVD model for a piezoelectric element.

An equivalent circuit model may be used to represent the electrical impedance characteristics of a piezoelectric element and its mechanical load. The Butterworth–Van Dyke (BVD) model [1, 29], shown in Figure 2-4, is often employed as a simple means of representing the electrical behavior of a piezoelectric ceramic subjected to resonant excitation. The model consists of a capacitor C_0 connected in parallel with a resistor R_1 , capacitor C_1 , and inductor L_1 that are connected in series. C_0 represents the static, or DC, capacitance of the element’s dielectric material and any external connections. The RCL network serves as a lumped model of the motional behavior of the piezoelectric element and its load. At resonance, the C_1 and L_1 reactances cancel, leaving just

R_1 to represents the losses in the element and load. The BVD model impedance $Z_{\text{BVD}}(s)$ may be expressed using the following transfer function:

$$Z_{\text{BVD}}(s) = \frac{1}{C_0 s} \frac{C_1 L_1 s^2 + R_1 C_1 s + 1}{C_1 L_1 s^2 + R_1 C_1 s + 1 + \frac{C_1}{C_0}}. \quad (2.21)$$

Suitable values for the model parameters may be obtained by computing the nonlinear least-squares fit to measurements of a given tube's electrical impedance as a function of frequency (*i.e.*, the nonparametric frequency response function). A piezoelectric scanner tube (PZT-5H; $d = 2.5$ mm, $h = 0.5$ mm, $L = 25$ mm) was connected to an impedance analyzer (Hewlett Packard[®] HP 4194A) via leads soldered to the inner electrode and one of the four outer electrodes. A frequency sweep was performed over a range from 0.1 kHz to 100 kHz, which was found to be approximately centered on the tube's first resonant frequency. The resulting impedance gain and phase data were then used to compute the following equivalent circuit values were computed for the BVD model parameters: $C_0 = 2.5$ nF, $R_1 = 11.7$ k Ω , $C_1 = 128.4$ pF, and $L_1 = 1.68$ H. The first resonance from a simulated frequency response of (2.21) using the above parameter values is shown in Figure 2-5. It is desirable to operate piezoelectric elements near resonance in order to minimize power dissipation and maximize electro-mechanical coupling.

A lower bound estimate for the current draw for a given excitation voltage $v(t)$ may then be obtained by substituting fitted parameter values back into (2.21) and deconvolving:

$$I(s) = \frac{V(s)}{Z_{\text{BVD}}(s)}, \quad (2.22)$$

where $V(s)$ denotes the Laplace Transform of $v(t)$ (*i.e.*, $\mathcal{L}\{v(t)\}$).

2.1.4 Analytical Deflection Model

Numerous analytical models are available to describe the mechanics of piezoelectric tubes undergoing deflections resulting from an applied excitation potential [10, 16, 19].

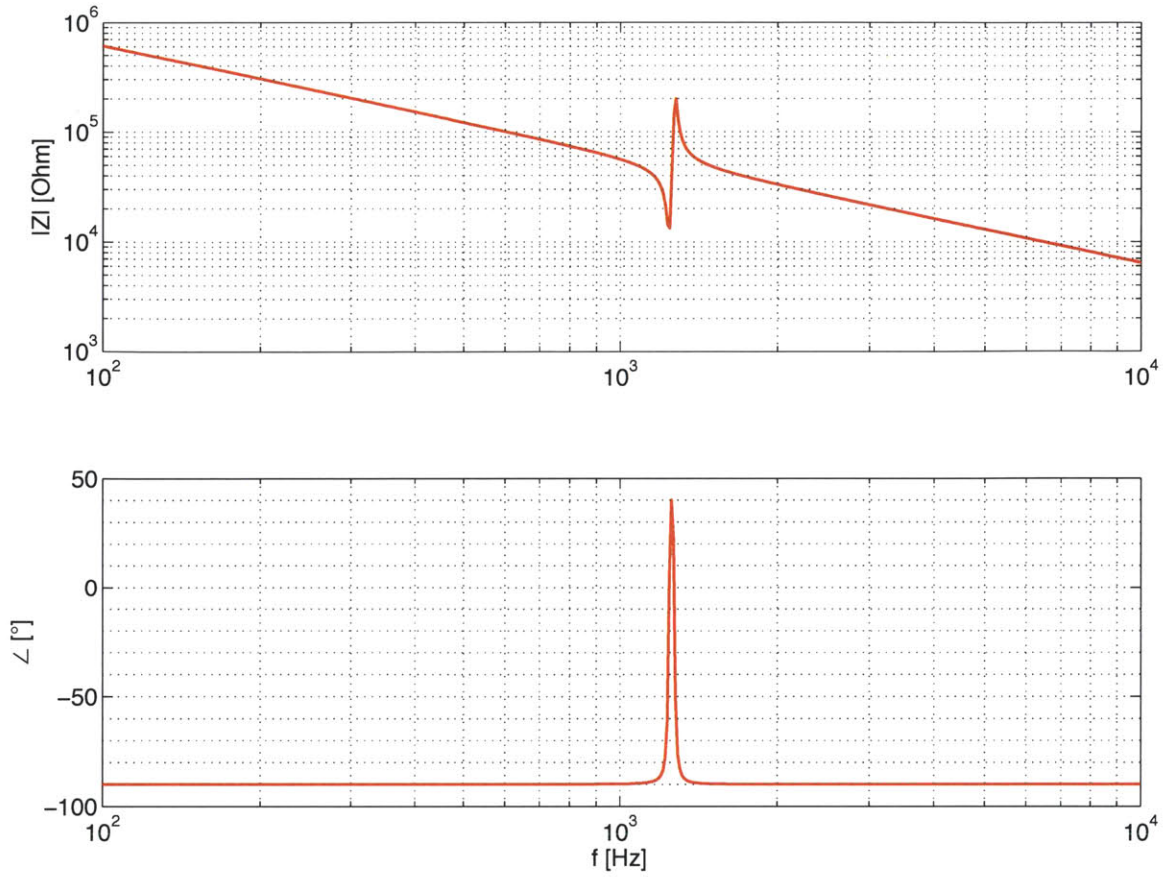


Figure 2-5: Simulated frequency response of the BVD impedance model displaying first resonance.

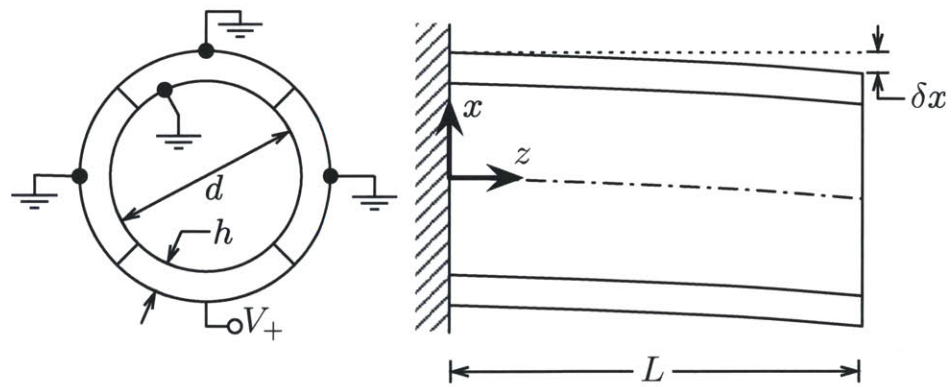


Figure 2-6: Deflection of a piezoelectric tube scanner subjected to an excitation potential applied to one of its four outer electrodes.

First-order design calculations often invoke a model proposed by [16]. For the case shown in Figure 2-6, where a voltage v is applied to only one external electrode, the resulting deflection δx of the free end may be estimated as

$$\delta x = \frac{\sqrt{2}d_{31}L^2v}{\pi dh}, \quad (2.23)$$

where d_{31} is the relevant piezoelectric coupling coefficient (an intrinsic material property specified by the manufacturer). It is worth noting that (2.23) applies to the unloaded quasi-static case and would underestimate the tip deflection for cases where the tube is excited dynamically.

Numerical Deflection Model

A parametric model of the piezoceramic leg and ruby foot assembly was created (COMSOL Multiphysics®) to facilitate exploration of the leg dynamics in response to various excitation waveforms and load conditions, and to obtain estimates of expected step size.

Simulation results depicting the first six resonant mode shapes are shown in Figure 2-7. Note that the first and second modes correspond to the sought after transverse deflections. The third mode of vibration is longitudinal, and deformations are aligned with center axis of the leg. The subsequent three modes all correspond to transverse deflections, however the presence of a node at the center of the foot results in net displacements that are significantly attenuated in comparison to the first two modes. With these simulated characteristics in mind, it was decided to initially focus on utilizing excitation frequencies in the vicinity of the first two modes to induce stepping.

A plot of the simulated frequency response for transverse displacements of the sphere's center is included in Figure 2-8. Modulating the excitation frequency between the second and third modes would appear to result in a variable step size with a dynamic range of almost four orders of magnitude over a frequency span of only about two decades.

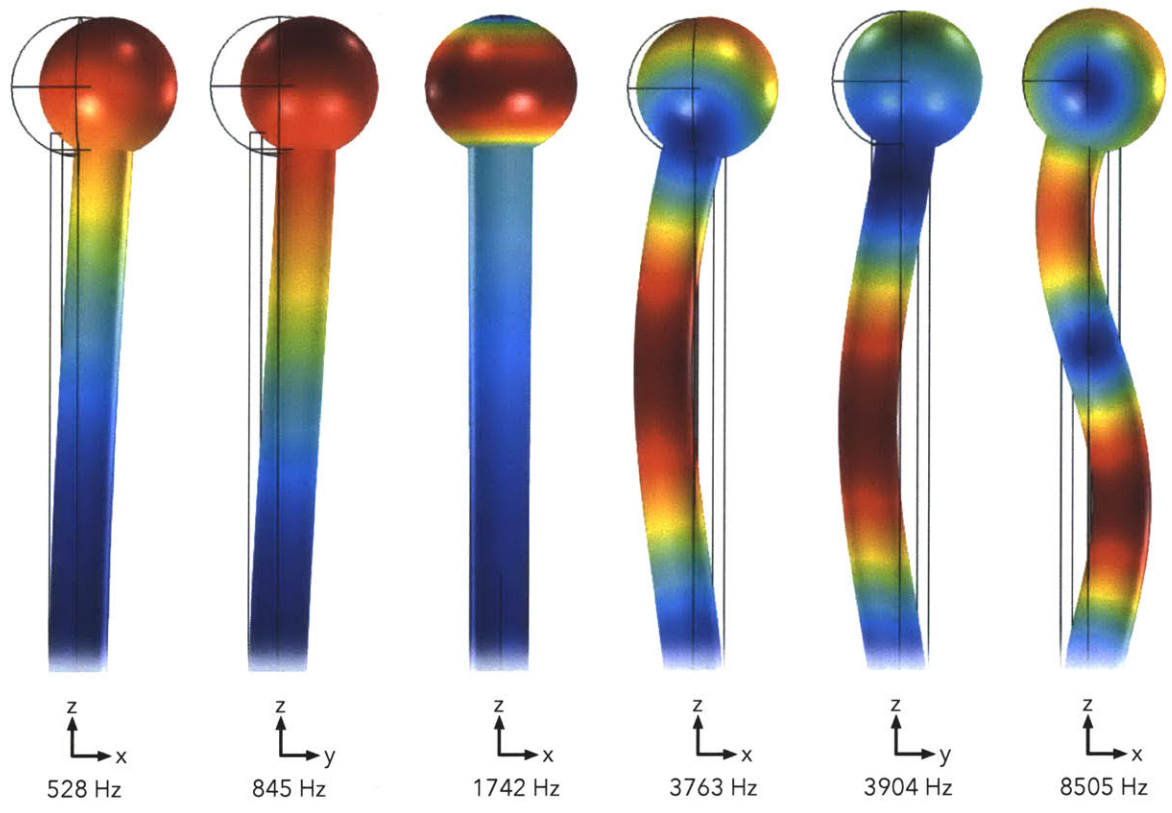


Figure 2-7: Simulation results depicting the first six resonant modes of a scanning tube (PZT-5H) terminated with a spherical element (aluminum oxide).

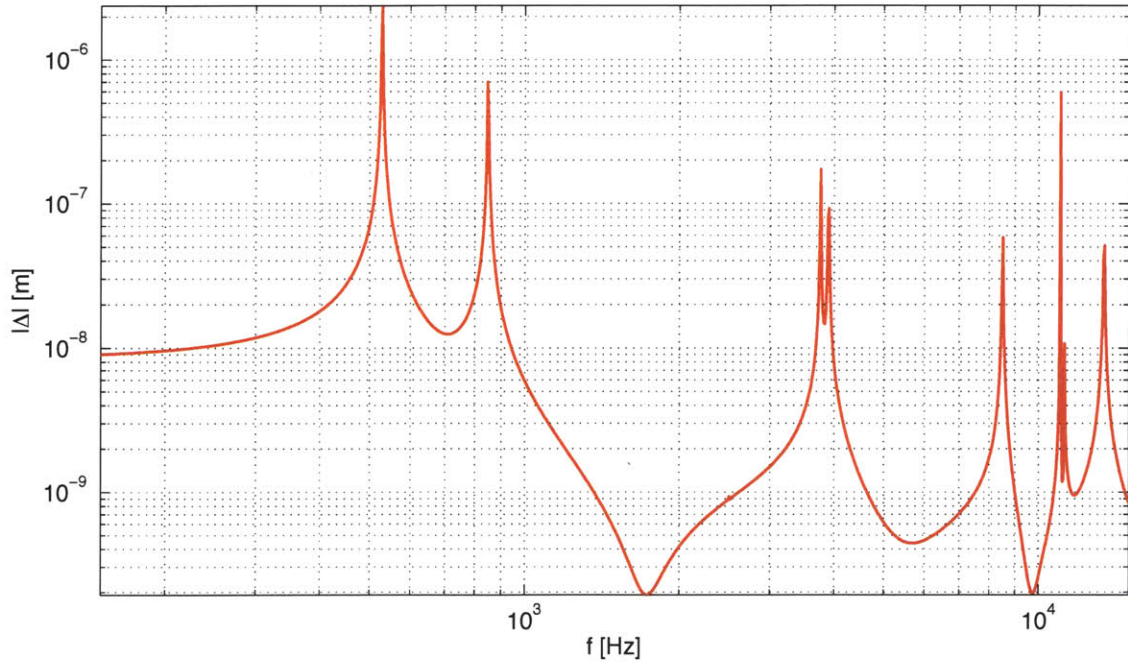


Figure 2-8: Frequency response of the unloaded leg assembly as predicted by numerical model.

2.2 Subsystems

Design elements were organized into four subsystems based on function. A hierarchical map of the ANT subsystem architecture, indicating key components within each subsystem, is provided in Figure 2-9.

2.2.1 Core Subsystem

Components that were considered to be critical for the most basic of device functions were designated to the core subsystem design. These components include the onboard energy storage and the main processing unit, along with regulating electronics to power it.

A rechargeable battery comprised of one or more lithium polymer cells was selected as the power source. High energy density, low cost, and overall convenience (for the end-user and developer

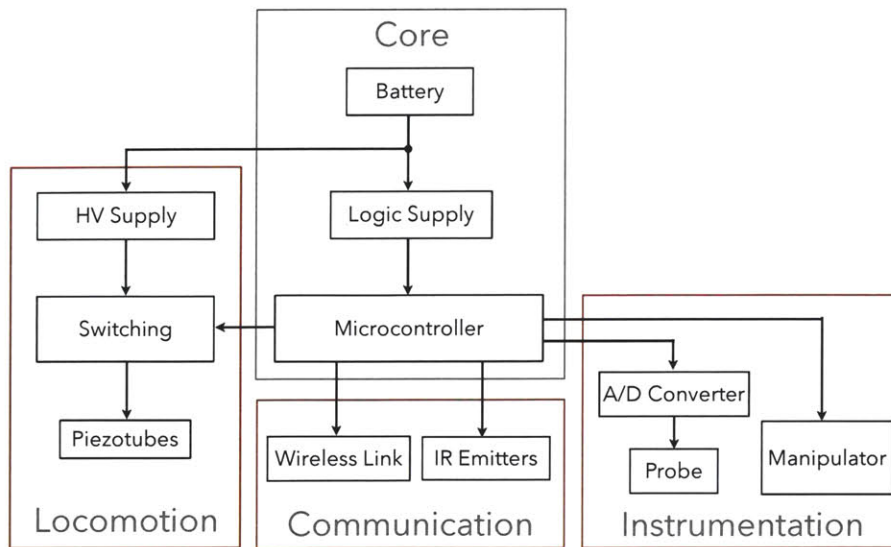


Figure 2-9: Map of ANT subsystems.

alike) were the main deciding factors in selecting this solution over alternatives such as alkaline, nickel-cadmium (NiCd), nickel metal hydride (NiMH), and silver oxide chemistries.

A microcontroller would control and coordinate the other subsystems and perform a number of data processing tasks. As the onboard energy storage would become depleted during use, the core subsystem would have the authority to shutdown non-critical components, such as those comprising the locomotion and instrumentation subsystems, in order to reduce power consumption. The user would then be alerted of the low energy state and given the option to either charge the ANT or initiate a graceful shut down sequence. Colour LEDs on each ANT would serve as visual indicators of the device status, should it be necessary to power-down the primary communication link as well.

A logic supply would be used to convert the unregulated battery output, which, depending on charge may be above or below the microcontroller's rated supply voltage range, into a steady supply rail for the digital electronics. Buck-boost converters are a class of switching power supplies that are capable of efficiently generating a regulated output voltage given an input voltage that may be greater than or less the specified nominal output value.

2.2.2 Locomotion Subsystem

The locomotion subsystem was divided into three distinct design elements: a high-voltage source, an array of high-voltage switching circuits, and the leg assemblies, which comprised of piezoelectric scanning tubes spherical feet.

High-Voltage Source

A compact boost converter circuit was designed in order to generate a regulated high-voltage rail given the low-voltage, time-varying voltage supplied by the onboard lithium polymer cells. Several boosting DC/DC converter topologies were considered, including conventional boost, flyback, and switched capacitor designs. Ultimately, a tapped-inductor boost converter² design was selected, as it provided high voltage gain over a single converter stage using a minimal number of components [28, 47].

Modern boost converter controller ICs containing internal transistors that are capable of switching potentials in excess of 40 V are not uncommon. An external transistor with a higher voltage rating may be added should one need to generate an output that exceeds the maximum voltage rating specified for the internal switch, however this approach may be undesirable, as more parts will be required and increased switching losses may result.

Flyback converters replace the single inductor found in conventional boost converters with a transformer, providing galvanic isolation between the output terminals and the rest of the switching electronics. By increasing the ratio of the number of turns in the secondary winding with respect to the number of turns in the primary winding beyond unity, output voltages may safely exceed the maximum voltage rating of the switching transistor. However, additional circuitry is required to regulate the secondary coil's output on account of the aforementioned galvanic isolation. Furthermore, the load must accommodate a floating ground, which may require additional isolation electronics.

²Also known as coupled-inductor or autotransformer boost converter

Tapped-inductor boost converters combine the compactness and simplicity of conventional boost converter topology, whilst being capable of safely generating output voltages in excess of the switch maximum rating, much like flyback converters do; a schematic representation is provided in Figure 2-10. The single inductor of the conventional topology is replaced by a pair of inductors connected in series and wound around a common core. The point at which the two inductors are connected is connected to the switching transistor's drain or collector. The controller's feedback terminal is connected to converter's output by way of a voltage divider, thus providing regulation of the actual output voltage.

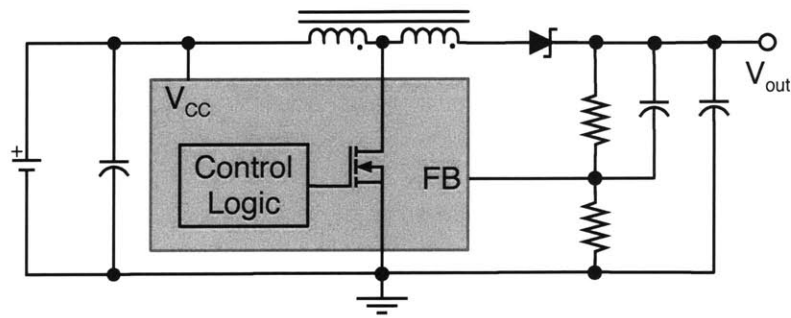


Figure 2-10: Tapped-inductor boost converter.

It was also necessary to consider the environment in which the converter would be operating. For example, high voltage switching devices that may be used inside of a functioning SEM should be designed with sufficient shielding so as to prevent EMI and distortion. Utilizing lower voltages (*e.g.*, $\lesssim 50$ V), as was done in this work, lessens the amount of interference. Insulating otherwise exposed conductors may also be desirable; reducing the likelihood of an unintended short circuit when operating amidst conductive surfaces.

High-Voltage Drive Electronics

Intermediate drive electronics were required to translate the logic-level signals output by the microcontroller to the substantially higher voltage that was used to excite the piezoelectric legs. Given that each leg had four input electrodes, a total of 12 separate excitation signals were to be amplified.

In prior work, sophisticated amplitude modulation techniques were implemented[34] and designers opted to use digital-to-analog converters (DAC) and high-voltage linear amplifiers. Such designs may be suitable for instruments with access to significant energy reserves, as is the case with line powered benchtop machines, but are less than ideal for self-powered mobile devices. Semiconductor-based linear amplifiers generally introduce very little distortion over their design bandwidths, but do so at the expense of efficiency. In situations that may accommodate the introduction of some non-linear frequency characteristics, a class-D amplifier may be a more appropriate solution. Class-D amplifiers, also known as switching amplifiers, typically use a high frequency pulse width modulation (PWM) encoded analog signal to drive a transistor bridge, or half-bridge. The output of the bridge passes through a low-pass LC filter, resulting in an amplified approximation of the original analog input signal. The transistors that perform the amplification are usually in either of their lowest power states - fully on or off - leading to significantly higher efficiency than linear amplifier designs.

Since the proposed frequency modulation scheme only required a binary excitation signal, obviating the need for DACs or PWM encoding, and the amplification stage could be efficiently implemented using a simple voltage translator design, like the one shown in Figure 2-11. Aside from reducing the power consumption in the amplification stage, transistor pairs, like the ones depicted in Figure 2-11a were readily available as monolithic devices (Figure 2-11b), furthering their suitability for space constrained and cost-conscious applications.

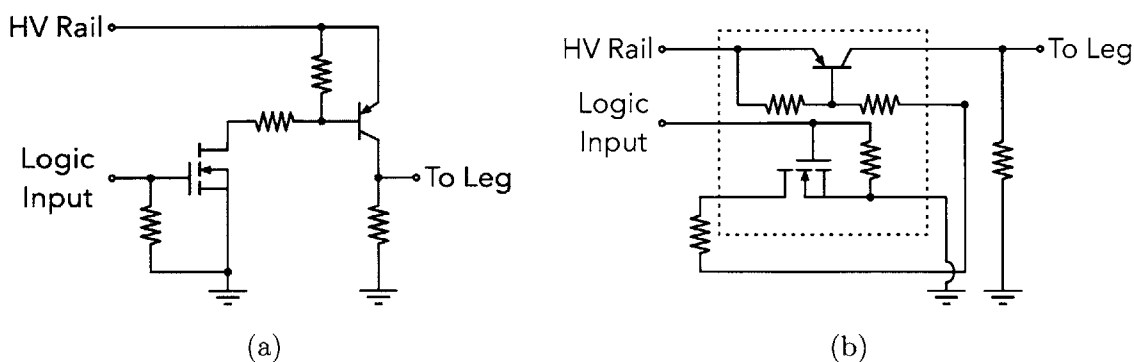


Figure 2-11: (a) A cascaded transistor high voltage switching circuit. (b) The same circuit realized using a monolithic load switch IC.

2.2.3 Communication Subsystem

The communication subsystem was to provide a bidirectional communication link between the ANTs and the control interface, allowing users to transmit control inputs, receive acquired measurements, and monitor the device status.

Interface Type

To date, many mobile microrobotic devices had used tethers for communication and power transmission. Tethered interfaces are robust and can support high data rates, however the wires and/or fibers that comprise a tether exert forces and torques on the devices to which they are connected. This form of loading is undesirable and is detrimental to positioning accuracy. Lightweight microrobotic devices may not be capable of compensating for such disturbances. Additionally, tethers can obstruct motion (*i.e.*, mechanical congestion), especially in situations where multiple microrobots are operating within a common workspace.

In lieu of a tethered communication interface, some systems have adopted an optical link [26, 36]. To improve SNR when operating in environments with ambient lighting, infrared emitters (IR) are often used as the transmitting elements. Photodetectors, often with peak quantum efficiency in the vicinity of the transmission wavelength, are used as receivers. IR communication consumes relatively little power ($< 1 \mu\text{A}$ in standby). However, data rates tend to be low (1.5 – 4 Mbps), line-of-sight conditions are often required for reliability, and fairly sophisticated techniques (*e.g.*, error detection and frequency modulation) must be employed in order to support multiple channels or full-duplex communication.

In recent years, advances in RF transceiver design and fabrication technologies have made integrated radio circuits a viable option for applications requiring low power, high-bandwidth communication³. Some transceivers are protocol specific, with circuit designs that are optimized for an industry standard communication protocol, such as ZigBee[®], Bluetooth[®], and Wi-Fi[™], while others support user-defined proprietary protocols and support data rates in excess of 2 Mbps. Adopting

³A comprehensive comparison of various wireless communication solutions is provided in [45].

an existing protocol offers both convenience and compatibility, but include compromises, like trading performance for robustness, or low-latency for energy savings. The ANT firmware was to be developed from the ground up rather than building upon an existing operating system, providing an opportunity to tightly integrate wireless communication functionality with the rest of the software architecture to enable efficient, low-latency, wireless communication.

2.2.4 Instrumentation Subsystem

The form and function of the instrumentation subsystem were intended to be dependent on the application for which an ANT will be used. For example, a user may functionalize an ANT to perform atomic force microscopy, in which case a hardware module consisting of a scanning tube, cantilever, and excitation/sensing electronics would be installed as the instrumentation subsystem. Alternatively, a user may instead choose to install a micro-gripper as their instrument of choice for performing micro/nano-manipulation and fabrication tasks.

For demonstration purposes, the development of a compact AFM was strongly considered, and several hardware components were prototyped. One of the interesting challenges involved the design of a compact actuator for raising delicate probe assembly when traversing between measurement sites. Inch-worm type actuators had been used previously [35], but are complex and require precision components, which increase cost. An alternate approach, wherein a Lorentz force linear motor would serve as a direct drive actuator, was briefly explored (see Appendix B). While mechanically simpler, this form of motor would require a continuous current draw in order to actively hold a position – undesirable for a device with limited onboard energy reserve.

Ultimately, development of the AFM was placed on hold as long working distance SPM concept presented itself; a novel scanning capacitive probe microscope was developed and integrated into one of the ANT hardware prototypes. Capacitive probe microscopes sense changes in capacitance, which may result from changes in a sample's dielectric properties or surface topology.

Chapter 3

Prototype Development

Numerous ANT prototypes were developed, sporting various incremental changes and refinements to the electrical and mechanical design elements.

3.1 Mark I

The Mark I prototype, shown in Figure 3-1, was designed to determine the feasibility of realizing several key functional requirements by demonstrating high-duty cycle locomotion over a reasonable period of time using energy stored onboard. A “reasonable period of time” being anywhere from 15 minutes to an hour; long enough for a user to acquire sequence of samples or capture a few images.

The microcontroller (NXP Semiconductor[®] LPC1313) containing a high-performance ARM[®] Cortex-M3[™] microprocessor (70 MHz, 8 kB memory, 32 kB flash) was selected since it satisfied the design’s peripheral (*i.e.*, GPIO, SPI, I²C, ADC, timers) and I/O requirements (12-pin ports allowing changes to all leg electrodes to be synchronous), and was the lowest-power device of its class (200 $\mu\text{A MHz}^{-1}$) at the time that development began. Additionally, the microcontroller packaging was suitably small (48-pin, 7 mm \times 7 mm QFP), and low-cost.

The high-voltage power supply was based on a LCD bias supply controller with a 30 V internal switch

(Maxim Integrated Products[®] MAX1605). The controller operated in a fixed-frequency mode with a switching frequency of 500 kHz, which allowed for small surface-mount ancillary components to be used. A miniature (4 mm × 4 mm × 1.1 mm) shielded coupled inductor (Coilcraft[®] LPR4012-202B) was selected as the tapped-inductor, as it provided a sufficiently high saturation current rating ($I_{sat}=1.7\text{ A}$), an appropriate turn ratio ($N_p : N_s = 1 : 2$) and primary inductance ($L_1=2.0\text{ }\mu\text{H}$ nominal), and a suitably low DC resistance ($R_{L_1}=0.24\text{ }\Omega$, $R_{L_2}=0.48\text{ }\Omega$). A Schottky diode was used as the freewheeling diode (NXP Semiconductor[®] PMEG4010ER), in order to minimize the voltage drop when forward biased. The controller feedback network was configured to provide a nominal stable output of 20 V as a conservative starting point.

A pair of 8-channel CMOS logic to high-voltage level translators (Analog Devices[®] ADG3123) applied the high voltage excitation potential to the 12 leg electrodes as per the microcontroller logic-level command signals. The translators provided a convenient solution for managing the high voltage switching task in a single stage, whilst requiring no additional components.

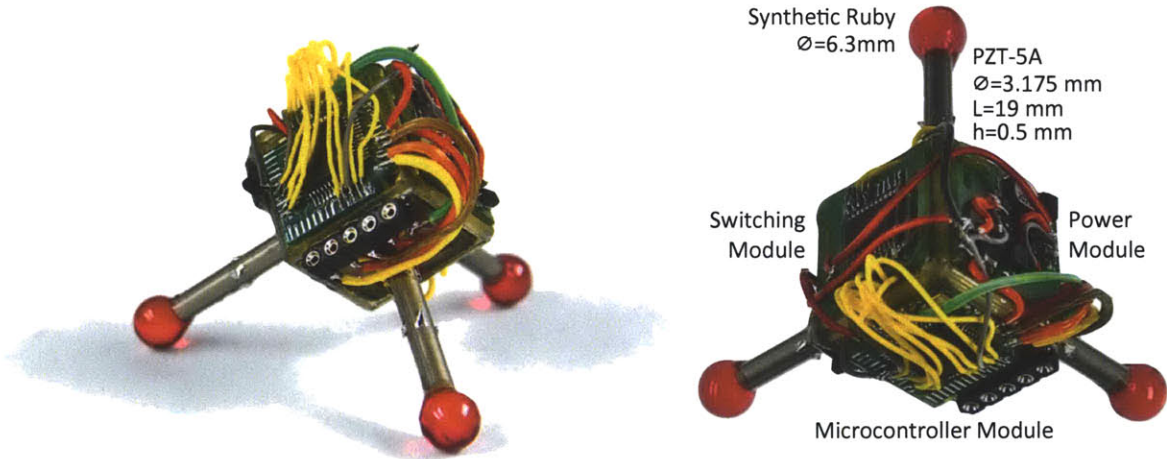


Figure 3-1: Assembled Mark I prototype.

Additionally, the Mark I provided a starting point for developing the fabrication and assembly techniques. The various subsystems were distributed among a number of tabulated 14 mm × 14 mm × 1.6 mm rigid PCB modules. Once populated, the modules were separated and mounted in a lightweight polymer frame (3D Systems[®] Accura[®] 40) that was fabricated via stereolithography

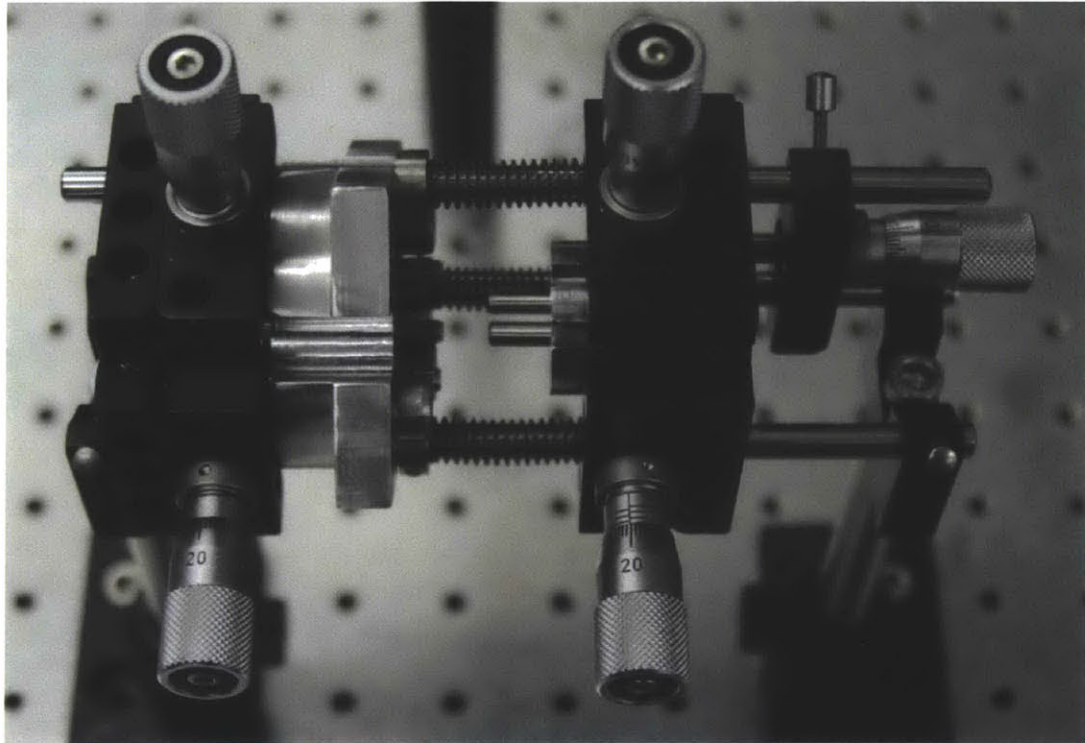
(3D Systems[®] Viper SLA), and secured in place with a high-stiffness UV-cure adhesive (Loctite[®] 349). The various PCB interconnects were completed by manually soldering individual jumper wires. Prior to sealing, a 20 mA h rechargeable lithium polymer cell was installed inside of the body cavity.

A jig was constructed from machined fixtures and optical mechanical components (QiOptiq[®] LINOS Microbench) to assist in aligning and securing the piezoceramic legs (Boston Piezo-Optics Inc.) their corresponding cube faces in a manner that would present some degree of leg orthogonality. The jig, seen in Figure 3-2, consisted of two parts (i) a kinematic mount for holding a square piece of FR-4 to which the leg would be mounted, and (ii) a semi-kinematic mount for holding a piezoceramic leg tube. Micrometers were used to align the leg along three axes. Once in place, tubes were bonded to the FR-4 panels with a circumferential fillet of UV-cure adhesive. Adhesive was also used to bond the spherical ruby feet in place at the end of the tubes. A terminal strip mounted along one edge of the body provided connections for programming/debugging and charging hardware.

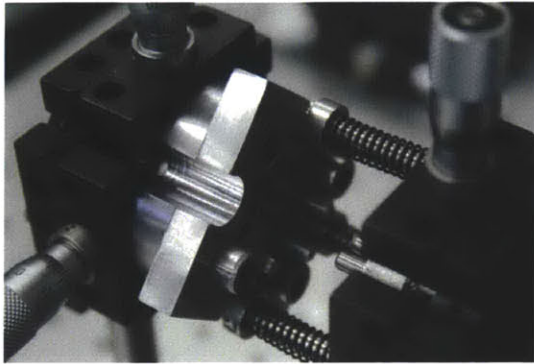
The Mark I proved to be a success, demonstrating rates of 3 mm s^{-1} in translation and 6° s^{-1} in rotation when excited at 3 kHz. From a fully charged state, the device was able to step non-stop for 30 minutes.

3.2 Mark II

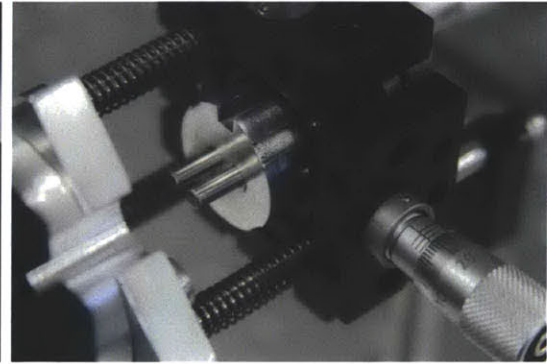
The Mark II prototype integrated the various subsystem designs that comprised the Mark I onto a single two-layer flexible printed circuit board (Tech-Etch Inc.), shown in Figure 3-3. Once populated, the flex PCB was folded around a lightweight polymer frame and bonded in place with UV-cure adhesive resulting in a hollow cube-shaped chassis onto which the three legs could be mounted. Each cube face was reinforced with a 0.8 mm thick FR-4 stiffener bonded to the flex PCB. Two 20 mA h LiPo cells were installed inside of the body cavity, doubling onboard energy storage capacity of the Mark I prototype.



(a)



(b) Kinematic PCB mount.



(c) Semi-kinematic tube mount.

Figure 3-2: Leg mounting jig.

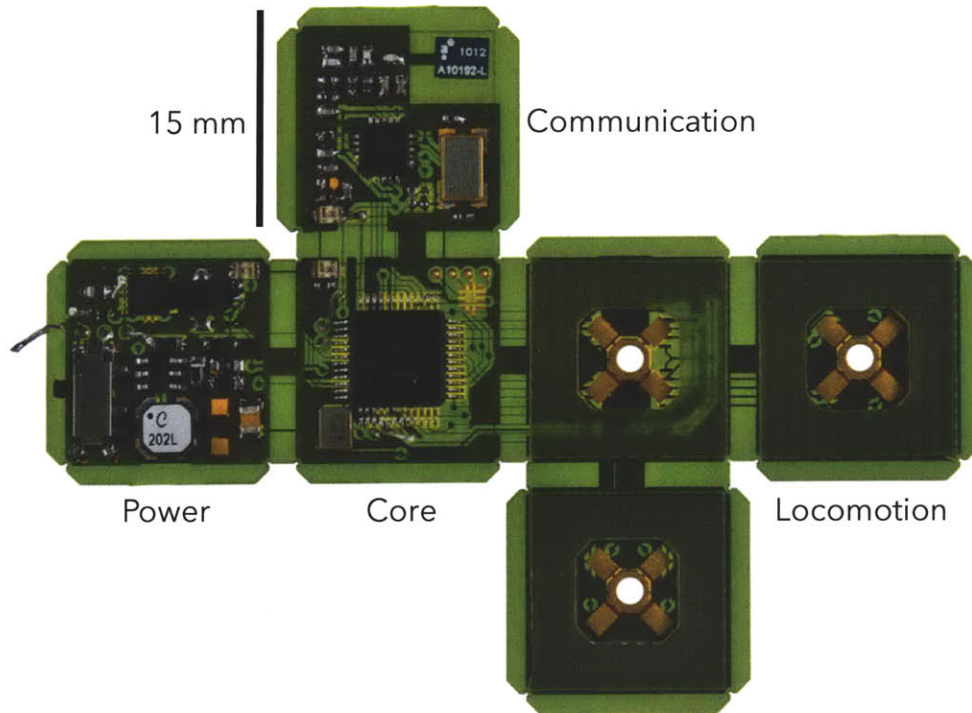


Figure 3-3: Mark 2 flex PCB prior to final assembly.

The radically different construction of the Mark II was found to be incompatible with Mark I leg mounting jig. Each piezoceramic leg was carefully mounted its respective section of the flex PCB prior to folding. Unlike the Mark I, solder joints between the leg electrodes and their corresponding electrical contacts on the PCB served as both direct electrical connections and mechanical joints. Once again, the spherical ruby feet were secured to the legs with adhesive. The assembled Mark II prototype is shown in Figure 3-4.

The integrated electrical layout required less board space, readily accommodating the addition of the communication subsystem hardware. A low-power 2.4 GHz transceiver (Texas Instruments® CC2500) was selected as the radio IC and paired with a small chip antenna (Antenova® Fusca).

Despite a number of the design refinements, the Mark II presented a reduction in stepping performance, with a peak translational rate less than 1 mm. The decrease in performance was likely attributed to an increase in compliance at the leg-body joints. Manufacturing limitations mandated that the FR-4 stiffeners be mounted on the outer surface of the cube. Cut-outs were made in the

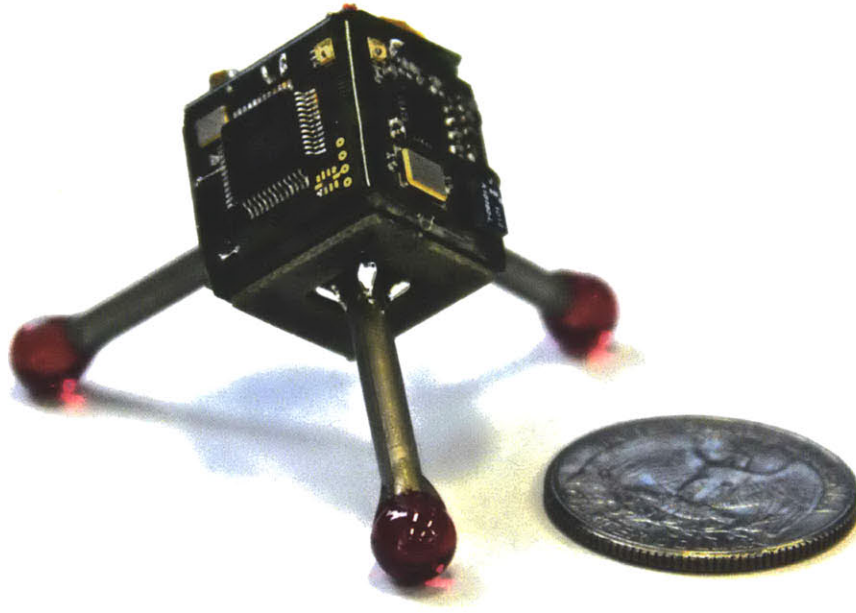


Figure 3-4: Mark II prototype.

stiffeners to accommodate the electrical connections between the tube electrodes the corresponding solder pads on the flex PCB. The resulting loss of support was apparently substantial enough to adversely impact the leg-body mechanical coupling.

3.3 Mark III

Like the Mark II, the Mark III prototype was fabricated using a rigid-flex PCB construction. In order to reduce development costs and facilitate the process of implementing revisions to the electronics design, a rigid module on flexible PCB construction was devised. A 25-unit panel of generic flexible PCB backplanes, as shown in Figure 3-5a, was produced (Flex Interconnect Technologies). A less expensive rigid PCB that was geometrically representative of the final configuration, seen in Figure 3-5b, was designed, populated, and tested. Once the functionality of each subsystem was confirmed, a 0.75 mm thick diamond cutting wheel was used to separate the individual modules that would eventually serve as the cube faces. The six rigid PCB modules were then reflow soldered

onto the flexible backplane, resulting in the rigid-flex assembly shown in Figure 3-5c.

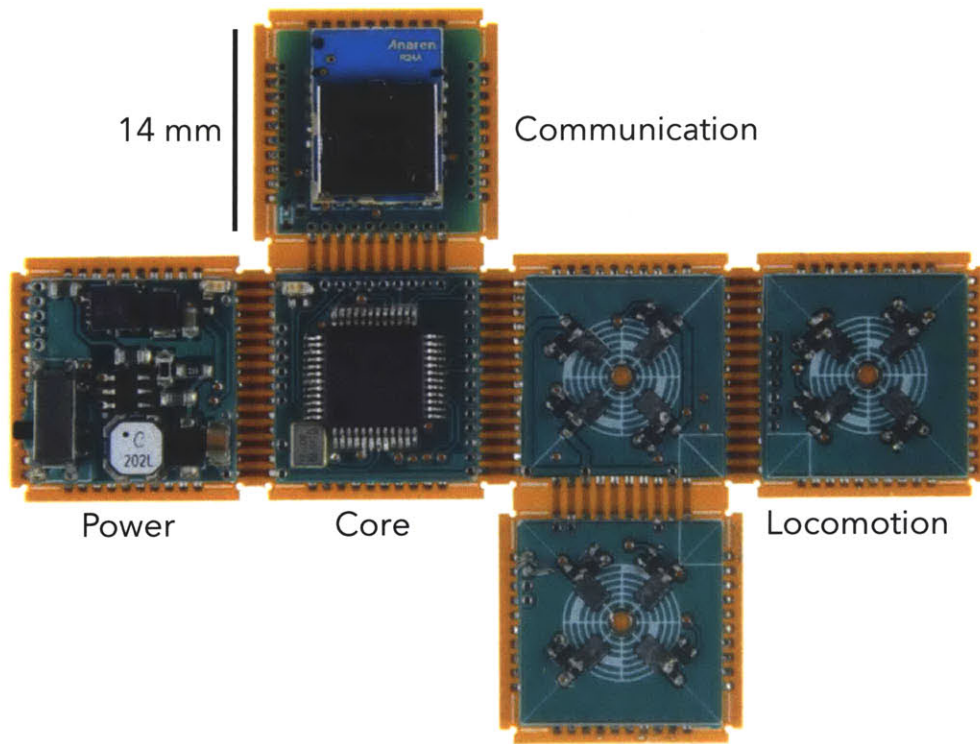
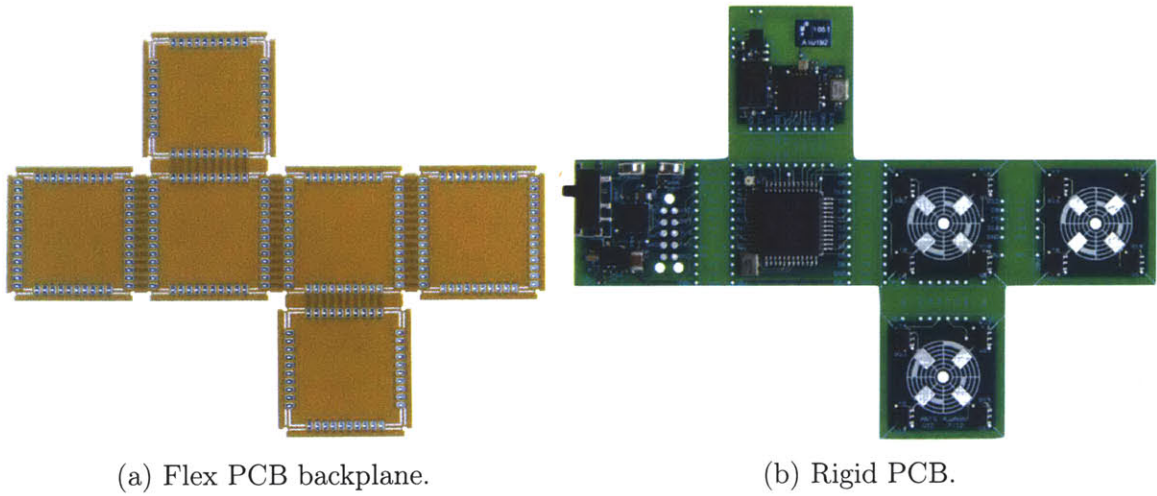


Figure 3-5: Mark III rigid-flex PCB assembly.

For this prototype, a surface mount integrated radio module (Anaren[®] A2500R24A), was used in an attempt to improve the reliability of the wireless communication link. The module was based

on the same radio transceiver used in the previous designs, but provided greater EMI shielding and utilized RF-grade material for the PCB substrate.

The power electronics were also revised in order to increase the maximum step size. The high-voltage boost converter feedback divider was set to produce a regulated output of 50 V, more than twice that of the predecessors. Increasing the high-voltage rail potential required a redesign of the downstream high-voltage switching electronics. The new design simply used discrete MOSFETs (Diodes Incorporated[®] DMN55D0UT) configured as inverters to amplify the logic-level switching signals. This switching design required less board space, but resulted in significant power dissipation and slow rise times at the leg electrodes. Most of the design revisions were considered to be successful improvements, though the over-simplistic switching electronics were not. Fortunately, revisions to the switching circuit design were soon devised and employed in subsequent prototypes.

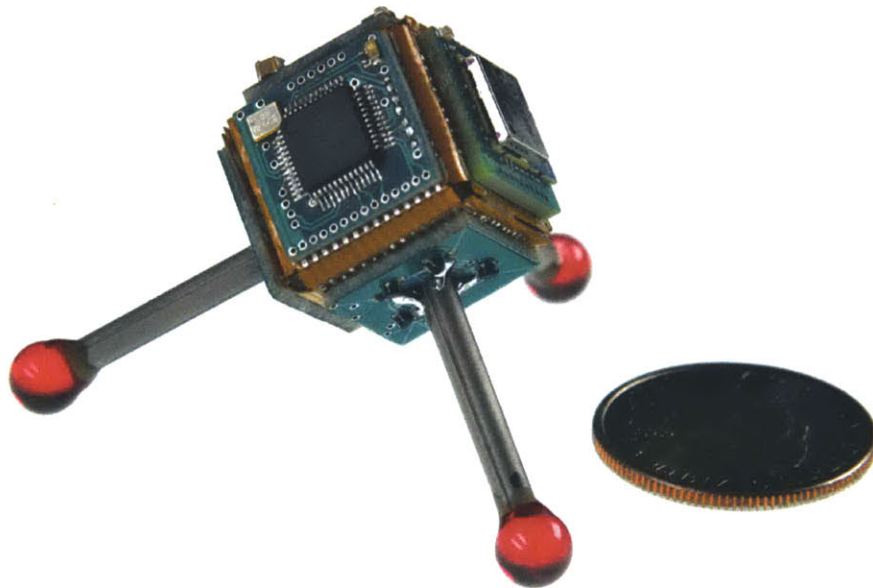


Figure 3-6: Mark III prototype.

3.4 Mark IV

The Mark IV utilized the same rigid-flex construction as its predecessor, but benefited from a significant number of design revisions and added features.

The radio transceiver was upgraded to a different model that featured lower power consumption and increased bandwidth (Nordic Semiconductor[®] NRF24L01+). The passive RF components and layout were revised to improve signal integrity and accommodate additional electronics on the same PCB module.

A 9-axis IMU (Invensense[®] MPU-9150) was added to allow for measurement of linear accelerations, angular rates, and orientation in three-dimensions.

Following success with several bench-level test designs, a capacitance-to-digital converter was added (acam[®] PCAP01) to demonstrate how onboard instrumentation may be integrated with the rest of the ANT architecture. A compact, low-power, 3.0 V LDO linear regulator (Texas Instruments[®] TPS72730) was added to mitigate the presence of switching noise and transients on the instrumentation supply rail.

The majority of design improvements involved the locomotion subsystem electronics. The high-voltage boost converter controller was upgraded to a more efficient component (Texas Instruments[®] TPS61170) that operated at more than twice the switching frequency (1.2 MHz) of the part that it replaced, thus allowing for a reduction in the size of passive components, and providing a greater frequency margin between the switching supply and instrumentation operating bandwidth.

Several alternative designs were evaluated as candidates for the high-voltage switching circuits. Ultimately, a solution based on integrated load switches resulted, providing low power consumption, a small footprint, and large bandwidth (25 MHz). The new design utilized a pre-biased PNP transistor and N-channel MOSFET pair integrated in a common package (Diodes Incorporated[®] LMN200B02).

A connectorless interface was added to facilitate charging, in-circuit programming/debugging, and for testing wired serial communication. A special 10 contact pogo-pin cable (Tag-Connect[®] TC2050-

IDC-NL) provided the connection between the ANT and the charger/programmer/debugger hardware.

Load switches (Fairchild Semiconductor[®] FPF1003A) were added to disconnect sub-circuits when not in use. One load switch was included upstream of the battery voltage monitor circuit, preventing the battery from needlessly discharging through the voltage divider resistors when not being monitored. A second load switch was added upstream of the high-voltage boost converter input rail in order to prevent parasitic losses through the tapped-inductor and output filter when the ANT is not stepping.

The three discrete status LEDs present on previous designs were replaced with a single RGB LED (Lumex[®] SML-LX0404SIUPGUSB), in order to reduce part count and reduce board space usage. The red, green, and blue channels were each used to inform the user of the occurrence of an error, the power state, and of ongoing radio activity, respectively.

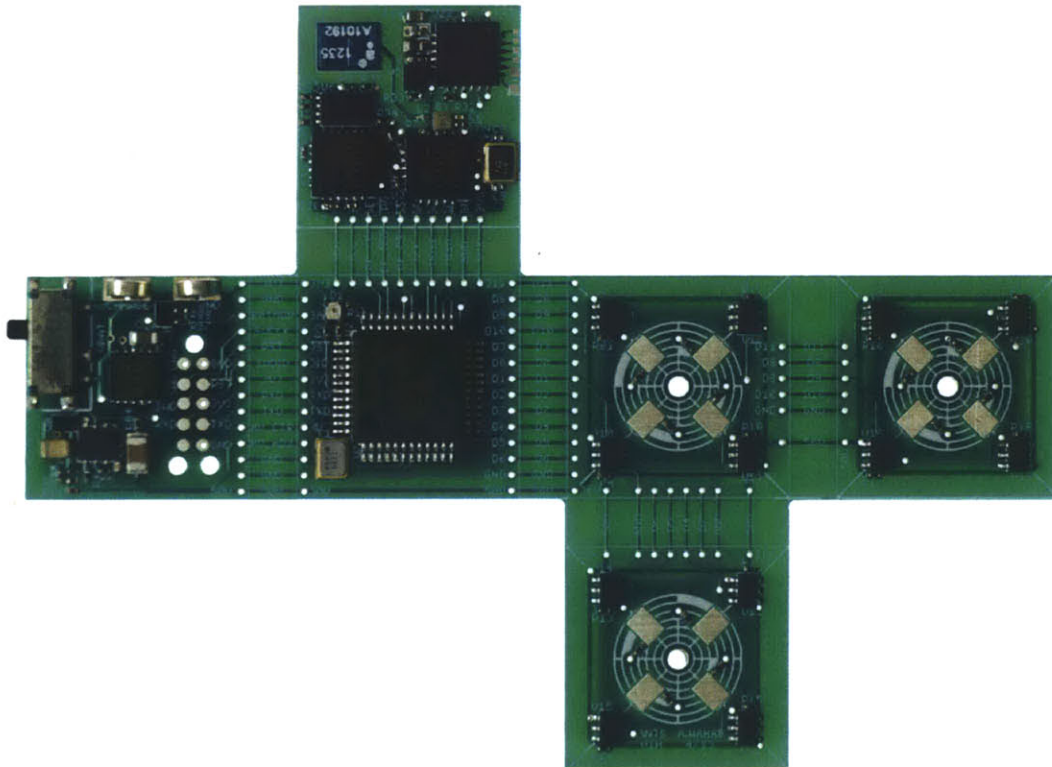


Figure 3-7: Mark IV rigid PCB assembly prior to final assembly stage.

To improve consistency and accuracy of the leg mounting process, a new jig, shown in Figure 3-8, was created. Rather than aligning each leg with respect to its associated PCB module, the revised technique aligned and fixtured all three legs with respect to a common global reference. The 6 mm thick 6061-T6 aluminum alloy hexagonal plates were machined using a wire EDM (Charmilles® Robofil 1020SI), and aligned with 6 mm diameter precision optical rails.

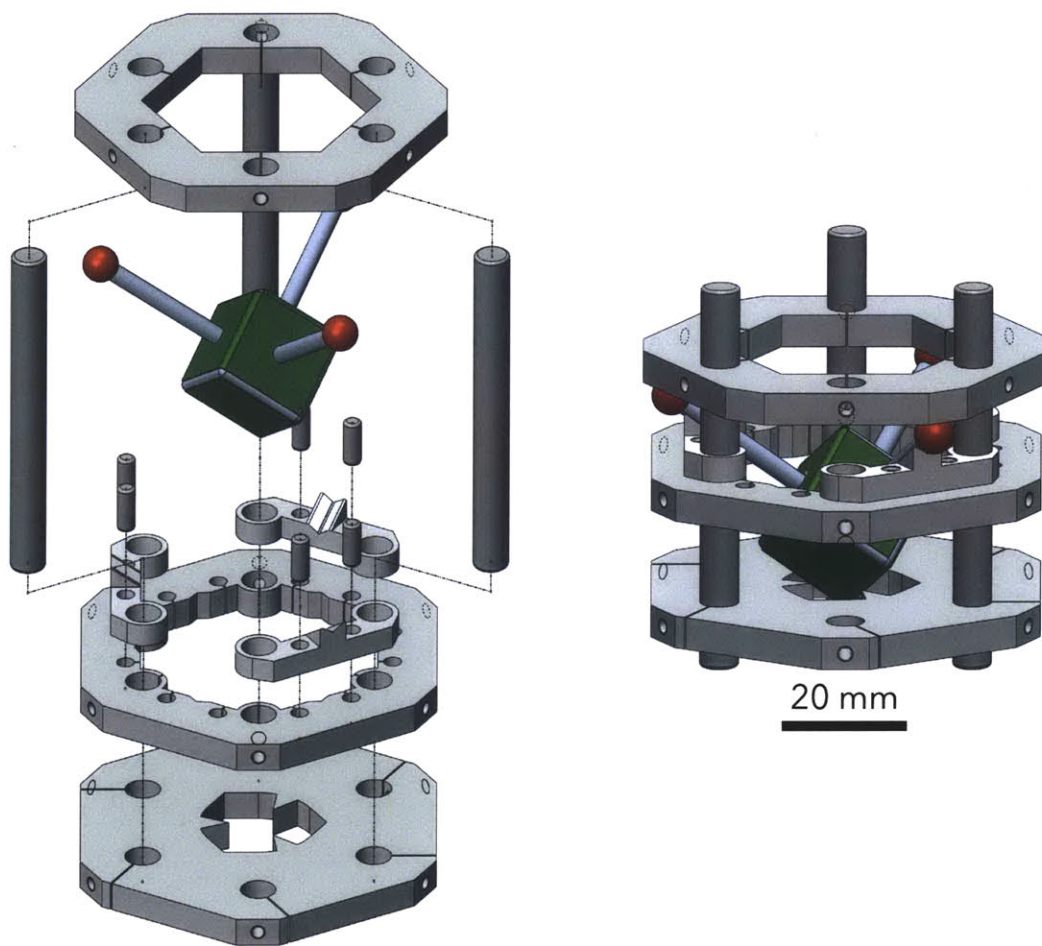


Figure 3-8: Revised leg mounting jig.

After being folded into a cube, the populated rigid-flex PCB assembly was placed onto the jig's bottom plate such that the three faces onto which the legs were to be soldered faced upwards. The three piezoelectric tubes were then seated in corresponding vee blocks, positioned 120° apart, located on the middle jig plate. Size 10 rubber bands were used to hold the fragile ceramic tubes in place, whilst still allowing adjustments to be made. The top plate was then lowered until all

three legs were constrained between the aforementioned plate and the ANT body. Tight tolerances among the plates, optical rails, and vee blocks ensured that, once constrained, the tubes would sit in a manner as to be orthogonal to one another. Set screws on each plate were then tightened, and solder joints were made between each tube's outer electrodes and corresponding PCB pads. Once the legs were soldered in place, the top plate was removed, allowing the leg-body assembly to be extracted. The ground connections between the PCB and each tube's internal electrode was then made using 2 mm to 3 mm long segments of 0.4 mm (No. 26 AWG) nickel-plated copper bus wire. Temporary "tack" bonds, holding the one face of the cube (populated with the power electronics) were removed, allowing access to the internal cavity. The bus wires were positioned and soldered in place from within the cube. Once the battery pack was installed, the access face was folded shut and secured in place with beads of adhesive along each edge. The 0.0126 kg fully assembled Mark IV prototype is shown in Figure 3-9.

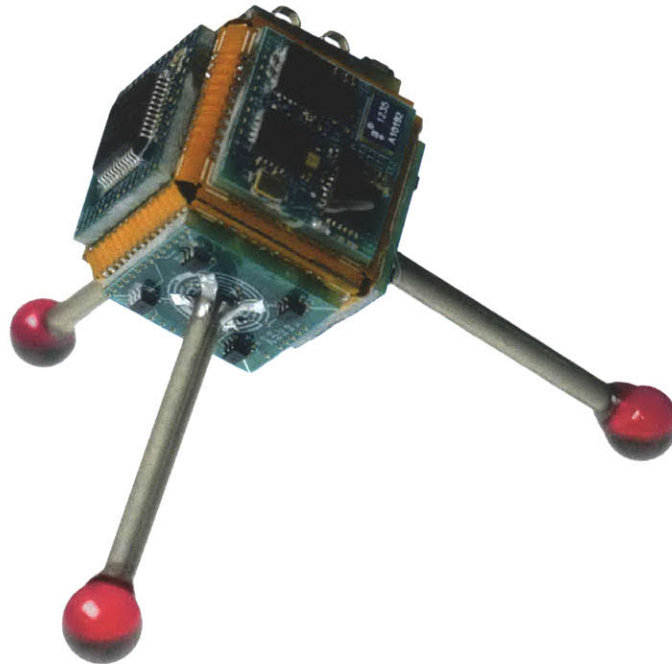


Figure 3-9: Mark IV prototype.

3.5 Mark V

Developing the Mark V hardware involved only minor changes to the electronics and fabrication. The power and ground plane layouts were modified to reduce noise coupling, and the radio antenna transmission line was rounded to reduce reflected interference. The populated Mark V PCB assembly is shown in Figure 3-10.

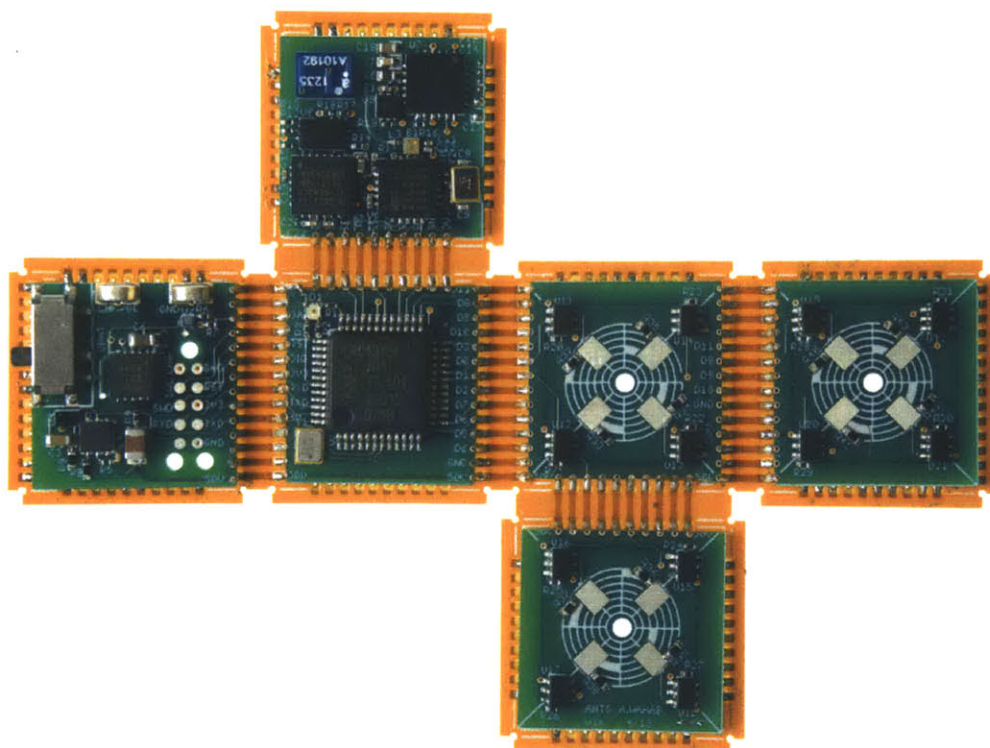


Figure 3-10: Mark V rigid-flex assembly prior to folding.

A more rigid UV-cure adhesive (Loctite[®] 4305) was used to bond and reinforce the folded rigid-flex PCB assembly and to secure the synthetic ruby spheres to the piezoelectric ceramic legs. The useable volume inside of the body was increased by omitting the internal polymer frame, opting instead to apply beads of the rigid adhesive along each edge. As a result, this prototype was able to accommodate a larger internal battery, comprised of four 40 mA h lithium polymer cells connected in parallel, marking a 33% increase in energy storage capacity over its predecessor. The

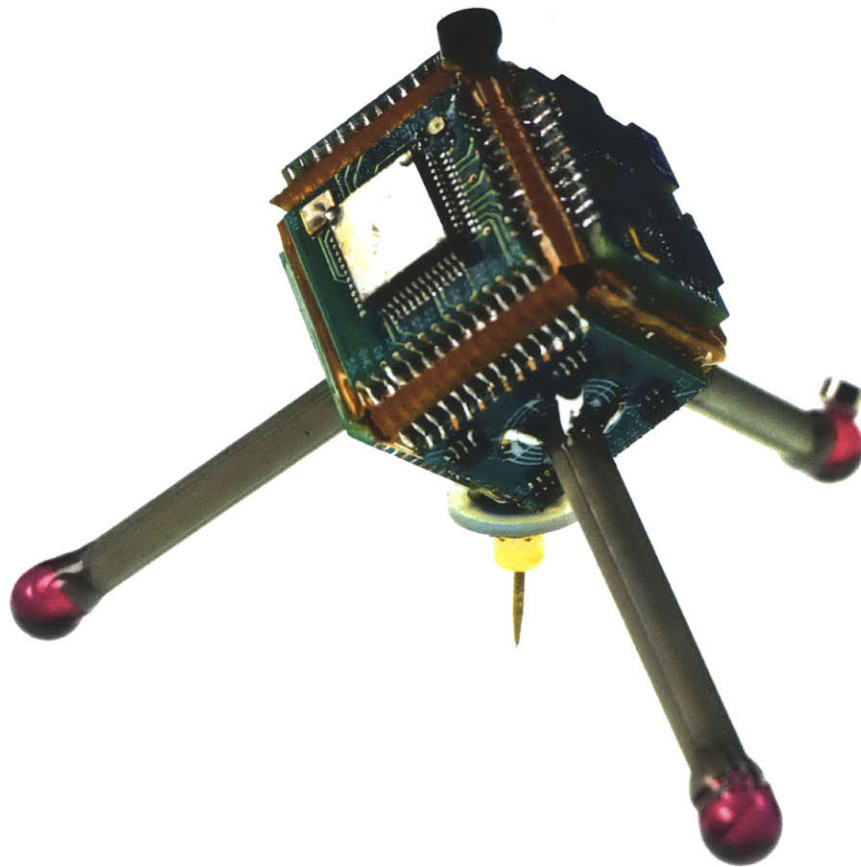


Figure 3-11: Mark V prototype with a capacitive probe is shown mounted on the bottom chassis apex.

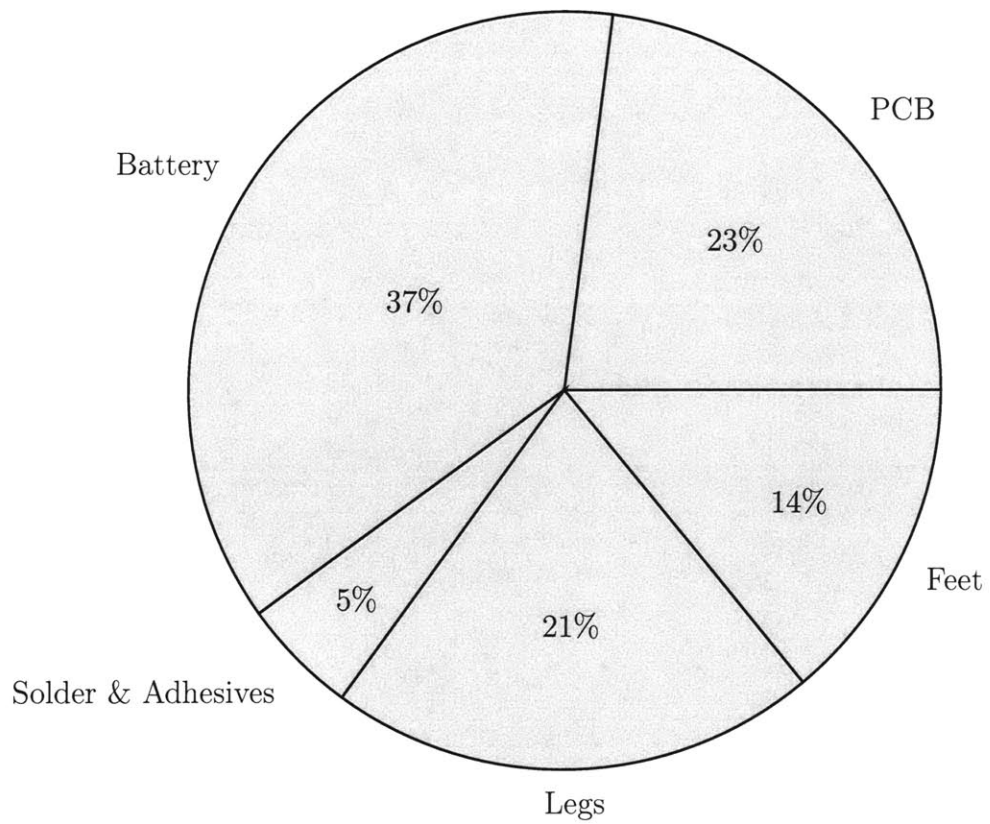


Figure 3-12: Mass distribution for Mark V prototype. Total measured mass was 0.0142 kg.

fully assembled Mark V prototype is included in Figure 3-11.

For reference, a breakdown of the Mark V mass distribution is provided in Figure 3-12. As expected, the internal battery comprises the majority of the body mass, followed by the rigid-flex PCB assembly and the piezoelectric legs. The increase in total mass due to the addition of an additional lithium polymer cell was, in part, offset by reducing the diameter of the synthetic ruby feet from 6 mm to 5 mm, resulting in a 42% reduction in the dynamic loading encountered by each leg.

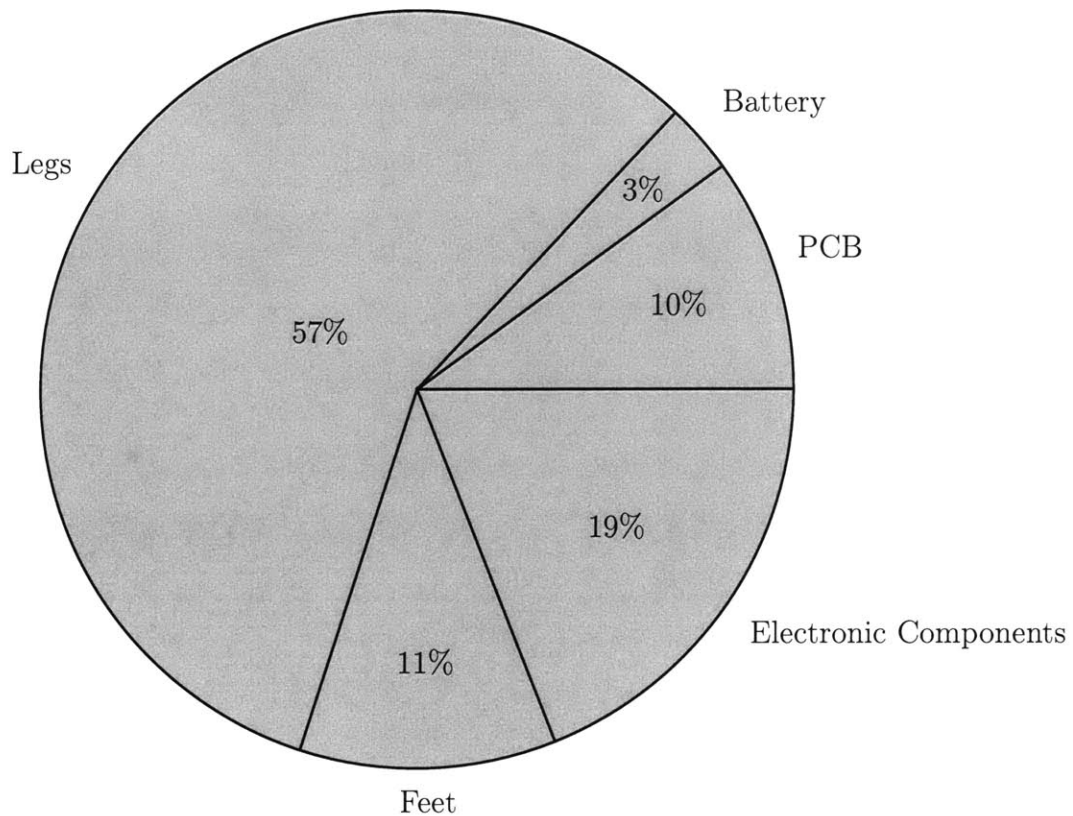


Figure 3-13: Breakdown of component costs for Mark V prototype. Total cost was \$525 (USD).

An approximate breakdown of the component costs for the Mark V prototype is represented in Figure 3-13. It is worth noting that the \$525 (USD) bill of materials cost does not account for any price savings that might arise when produced in larger quantities. Furthermore, the quoted cost does not account for assembly, testing, and software development.

The total component power distribution is illustrated in Figure 3-14. The values are representative of

power consumed during continuous stepping while receiving user input commands and transmitting periodic orientation updates over an active communications link. Under these conditions, the total average power consumption was found to be 1.245 W; which would provide 1712 s (28.5 minutes) of runtime given the 2.1 kJ (160 mA h) internal battery capacity.

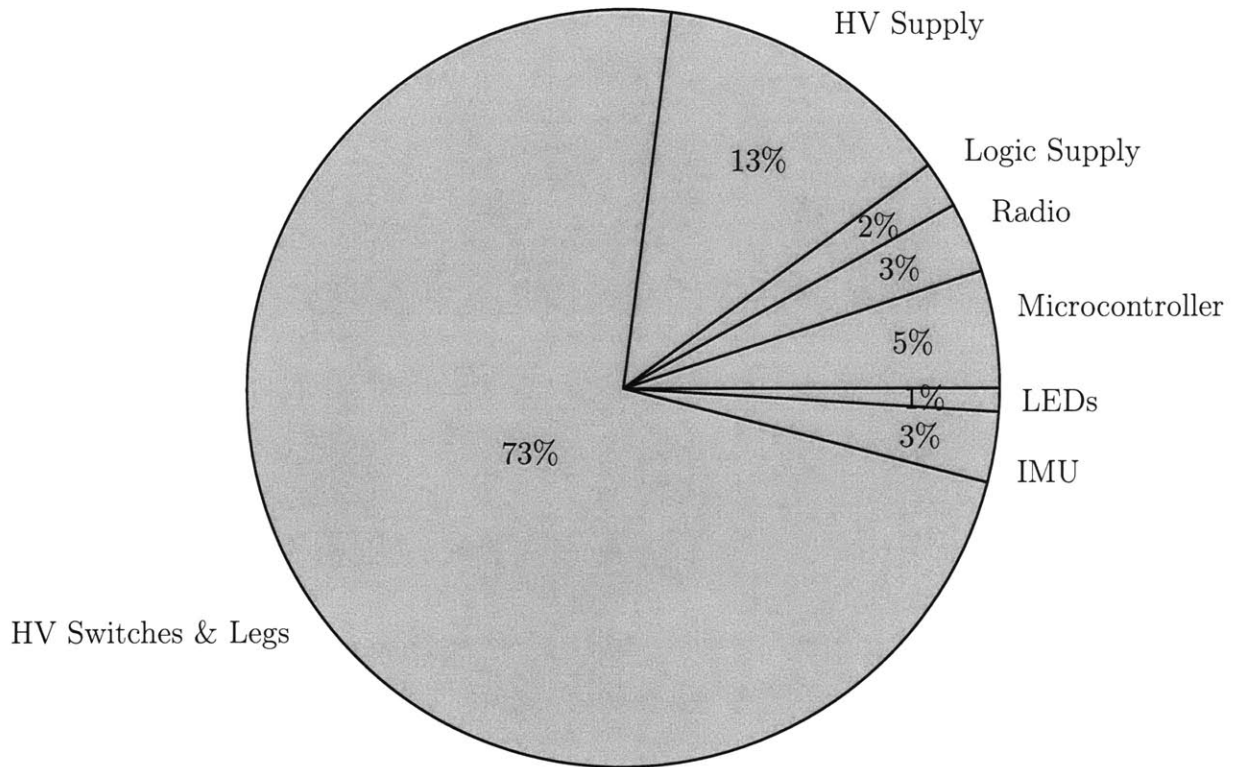


Figure 3-14: Approximate distribution of average power consumption during continuous stepping. The total power draw was 1.245 W.

Characterization and analysis of the Mark V prototype walking characteristics are provided in Chapter 4.

THIS PAGE INTENTIONALLY LEFT BLANK

Chapter 4

Stepping Characteristics

4.1 Apparatus

Step sizes were measured over a range of frequencies using a Michelson-type laser interferometer. A two-frequency HeNe laser (Agilent[®] 5517D) served as the optical source, with a nominal wavelength of $\lambda = 632.991$ nm. The beam was split using a single beam interferometer module (Agilent[®] 10705A) fitted with a retroreflector (Agilent[®] 10704A), which served as the fixed reference arm. A second, smaller retroreflector was constructed from a corner cube element (Thorlabs[®] PS970) and mounted on the ANT prototype as the interferometer's moving arm. The reflected beams were detected by an fiber-coupled remote receiver (Agilent[®] 10780F) connected to a 32-bit three-axis laser board (Agilent[®] N1231A). The aforementioned configuration provided a resolution of $\lambda/1024$, or approximately 0.6 nm, a maximum range of ± 1.3 m, and a maximum measurable velocity of 1 m s^{-1} .

High-energy density neodymium iron boron (NdFeB) magnets (K&J Magnetics[®] R211) coupled the moving arm's retroreflector to the device under test at one of two mounting points. A magnetic mounting point located on one of the three spherical ruby feet was used for measuring the piezoceramic leg frequency response characteristics. The second mounting point, consisting of a ferromagnetic plate located near the ANT's center of mass, was utilized for measuring the body

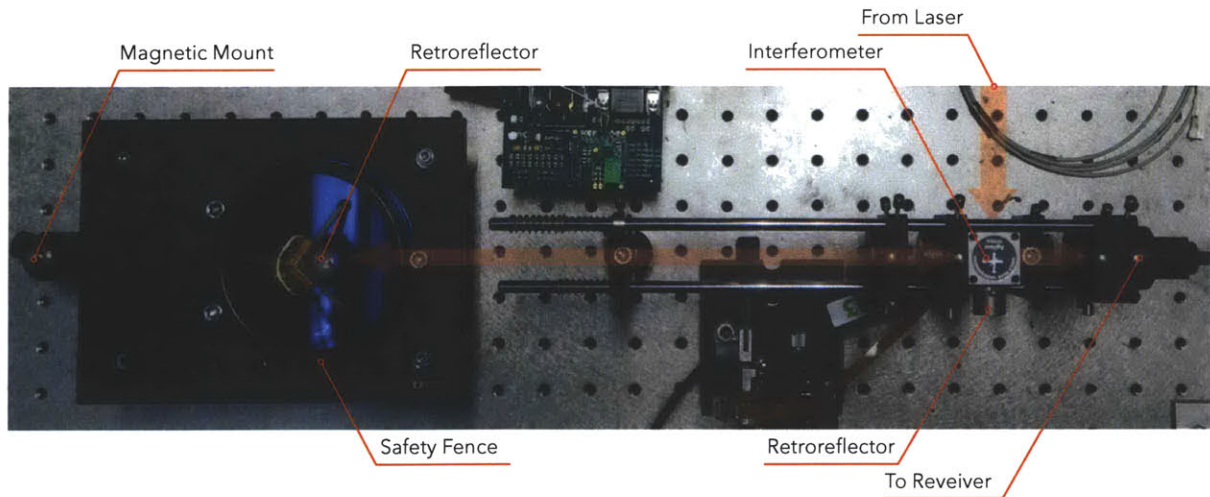


Figure 4-1: Optical measurement apparatus used for determining both leg deflection and step size. Red arrows depict the laser path.

displacement during unidirectional stepping tests.

Driver limitations required that the laser board be interfaced from within Microsoft® Windows operating system. In order to achieve maximum temporal resolution, a console application was written in C++. The program prompted the user to specify the desired name for the file into which measurements would be stored as well as the desired number of samples to acquire. Since the program was to be deployed on a platform that did not provide real-time scheduling. To account for non-uniform sampling, each measurement read from the laser board's registers was assigned a timestamp based on the operating system's high-performance timer. The timestamped data was buffered in RAM before being written to the user-specified output file as tab-delimited plain-text values.

An unpatterned silicon wafer was used as the work surface as it offered high uniformity and flatness. The RMS surface roughness was measured using an AFM (Park Scientific Instruments™ AutoProbe CP-R) and found to be approximately 0.3 nm.

A set of MATLAB® scripts were written to resample and process the raw data. The resampling rate was based on the longest interval between acquired measurements.

4.2 Measurement Procedure

Prior to acquiring measurements of the step size, it was decided that it would be instructive to first examine the frequency response characteristics of a single piezoelectric leg for a given combination of excitation electronics, and software parameters, and boundary conditions (*i.e.*, leg mounting and foot diameter). By examining the response data, an approximate range of potential stepping frequencies could be identified.

The ANT prototype was placed inside of the measurement space, with the chassis-mounted retro-reflector aligned with the beam of the laser interferometer. Remotely, the prototype was issued a “burst” command wherein it would walk at a user-defined stepping frequency for a 100 ms interval towards the interferometer. Whilst executing the command, the laser interferometer was used to obtain a time record of distance measurements. The measurement procedure was repeated multiple times at each frequency over a range of frequencies.

4.3 Results

Figure 4-2 presents the non-parametric frequency response of an unloaded leg undergoing transverse vibrations as a result of single electrode excitation. The plane of motion was aligned to be parallel with the axis of the laser interferometer’s beam. The existence of several resonant peaks is apparent and in agreement with the numerical model. The frequency range between 1 kHz and 1.6 kHz indicated that a fairly monotonic mapping between step size and excitation frequency would be observed when operating within that regime.

Segments from each unidirectional translation dataset were overlaid and the resulting plot has been included in Figure 4-3. Due to the existence of multiple resonant peaks over the selected range of stepping frequencies, the evolution of the average velocity trend among the family of curves was not monotonic with frequency. In particular, this particular ANT prototype attained a peak velocity of approximately 5 mm s^{-1} at a stepping frequency of 1450 Hz, and a minimum velocity of around

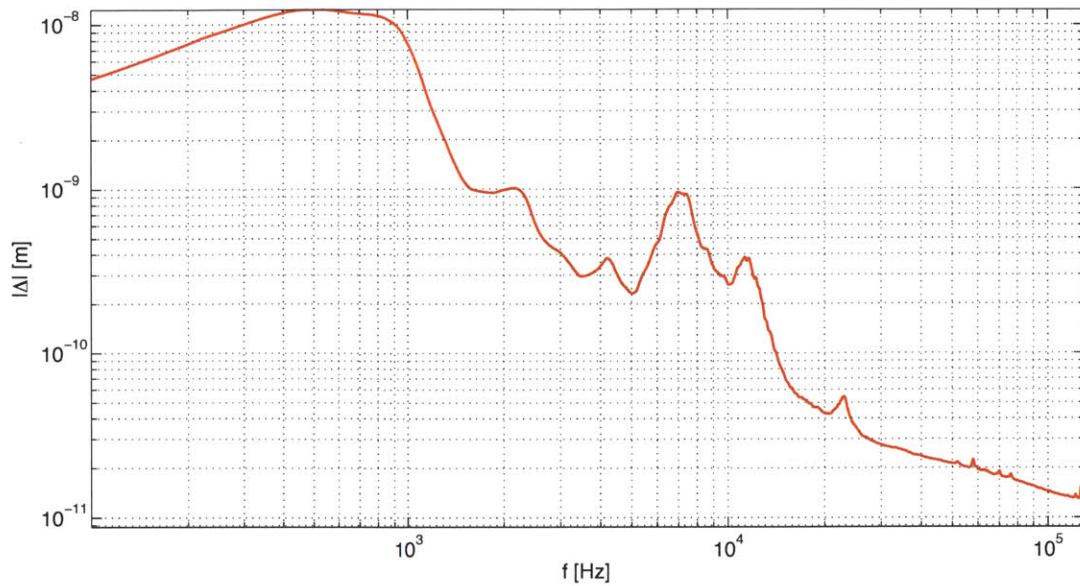


Figure 4-2: Measured frequency response of an unloaded leg subjected to single electrode excitation.

1 mm s^{-1} at a stepping frequency of 600 Hz.

A MATLAB[®] script was written to automate the process of estimating the average step size as a function of stepping frequency. Rather than to assume that each displacement profile had, on average, a constant slope, the script computed the average of the relative displacements between adjacent peaks. In this manner, the number of steps taken during the measurement interval would not significantly affect estimates of step size. The results were plotted as a function of frequency in Figure 4-4.

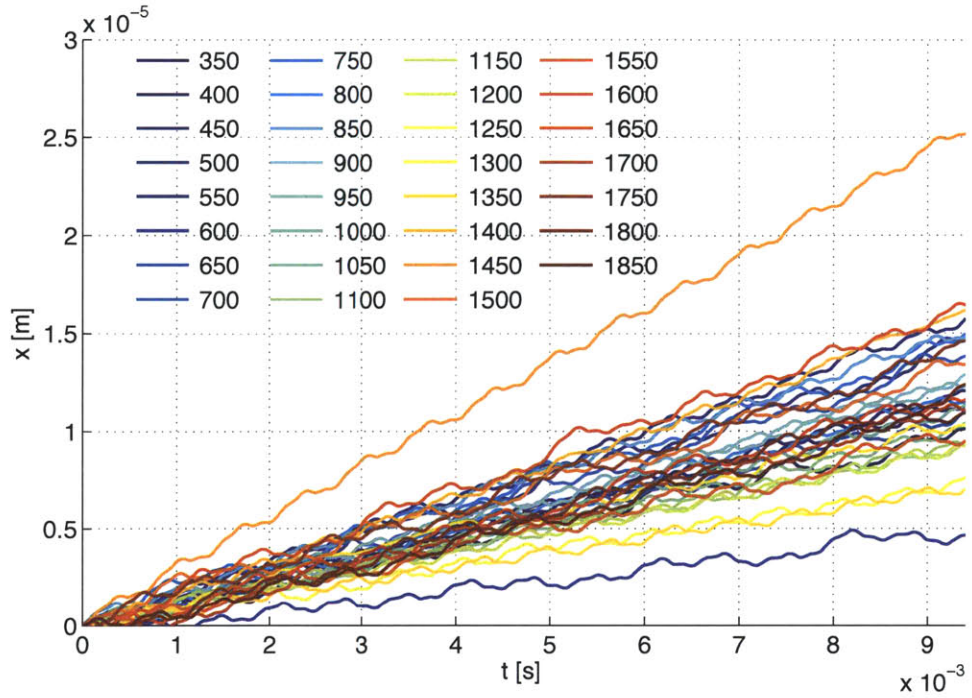


Figure 4-3: Measured body displacement during uni-axial stepping.

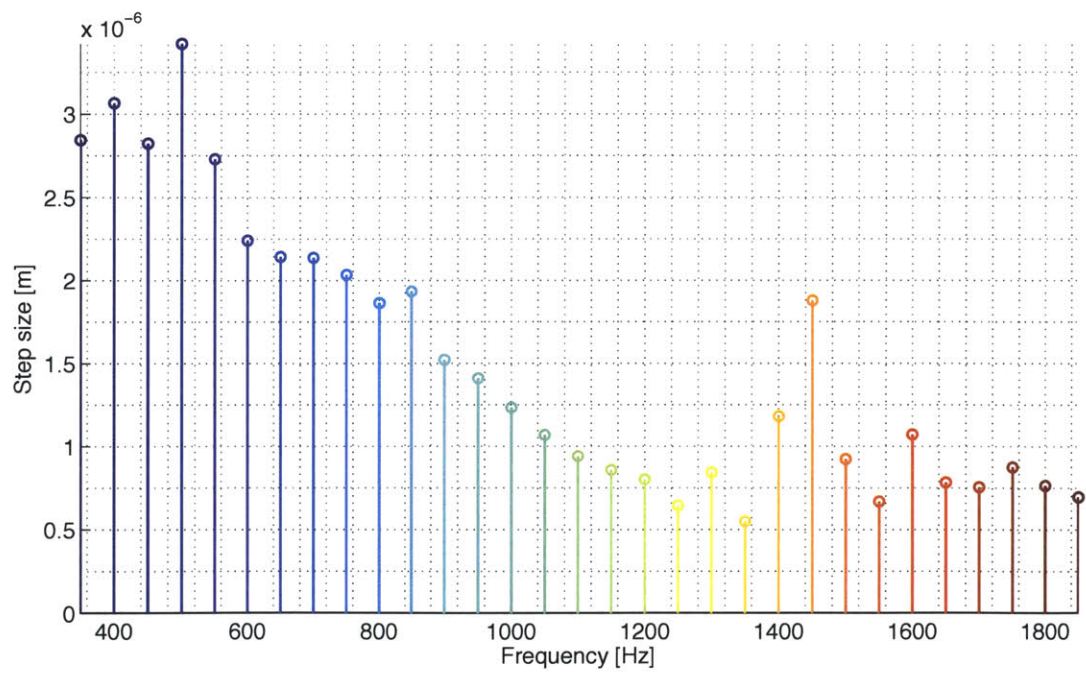


Figure 4-4: Average step size as a function of frequency for a range of excitation voltages.

THIS PAGE INTENTIONALLY LEFT BLANK

Chapter 5

Control and Monitoring

5.1 Firmware

The ANT firmware was designed with a state machine architecture to ensure some degree of deterministic behavior and performance. Software registers were defined to store configuration and data variables; a list is provided in Table 5.1.

5.2 Motion Primitives

Different gaits were implemented as vectorized motion primitives: (i) translation, (ii) counter-clockwise rotation, and (iii) clockwise rotation. For simplicity, only three translation directions were defined – one corresponding to each leg. The binary nature of the leg excitation signals allowed the motion vectors to be conveniently stored as compact 16-bit wide arrays with each of the lower 12-bits corresponding to an individual leg electrode. The length of each array was determined by the number of phases comprising a given gait. Upon receiving a command to step, the firmware enabled the high voltage power supply and configured a hardware timer to periodically trigger an interrupt service routine (ISR) in accordance with the user-defined stepping frequency. Each call of

| Register Name | Description | Unit | Data Type |
|---------------|--|--------------------------|------------------------|
| STATE | Current state | - | uint8_t |
| VBAT | Battery voltage | mV | uint16_t |
| LEDS | LED indicator state | - | uint8_t |
| LOCO_FREQ | Stepping frequency | Hz | uint32_t |
| LOCO_MODE | Stepping motion primitive | - | uint8_t |
| ORIENT_EN | Enable/disable IMU | - | bool |
| ORIENT_ACCX | IMU x -axis acceleration | m s^{-2} | int32_t (Fixed-point) |
| ORIENT_ACCY | IMU y -axis acceleration | m s^{-2} | int32_t (Fixed-point) |
| ORIENT_ACCZ | IMU z -axis acceleration | m s^{-2} | int32_t (Fixed-point) |
| ORIENT_GYRX | IMU x -axis angular rate | $^{\circ} \text{s}^{-1}$ | int32_t (Fixed-point) |
| ORIENT_GYRY | IMU y -axis angular rate | $^{\circ} \text{s}^{-1}$ | int32_t (Fixed-point) |
| ORIENT_GYRZ | IMU z -axis angular rate | $^{\circ} \text{s}^{-1}$ | int32_t (Fixed-point) |
| ORIENT_MAGX | IMU x -axis magnetic flux density | μT | int32_t (Fixed-point) |
| ORIENT_MAGY | IMU y -axis magnetic flux density | μT | int32_t (Fixed-point) |
| ORIENT_MAGZ | IMU z -axis magnetic flux density | μT | int32_t (Fixed-point) |
| ORIENT_MAGY | IMU computed heading angle | $^{\circ}$ | int32_t (Fixed-point) |
| INST_EN | Enable/disable instrumentation | - | bool |
| INST_ADO | ADC channel 0 raw value | - | uint16_t |
| INST_CAPO | Lower 20 bits of normalized ref. TDC value | - | uint32_t |
| INST_CAP1 | CDC channel 1 (normalized by Cref) | F F^{-1} | uint32_t (Fixed-point) |
| INST_CAP2 | CDC channel 2 (normalized by Cref) | F F^{-1} | uint32_t (Fixed-point) |
| INST_CTEMP | CDC internal temperature | $^{\circ}\text{C}$ | uint32_t (Fixed-point) |
| INST_CAP12 | Difference between CDC channels 1 and 2 | F | uint32_t (Fixed-point) |
| INST_CAP1D | Estimated time derivative of CDC channel 1 | F s^{-1} | uint32_t (Fixed-point) |

Table 5.1: ANT configuration and data registers.

the ISR incremented an address counter pointing to an index in the current user-selected motion primitive vector. The indexed value was then used to update the state of the port assigned to control the 12 high voltage switches. A `switch` statement within the ISR resets the address counter after reaching the end of the given vector. The use of look-up tables and the absence of conditional expressions were conscious design choices intended to minimize processor overhead.

5.3 Communication Protocol

Communication between individual ANTs and a central control and data acquisition system is achieved by a proprietary low-latency wireless protocol. A simple packet structure, shown in Table 5.2, was conceived to support the concurrent use of multiple ANTs on a common radio channel, and to facilitate data handling. The total length of each packet was limited to 14 bytes so as to not exceed the size of the microcontroller UART FIFO, freeing the processor to handle other tasks as packets are transmitted and received over the UART interface.

| | Header | | | | | Body | | | | | | | | |
|-------------|--------|-----|-----|-----|-----|------|---|---|---|---|----|----|----|----|
| Packet Byte | 0 | 1 | 2 | 3 | 4 | 5 | 6 | 7 | 8 | 9 | 10 | 11 | 12 | 13 |
| Name | LEN | DST | SRC | CMD | EPC | PYLD | | | | | | | | |

Table 5.2: Communication packet structure.

A description of the packet header bytes is as follows:

- **LEN** The length of the packet payload.
- **DST** The destination address to which the packet is being delivered.
- **SRC** The address of the packet source/origin.
- **CMD** The command code, describing the nature of the packet’s payload.
- **EPC** An epoch number indicating if the current packet payload part of a multi-packet series.

Table 5.3 summarizes the network address mapping scheme. The network is primarily intended to operate with a star structure, though the firmware was designed to readily accommodate a mesh topology if needed. In the star network, there was no direct communication among ANTs; instead, all communication was passed to the server via a Coordinator - a radio-equipped USB dongle running the ANT communication stack. Regardless of the interface, packets received by the coordinator are processed by a low-latency look-up table. Depending on the destination address (DST), a received packet would either be forwarded to the server (DST = 0) via the wired (UART) communication interface or to an ANT via the wireless interface (DST = 2...255).

| Network Address | Device |
|-----------------|--------------------------|
| 0 | Server (computer) |
| 1 | Coordinator (USB dongle) |
| 2-255 | ANTs |

Table 5.3: Network address assignment.

The packet payload (PYLD) may contain one to nine bytes depending on the nature of the packet. A typical packets containing data from a 32-bit ANT register will have a payload length of 9-bytes (LEN = 9). The first byte (REG) contains the enumerated address of the pertinent ANT register. The following four bytes (DATAx) contain the 32-bit data value cast as four bit-shifted bytes. Similarly, the final four payload bytes (TIMEx) store a 32-bit timestamp that was generated when the data value was acquired.

| | Address | Data | | | | Timestamp | | | |
|--------------|---------|-------|-------|-------|-------|-----------|-------|-------|-------|
| Payload Byte | 0 | 1 | 2 | 3 | 4 | 5 | 6 | 7 | 8 |
| Name | REG | DATA0 | DATA1 | DATA2 | DATA3 | TIME0 | TIME1 | TIME2 | TIME3 |

Table 5.4: Data packet payload structure.

The command byte (CMD) is populated with a valid command code, instructing the receiving device as to how the packet is to be handled. A list of the supported commands is provided in Table 5.5.

| Command | Description |
|----------------|--|
| READ_REQUEST | Node A requesting to read a register on Node B |
| READ_RESPONSE | Node B responding to read request from Node A |
| WRITE_REQUEST | Node A requesting to write to a register on Node B |
| WRITE_RESPONSE | Node B responding to Node A's request to write |
| LIST_REQUEST | Node A requesting a list of Node B's registers |
| LIST_RESPONSE | Node B responding to Node A's request for register list |
| DUMP_REQUEST | Node A requesting for Node B to dump all register contents |
| DUMP_RESPONSE | Contents from Node B register dump |

Table 5.5: ANT protocol commands, where Node A and Node B represent two devices running the ANT firmware.

5.4 Heading Estimation

Measurements from the onboard 9-axis IMU, found on the Mark IV and Mark V prototypes, were used to compute estimates of the device heading. The three-axis magnetometer provided measurements of the local geomagnetic field within the sensor's frame of reference, which resided on one of the angled faces of the ANT body. A fixed-point tilt-compensation algorithm [42] was applied in order to convert the measurements from the sensor frame to the ANT reference frame using output from the three-axis accelerometer. The compensated measurements were then used to compute heading angle, thus providing the user with an estimate of the device orientation.

5.5 Server-Side Hardware

Small USB dongles, such as the one shown in Figure 5-1, sharing a common microcontroller/radio circuit layout and firmware with the ANT devices, were developed to allow computers to readily interface with ANTs. A UART to Full Speed USB bridge (FTDI[®] FT234XD) interfaced the computer running the server with the microcontroller running the ANT communication stack. This particular USB bridge IC was selected to ensure compatibility with all major operating systems, in order to maintain overall system accessibility and flexibility. An overview of the ANT network topology is provided in Figure 5-2. When connected, the USB dongle behaved as a virtual serial

COM Port (VCP), allowing end-users to create a customized software interface using a platform of their choosing. An example of such an interface was realized to demonstrate the flexibility of this architecture.

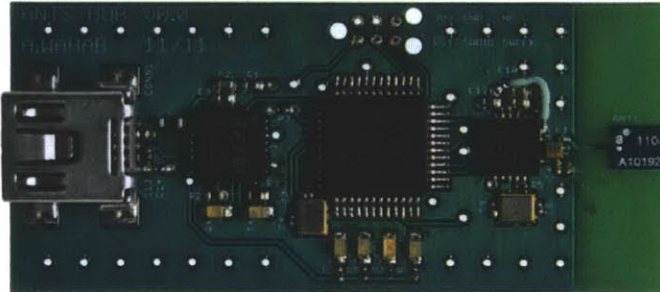


Figure 5-1: USB radio dongle (20 mm × 45 mm). From left to right: micro-USB port, USB-to-UART converter, microcontroller, radio transceiver, and chip antenna.

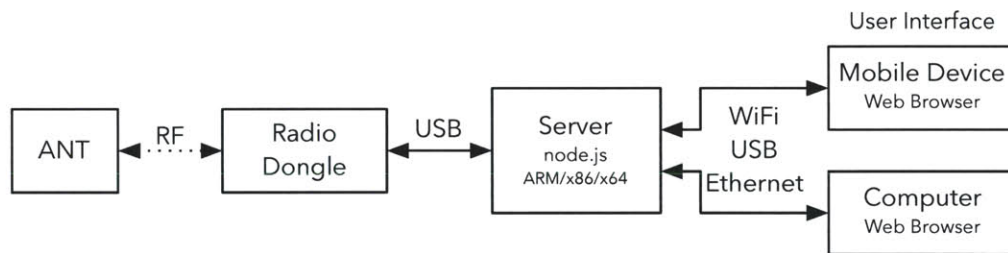


Figure 5-2: ANT network structure.

5.6 Server

A server application was developed using node.js, an open source server-side JavaScript platform targeted at event-driven, scalable, real-time applications [9]. Developing the server application in JavaScript allowed for a common codebase to be shared by the server and browser-based client-side applications, thus improving maintainability and reducing development time. node.js is based on the high performance V8 JavaScript engine, which provides performance that is comparable to unoptimized C code and runs on a wide range of platforms (*i.e.*, Microsoft® Windows, Apple® OS X, and Linux® systems with an x86, x64, or ARM® processor). At runtime, the server began

monitoring for traffic over both the VCP associated with the radio dongle and the WebSocket module [2], the latter of which handled communication with the user interface. Bytes received over the serial port were shifted into a buffer until a full packet was received; a timeout function handled incomplete packets by flushing the buffer. Completed packets were then parsed and routed to the destination address specified in the packet header. Case structures, instead of conditional statements, were used to handle parsing and routing tasks for increased performance. Similarly, packets received via the WebSocket interface were parsed and routed to their respective destinations.

The server broadcasted updates destined for the user interface, allowing multiple connected clients to remain synchronized. Packets received from the user interface containing commands or modified register values were rebroadcasted to all connected clients, regardless of the original packet's destination address.

Server communication may be easily expanded to interface with third-party applications, should users wish to do so. The node.js platform natively supports communication via TCP as do most common programming languages/environments used by scientists and engineers (*e.g.*, C/C++, Python[™], MATLAB[®], LabVIEW[™], and Mathematica[®]).

5.7 User Interface

Staying true to the project's vision of remaining open source and platform independent, the graphical front-end was designed as a web app, constructed strictly using web-standard languages: HTML, JavaScript, and CSS. As such, users may control and monitor one or more ANTs via any web-enabled device. Additionally, client-server communications were broadcasted, permitting synchronization across all connected devices. The user interface (UI) was designed to support input via keyboard, mouse, and touch-interface. Figure 5-3 contains a screen capture of the UI running within the browser.

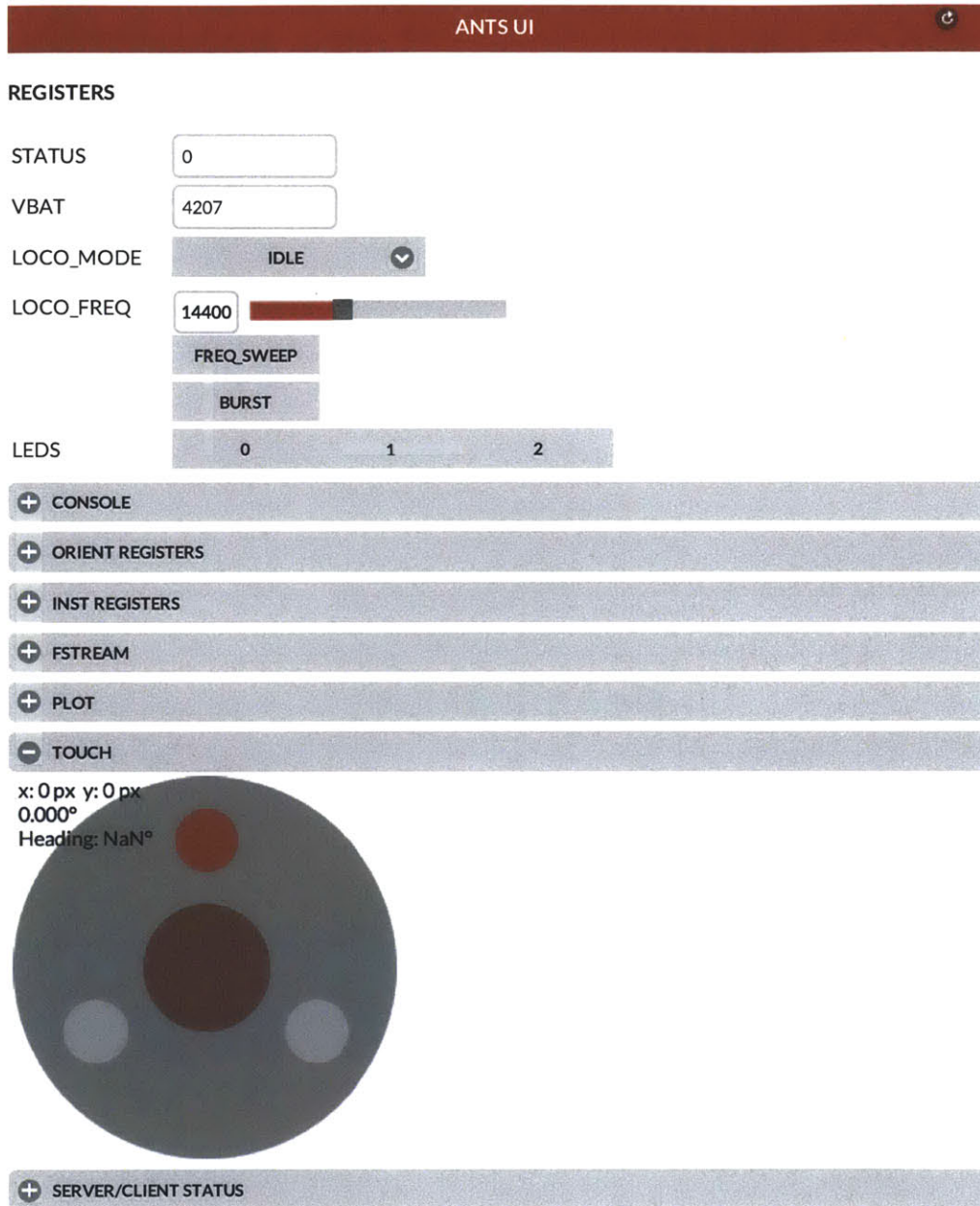


Figure 5-3: A screen capture of the ANTS UI. Basic status and control registers and the manual control joystick are visible.

5.7.1 Joystick

The on-screen joystick could be used to manually control an ANT using a mouse or touch-interface. Dragging the center circular element in a radial commanded the ANT to translate in the corresponding direction. The distance between the draggable element its idle position at the center of the joystick was mapped to stepping frequency; increasing radial distance was mapped to lower frequency, and thus resulting in an increase in step size. The outer ring could be used to rotate the ANT in the clockwise or counter-clockwise direction by clicking on, or touching, a part of the ring and dragging in a circular motion. Releasing the mouse button or removing one's finger caused the joystick elements to return to their idle position, whilst issuing a command to the ANT causing it to enter a low power idle state.

5.7.2 Plotting

A specialized plotting system was devised in an effort to efficiently handle visualization of multiple data streams on client systems with limited processing resources, such as handheld mobile devices. A set of client-side JavaScript plotting routines were created to plot one or more variables on a common axis. For robustness, no assumptions were made regarding the differences in sampling rates or the uniformity of sampling intervals. Each data stream was plotted to its own layer within an HTML canvas object. Rather than updating the entire canvas each time a new data point was received, only a narrow slice of the relevant layer was cleared and updated, much akin to the sweeping display mode of an oscilloscope, though each channel was updated independently and asynchronously. User inputs were provided to allow real-time scaling of each data stream in both time and amplitude, as well as the addition of a constant offset. A screen capture of the plotting section has been included in Figure 5-4.

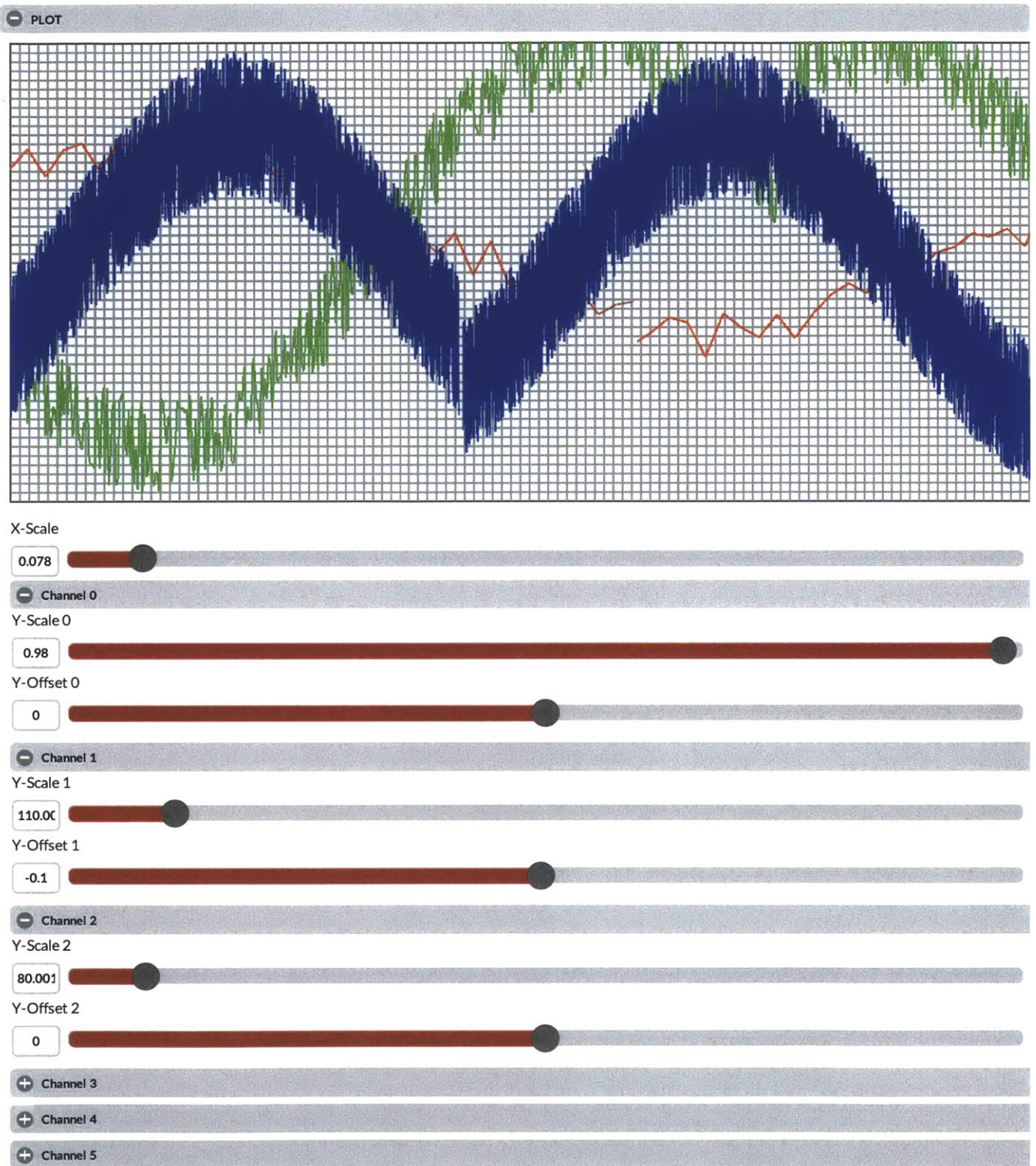


Figure 5-4: The ANTS UI plotting section allows users to easily monitor multiple asynchronous data streams in real-time. New canvas layers were dynamically generated as additional data streams are added. Notice how each layer was updated independently as new data is pushed from the server to the client.

Chapter 6

Instrumentation Example: Capacitive Probe

A novel type of low-cost, high-resolution capacitive probe was developed to demonstrate a means by which an ANT may be functionalized to operate as an application specific precision instrument.

6.1 Probe Fabrication

The probe design is coaxial in nature, constructed of alternating concentric conductive and insulating dielectric layers, as seen in Figure 6-1. A 0.635 mm diameter tungsten scanning tunneling microscopy (STM) probe (Signatone[®] SE-TB) was selected to serve as the conductive core. The STM probe was selected on account of its stiffness, straightness, fine tip diameter (25 μm), and availability within the lab; lower-cost mass produced probes would likely be fabricated from copper. In order to improve solder affinity, the probe was electroplated using a simple electrochemical cell and copper sulfate solution. After plating, a uniform 40 μm thick layer of Parylene-C (GALENTIS[®] Galxyl C) was applied via chemical vapour deposition (Para Tech Coating[®] LabTop 3000). In order to form the probe's second conductor, a sub-micrometer thick seed layer of silver was added over the dielectric using a sputter coater (Denton Vacuum[®] Desk V). The silvered surface of each probe was then electroplated with copper to increase the layer's thickness and solderability. A final conformal coating of Parylene-C, measuring 20 μm thick, was deposited to protect the outer conductor from

mechanical damage.

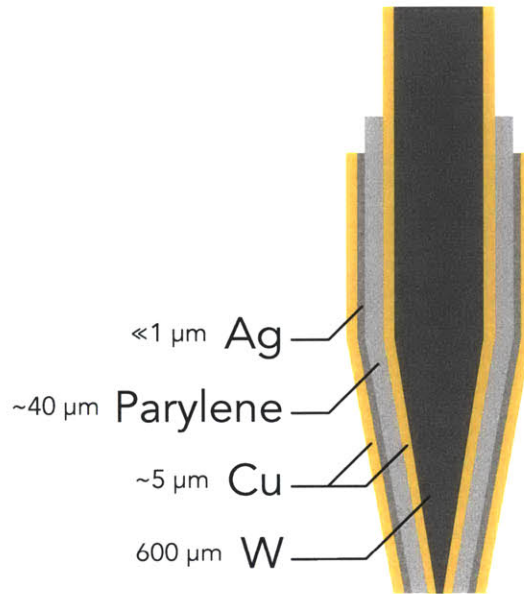


Figure 6-1: Cross-sectional representation of capacitive probe illustrating the layered construction.

The probes were then trimmed to length by removing excess material from the blunt end. In order to establish electrical connections with the measurement electronics, isolated portions of the two conductive layers were exposed by mechanically removing intermediate material. The pointed tips of the conductive cores were then exposed using a diamond grinder.

6.2 Measurement Electronics

Capacitance may be measured with a high-degree of precision using an integrated capacitance-to-digital converter (CDC). Conventional 16- and 24-bit CDCs are based on sigma-delta ($\Sigma\Delta$) converters capable of resolving changes in capacitance as low as 1 fF. An alternative approach to measuring capacitance involves connecting the unknown capacitance to a known resistance, applying a step input voltage, and measuring the RC time constant. Integrated solutions based on time-to-digital converters (TDC), with high-resolution timers and internal temperature compensation are capable of resolving capacitance changes of less than 10 aF. As with all CDCs, there is an inverse

relationship between the effective sampling rate (after oversampling and averaging) and resolution.

Due to their higher resolution, a TDC-based CDC solution (acam[®] PCap01) was selected to directly measure the changes in the effective probe capacitance. The CDC featured an internal, 48-bit user-programmable DSP, 48 × 48-bit data RAM, onboard clock, internal temperature measurement, and compensation for internal and external parasitic capacitances in a compact 4 mm × 4 mm QFN24 package. A precision 42 pF capacitor was connected as a floating reference, allowing absolute values of capacitance to be obtained. Communication between the CDC and microcontroller was carried out via the I²C serial bus. A 3.0 V LDO linear regulator provided a low-noise point-of-load supply rail.

A coaxial RF receptacle (Hirose[®] MS-147(06)) was selected as a mount for the capacitive probe. A short length of 0.8 mm diameter two-conductor coaxial cable (Murata[®] MXJA01JA0500) connected the two probe electrodes to the CDC.

6.3 Evaluation

An apparatus, shown in Figure 6-2, was constructed to provide a first-order evaluation the capacitive probe microscope's performance. Two linear actuators were used to vary both the probe-sample gap distance and position along the scan while measuring the spatial variation in capacitance as a function of both parameters.

A preloaded piezoelectric stack actuator (Physik Instrumente[®] P-841.20) modulated the probe along its center axis, resulting in a variable probe-sample gap distance l_{gap} . The actuator was driven by a high-voltage amplifier (Physik Instrumente[®] E-505.00), which was controlled via analog input. A 16-bit DAC (National Instruments[®] USB-6215) generated quasi-static analog command voltages that were provided as input to the amplifier. A laser interferometer was used to measure the value of l_{gap} , where the reference position ($l_{gap} = 0$ mm) was taken as the position where probe and conductive portion of the sample were in contact, resulting in a short-circuit between the probe's core and outer electrodes.

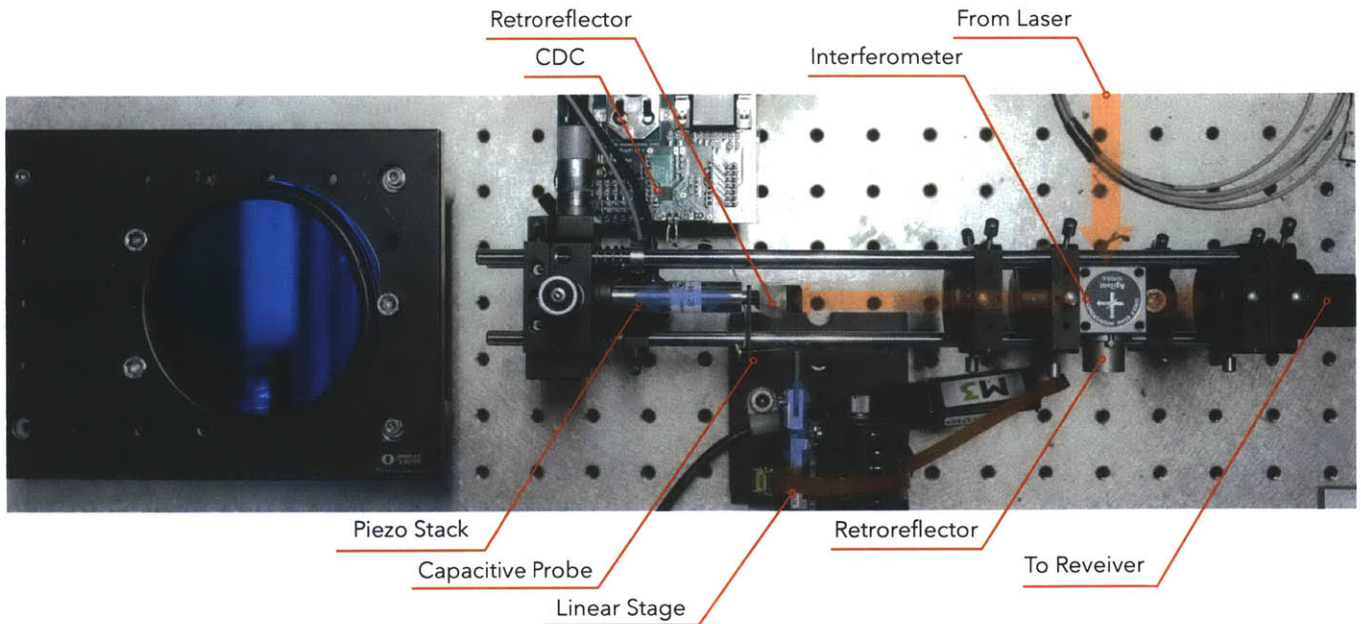


Figure 6-2: Apparatus for characterizing the capacitive probe microscope. Red arrows depict the laser path, blue arrows indicate the motion axes.

Motion along the scan axis x was produced by a precision linear motion module (New Scale Technologies[®] M3-L), which moved the sample transversely across the probe tip. The linear motion module featured closed-loop position control with a resolution of $0.5 \mu\text{m}$ over a 6 mm range of travel. Position commands were issued via serial interface. An integrated 12-bit magnetic sensor (Austria Micro Systems[®] NSE-5310) provided absolute position measurements.

At each gap distance l_{gap} , a series of capacitance measurements were obtained at discrete positions along the scan axis x . Each measurement consisted of 3000 samples that were averaged by the CDC's internal DSP, which also compensated for temperature fluctuations. To mitigate spatial error due to backlash in the linear motion module, measurements were only taken when scanning the sample in one direction; the linear stage position was reset once the end of travel was reached.

The sample consisted of a small piece of "0.5-oz" copper-clad FR-4 from which half of the copper had been etched away. The scan axis was selected to be perpendicular to the edge of the etched region, thus approximating a spatial step-change in sample conductivity.

The measured edge response for various gap distances is included in Figure 6-3. At a scan position

of $x = 0$ mm, the probe tip is located entirely above the metal-clad portion of the sample. As expected, the net capacitance decreased as the probe's position moved from the metallic region to the non-conductive region, as well as increasing gap distance.

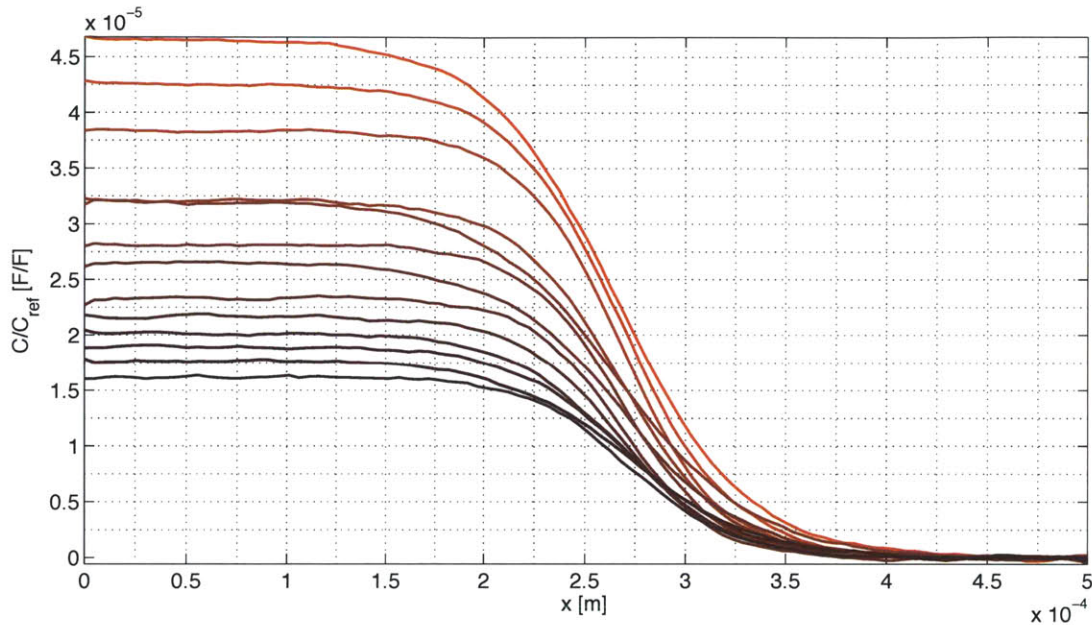


Figure 6-3: Measured edge response.

The edge response may be used to estimate the system's resolution as a function of l_{gap} using the 10% to 90% distance. That is to say, at a given gap distance, the spatial difference Δx , calculated between the positions corresponding to the 10th and 90th percentiles of the edge response data is representative of the probe's spatial resolution. The computed estimates of the probe's resolution are plotted in Figure 6-4.

The line spread function (LSF) may be estimated directly by computing the spatial deviated of the edge response data. As Figure 6-5 suggests, the LSF is effectively a one-dimensional slice of the imaging system's point-spread function (PSF). As one might expect, as the gap distance was increased, the amplitude and width of the LSF decreased and increased, respectively.

The width of the LSF is typically expressed as the full-width-at-half-maximum (FWHM), which is

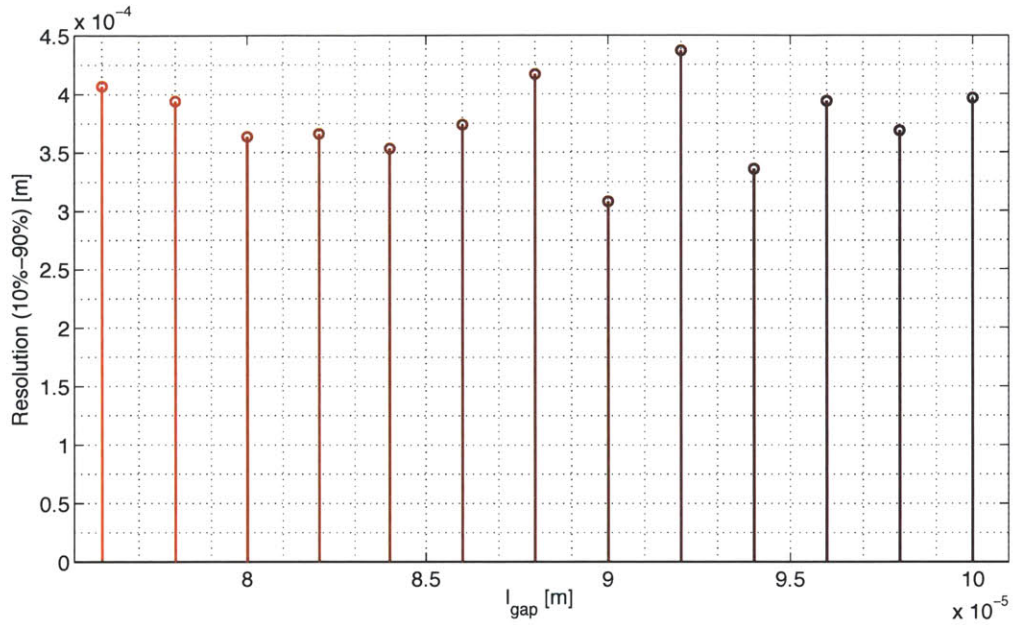


Figure 6-4: Computed resolution of a capacitive probe based on 10%-90% criterion.

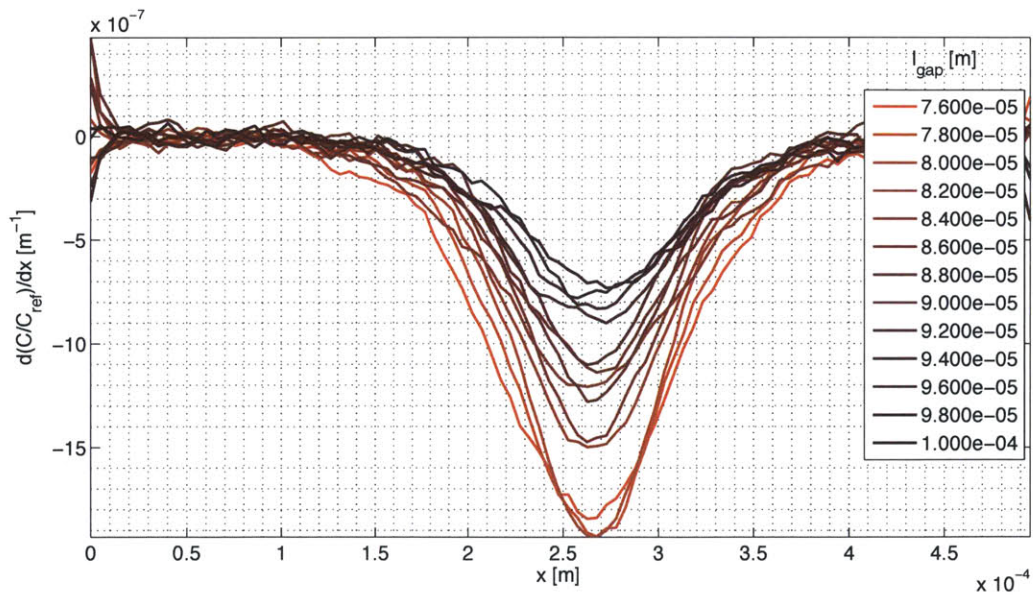


Figure 6-5: Computed line spread function.

simply the spatial difference computed at half of the LSF's peak value. The widths of the family of LSF curves is included in Figure 6-6 for completeness.

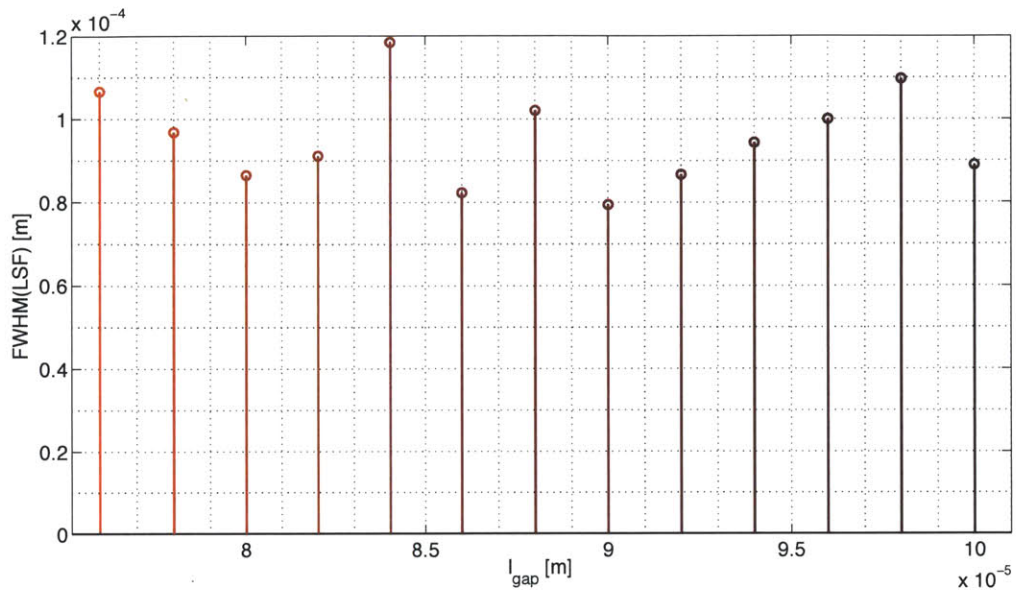


Figure 6-6: Computed line spread function.

THIS PAGE INTENTIONALLY LEFT BLANK

Chapter 7

Positioning

7.1 Positioning Systems

A variety of solutions were considered for performing closed-loop position control of one or more ANTs within a workspace. Figure 7-1 highlights three of the most promising architectures. The two leftmost approaches may be viewed as global positioning systems, wherein the position of each individual ANT within the workspace would be measured with respect to a fixed global reference by a downward-facing overhead optical sensor. The rightmost diagram illustrates a distributed positioning scheme, in which each individual ANT would be equipped with a downward facing camera and onboard processing capabilities for performing relative position control, as well as localization in the absolute frame given an appropriately patterned work surface.

7.2 Centralized Positioning

For the centralized positioning schemes, an eye-in-the-sky approach was considered. A downward-facing two-dimensional position sensor would be installed above the workspace; a real-time controller would continuously monitor the workspace, periodically transmitting absolute position and

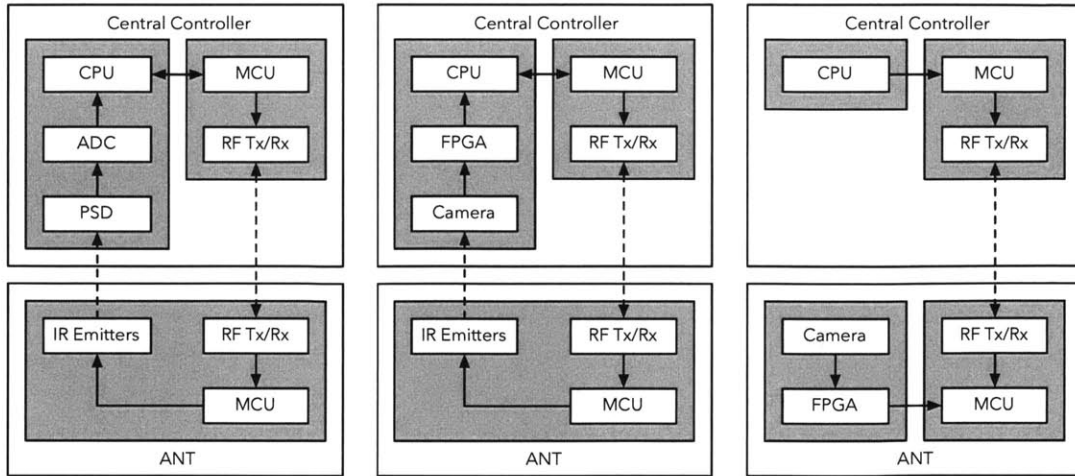


Figure 7-1: Proposed approaches for position measurement.

orientation information to individual ANTs via the wireless communication link.

7.2.1 Position Sensitive Device

Two different sensor technologies were considered: two-dimensional lateral-effect photodiodes and digital imaging sensors. The former, often ambiguously referred to as position sensitive devices, or PSDs, are inherently analog in nature and thus provide continuous position measurements. A rectangular photosensitive PIN diode comprises the active portion of the sensor, generating currents when exposed to light. Electrodes positioned along the four edges of the diode are used to measure the currents, thus allowing one to determine the position of the incident light's centroid. After calibrating for geometric nonlinearities introduced by the PSD and accompanying optics, the position of a point source of light within a plane parallel to that of the sensor will obey a linear relationship. With careful amplifier design and the use of high-quality optics may, one may resolve sub-micrometer displacements. This type of position sensor was previously used in the NanoWalker project [38].

In order to effectively determine the position and orientation of multiple ANTs using a PSD, each ANT could be equipped with photoemitters; near-infrared emitters would be well suited for this purpose since the peak quantum efficiency of most PSDs occurs around 900 nm. While one emitter

would be sufficient for performing position measurements, two or more emitters illuminated in a round-robin scheme, would allow for estimates of orientation as well. The central controller would periodically “ping” each ANT, also in a round-robin manner, requesting for a given unit to cycle its photoemitters to obtain a position measurement. PSDs are often specified with bandwidths in excess of 100 kHz, however the transimpedance amplifiers, which convert the photocurrents to voltages prior to digitization, and the intensity of the light source may both limit the actual bandwidth by several orders of magnitude. Lower bandwidth would likely limit the number of ANTs that could be tracked concurrently, as well as potentially limit the maximum stepping speed.

A two-axis motorized gantry system, similar to that which was used in [35] and illustrated in Figure 7-2, was constructed to evaluate the PSD-based positioning scheme. An orthogonal pair of motorized lead-screw motion stages (Parker[®] 404XR Series) were mounted to a three-legged frame constructed from 100 mm × 50 mm aluminum extrusion (mk[®] 50 Series). Each stage was actuated by stepper motor and indexing drive controller (Parker[®] ZETA4). In order to account for backlash in the leadscrew mechanisms, high-resolution optical linear encoders (Renishaw[®] RGH22) were used to measure the position of each stage. A duolateral silicon PSD module (On-Trak[®] PSM 2-20) and accompanying position sensing amplifier (On-Trak[®] OT-301), were suspended below the gantry system. The PSD was fitted with a 50 mm f/1.8 prime lens (Nikon AF NIKKOR) to increase the field of view.

During normal operation, the PSD would remain in a fixed position, centered over the workspace, however in order to accurately measure position, it was necessary to first establish a mapping between the PSD output and x and y coordinates within the workspace. A “dummy” ANT equipped with three IR emitters was placed at the center of the workspace. By scanning the PSD over an area containing the stationary emitters, it was possible to obtain the sought-after relationship.

A programmable automation controller (National Instruments[®] cRIO-9074) was used to control the motion stages and acquire samples of the V_x and V_y voltages output by the PSD amplifier along with the measured PSD position. A diagram illustrating the programmed scan path is included in Figure 7-3. In order to maximize the accuracy of the resulting measurements, the motion stages

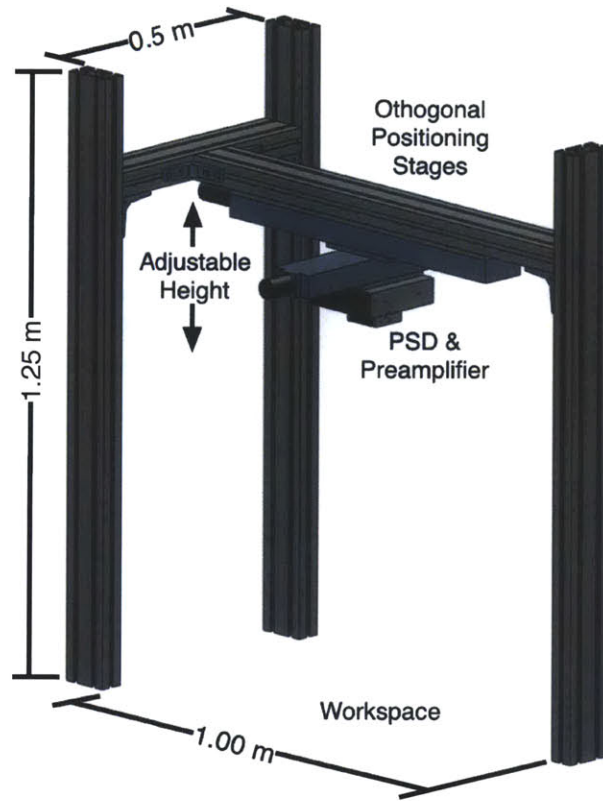


Figure 7-2: A gantry system that was constructed to explore the use of a PSD for two-dimensional positioning.

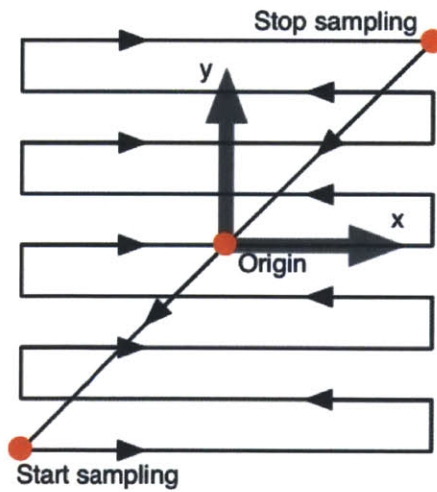


Figure 7-3: The scan path used for mapping the relationship between the two PSD voltage output channels and absolute position within the workspace.

were commanded to briefly pause at each measurement location and given sufficient time settle.

Plots of the normalized outputs from the PSD amplifier are provided in Figure 7-4. As expected, the mappings were both monotonic and superficially planar.

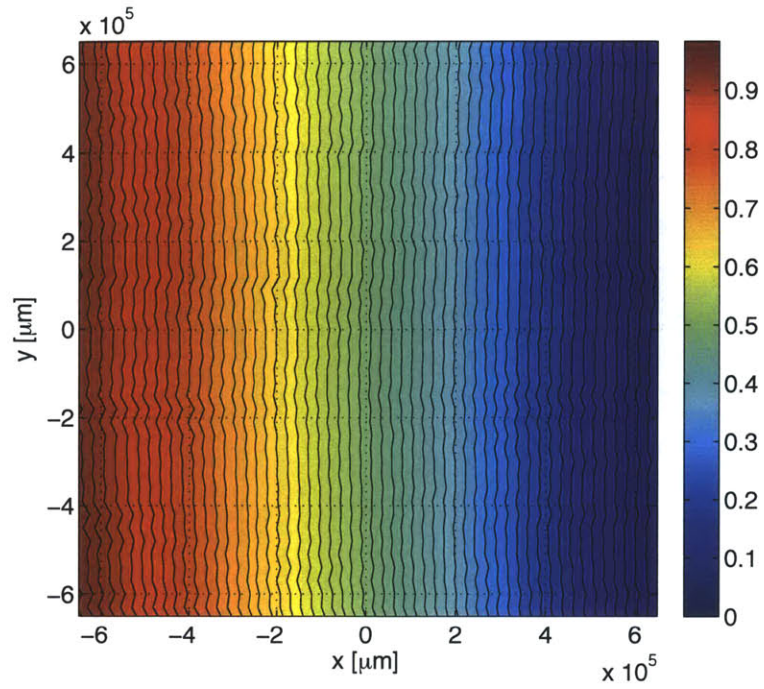
7.2.2 Digital Imaging Sensor

A downward-facing digital imaging sensor, such as the high-resolution CMOS devices found in modern cameras, is an attractive alternative to PSDs. A single digital image of the workspace would provide sufficient information to determine the position and orientation of each ANT within the field of view. Current generation multi-megapixel CMOS arrays and high quality optics might provide positioning accuracy on the order of a few micrometers¹. Image processing methods based on color detection and template matching techniques may be readily applied in real-time given sufficient computational resources. Template matching, for example, may be performed by computing the two-dimensional cross-correlation between an acquired frame of the workspace containing one or more ANTs, and a characteristic model or template image of an ANT.

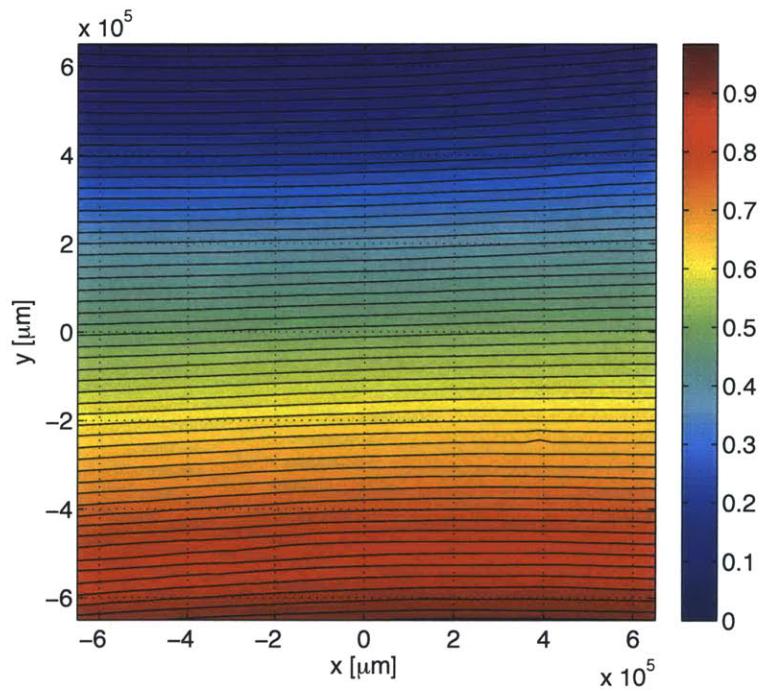
The two-dimensional cross-correlation may succinctly be described as the sum of products of the pixel intensity values from two images. One frame is shifted with respect to the other, and at each position the overlapping pixel values are multiplied and the resulting products are then added together. The process is repeated for all shift positions, resulting in a 2-D array containing the sums of products, whose maximum value represents the relative position of peak correlation between the two original frames. The process by which a template, or partial frame, B is incrementally shifted with respect to a full-frame A is depicted in Figure 7-5. By convention, the image coordinate system origin is located at the top left of the frame, with the horizontal u -axis and vertical v -axis oriented from left to right and top-to-bottom, respectively.

Mathematically, the cross-correlation between square arrays A and B of size $N \times N$ and $M \times M$,

¹Given a $0.5 \text{ m} \times 0.5 \text{ m}$ workspace, 1 m working distance, and 25 mm sensor format, one may obtain a resolution of roughly $5 \mu\text{m}$ to $10 \mu\text{m}$ using high-quality precision optics.



(a)



(b)

Figure 7-4: Spatial plots of normalized PSD amplifier output voltages (a) V_x and (b) V_y .

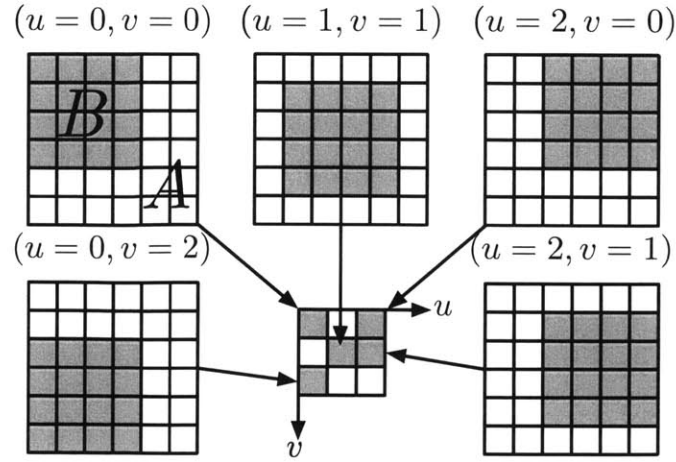


Figure 7-5: The pixel-by-pixel shifting process that occurs when computing the cross-correlation..

respectively, may be written as

$$R_{AB}(u, v) = \sum_{i=0}^{M-1} \sum_{j=0}^{M-1} A(i+u, j+v)B(i, j) \quad \Bigg| \quad (u, v) = 0 \dots (N - M + 1), \quad (7.1)$$

where i and j represent the row and column indices for a given set of horizontal and vertical shifts, u and v . The resulting cross-correlation array R_{AB} is of size $P \times P$, where $P = (N - M + 1)$. A peak value within R_{AB} occurs at the position of maximum correlation, and expressed in terms of a relative displacements, $(u, v)_{\text{peak}}$.

Further discussion, detailing some practical considerations, is provided below, in reference to the proposed Distributed Positioning scheme.

7.3 Distributed Positioning

Unlike the aforementioned positioning schemes, a distributed positioning system would not require a centralized measurement and control system. Instead, each ANT would be equipped with its own onboard positioning system that is capable of estimating relative or absolute position and orientation. The feasibility of implementing a low-power, integrated vision-based positioning system was explored, resulting in the development of preliminary hardware designs.

The design estimated inter-frame displacements by computing the 2-D cross-correlation of images taken of a highly localized section of the workspace surface immediately below a given ANT. The salient hardware components required to implement such a system included a downward-facing camera and a digital processor to compute inter-frame displacements.

An integrated camera module (OmniVision[®] OVM7690) containing focusing optics (1.15 mm focal length, $f/3.0$), a CMOS imaging sensor (1.95 mm format, 640×480 pixel), and electronics for A/D conversion (8-bit/pixel), timing (6 – 27 MHz, 30/60 fps), and basic control (exposure, scaling, sub-sampling, lens correction) was selected as the surface imaging device. The module provided a solution that was both compact ($2.5 \text{ mm} \times 3 \text{ mm} \times 2.5 \text{ mm}$), and low-power (100 mW active, 66 μ W standby).

Whilst processing video and image data using a microprocessor is convenient from a development standpoint, high clock rates are often required to satisfy frame-rate requirements and minimize the processor's pure delay - two key parameters when designing a real-time vision system. Furthermore, the power consumed by a microprocessor generally increases linearly with clock rate, which is undesirable for when the system is to be deployed on a mobile platform with limited energy storage. Clock rates may be reduced by parallelizing the processing operation and through a judicious use of pipelining, noting that the latter may result in increased pure delay. The vast majority of commercially available embedded microprocessors are single-core devices, and are thus not suited for performing performing parallel operations. Due to the shortcomings of the available technology, a custom hardware-based image processor was developed and implemented on a field programmable gate array (FPGA). A Flash-based FPGA (Actel[®] AGLN250) was selected to serve as the target device as it offered a desirable balance of low power consumption, a relatively small footprint (available in both a $5 \text{ mm} \times 5 \text{ mm}$ CS81 and a $14 \text{ mm} \times 14 \text{ mm}$ QFP100 packages), low cost, logic-element count (250,000), and integrated peripherals (Block RAM, PLL).

Figure 7-6 provides an overview, depicting the subsystem modules and key signals that were implemented within the FPGA fabric, and their relationship with respect to the camera. A PLL module generated clock signals that were used to drive the camera and internal logic. When actively ac-

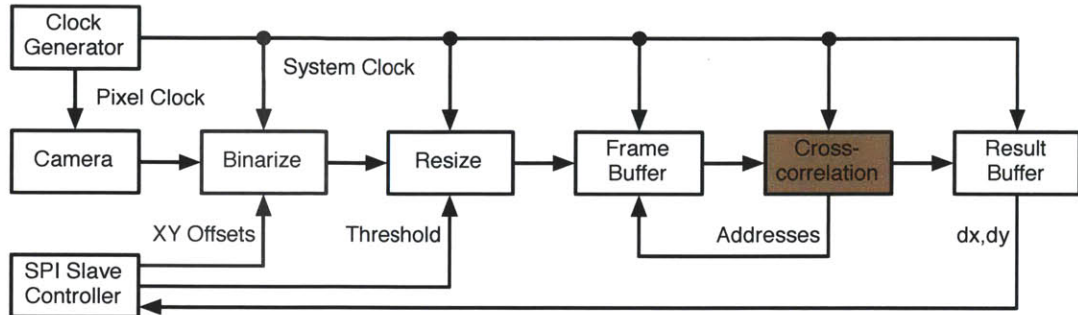


Figure 7-6: An overview of the FPGA subsystems and signal flow. Note that the “Binarize” process is shown in grey, as it may be omitted for implementations where increased dynamic range and resolution are required.

| Signal | Description |
|-------------|------------------------------|
| PCLK | Pixel clock |
| D0 . . . D7 | Pixel intensity; 8-bit value |
| VSYNC | Vertical/frame sync |
| HREF | Horizontal/line reference |

Table 7.1: Camera output signals.

quiring images, the camera output 11 signals, which are tabulated in Table 7.1, which were routed directly to corresponding input pins on the FPGA. The `VSYNC` signal was used to reset a row counter and indicate the start and end of each frame, while the `HREF` signal incremented the row counter. Full 8-bit wide pixel values (`D0 . . . D7`) were registered on the rising edge of `PCLK`. Pixel values were then passed to an optional Binarization module, which converted the 8-bit intensity data to 1-bit values by comparing with a user-defined threshold. The Resize module then discarded or retained individual pixels based on values stored in user-defined configuration registers, which specified the region of interest in terms of dimensions and offset. Pixels were discarded by effectively cropping the frame, thus retaining pixels near the center of the CMOS array, which would incur the least amount of distortion due to the geometry of the lens. The retained pixel values were then stored in one of three banks of SRAM, which served as input frame buffers for the 2-D cross-correlation module. Results from the cross-correlation were then registered in a result buffer, which could be accessed by the ANT microcontroller via serial interface. Open source tools, including Icarus Verilog [48] and GTKWave [24] were used throughout development whenever proprietary (FPGA-specific, but free) tools were not required, as a result the hardware design and unit tests are defined entirely in human-readable and maintainable ASCII text.

The Frame Buffer module consisted of three independent frame buffers implemented using pairs of 4096-bit dual port SRAM. A round-robin multiplexing scheme permitted one buffer to be filled with data from the current camera frame while the remaining two buffers were read from by the cross-correlation pipeline. Data in each frame buffer was mirrored across two blocks of SRAM allowing for four simultaneous reads per cycle.

Due to resource constraints (*i.e.*, a limited number of gates, the absence of dedicated DSP/MAC hardware), efforts were made to minimize the amount of data that needed to be processed and stored. Figure 7-7 contains a diagram of the full 8-bit cross-correlation processor core's architecture. The overarching structure is that of a folded-pipeline, trading speed for compactness, though other pipelines are contained therein in order to meet timing requirements. The four parallel unsigned 16-bit multipliers were implemented as three-stage asynchronous buffered pipelines. Final adders were omitted from the multipliers, with the addition of multiplier outputs being performed by a pipelined array adder, which computed the inner sum of products expressed in (7.1). The outer

sum was implemented with a final 24-bit accumulator. A registered copy of the accumulator output was then passed to a 24-bit comparator, which identified the peak in the cross-correlation. The values of u and v which corresponded to the peak value were updated as needed. After completing the cross-correlation between a pair of frames, the final peak coordinates were latched to provide a stable register value to be ready by the microcontroller.

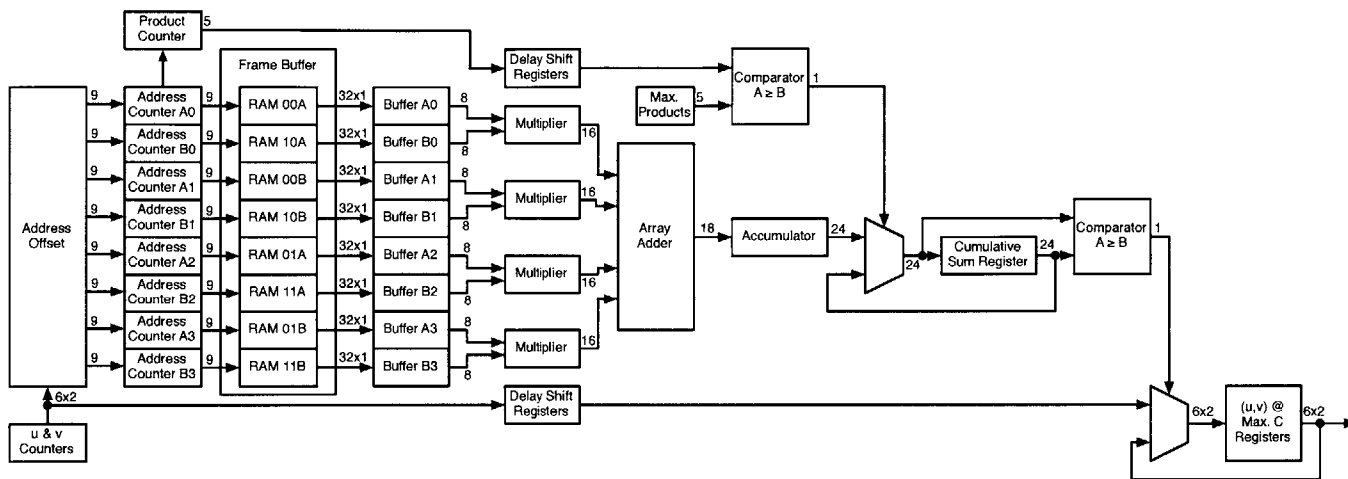


Figure 7-7: A 8-bit pipelined cross-correlation processor design.

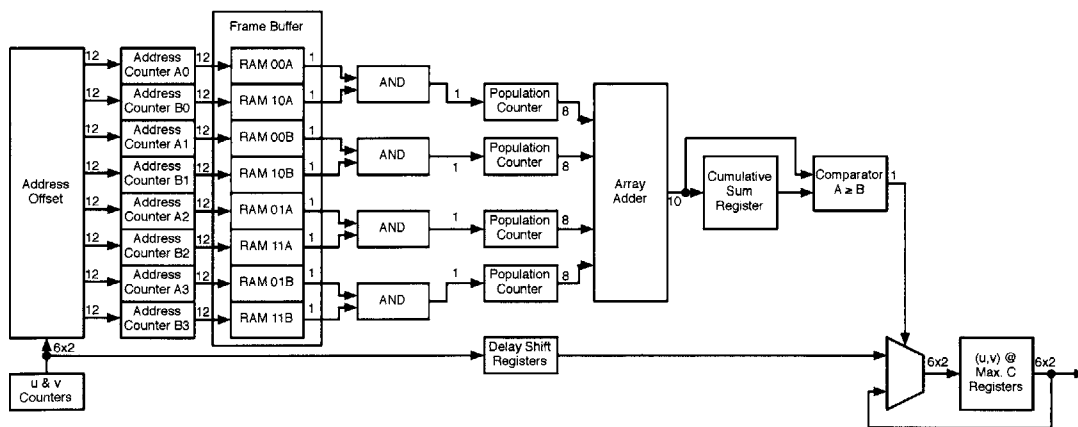


Figure 7-8: The binary cross-correlation pipeline, wherein expensive multipliers and adders have been replaced by AND gates and population counters.

Although a number of low-level optimizations and performance enhancing compromises were made, the 8-bit architecture still required a substantial number of logic elements, which effectively placed a lower limit on the size of the FPGA package (100-pin QFP, 13 mm × 13 mm), which was considered

to be relatively large in comparison to the rest of the subsystem components. An analysis of the pipeline modules was carried out in order to identify which ones might be suitable for pruning and rework. Unsurprisingly, it was found that the multiplication and addition stages required the most resources. Considering that a 1-bit multiplication may be implemented with a single AND gate, a simple yet elegant new implementation of the cross-correlation pipeline was designed. Rather than handling the full 8-bit pixel values, the revised design would instead process 1-bit representations, produced by applying a thresholding operation to the incoming data stream. The output from each of the four AND-gates comprising the multiplication stage were shifted into 8-bit wide registers. Four population counters quickly computed the number of 1's within each shift register, producing a 8-bit count values. The counts were then summed using a 10-bit array adder with an integral final adder, unlike its predecessor. The summation results were then stored in a register, for comparison with the current peak value.

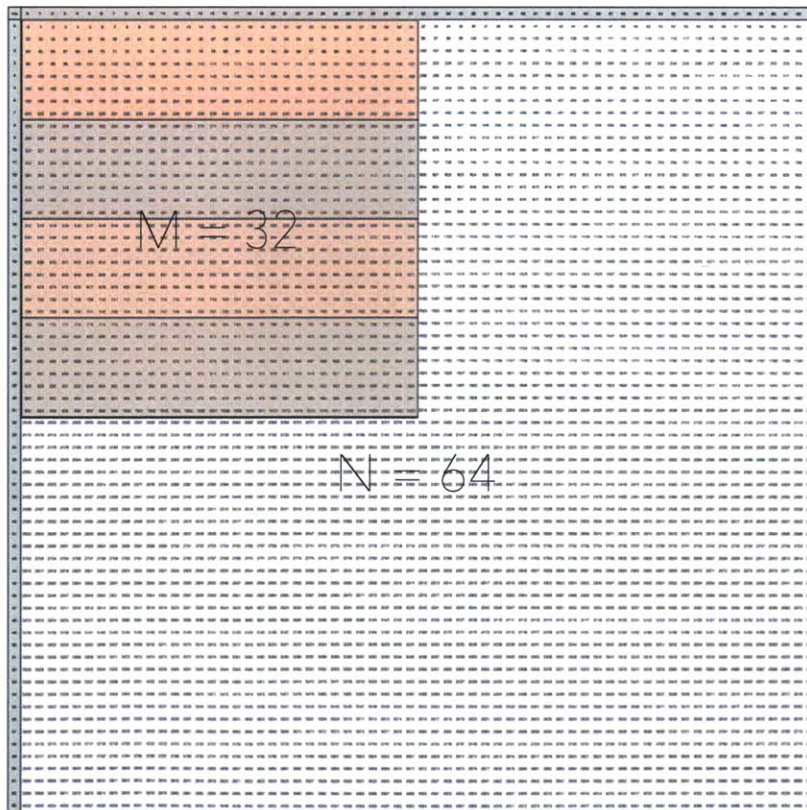


Figure 7-9: An $N \times N$ pixel frame and $M \times M$ pixel template shown with offset $u = v = 0$, corresponding with the start of a new cross-correlation computation.

Given a frame size of $N = 64$ pixels, template size of $M = 32$ pixels, as shown in Figure 7-9, the total number of shifts required in order to compute the cross-correlation would then be $P = N - M + 1 = 33$. Furthermore, the total number of reads per buffer per frame would be $P^2 M^2 / 4 = 278784$, where the factor of 4 in the calculation results from the use of four parallel hardware multipliers. For a core clock frequency of $f_{\text{core}} = 50$ Hz, the time to compute a single cross-correlation would be on the order of $T_{\text{xcorr}} \approx (P^2 M^2) / 4 f_{\text{core}} = 5.58$ ms, thus accommodating a frame rate of 179 Hz. As previously mentioned, the camera's maximum specified frame rate was 60 Hz, or $T_{\text{frame}} = 0.01\bar{6}$ s and the maximum pixel clock rate was limited to 27 MHz, resulting in 0.011 s of timing slack.

A hardware prototype was created, shown in Figure 7-10, as an incremental step towards producing a design that could be integrated with the existing ANT electronics. The processor was found to consume an average of 120 mW, resulting in an energy requirement of $0.407 \mu\text{J}/\text{pixel}$ for a 60 Hz frame rate.

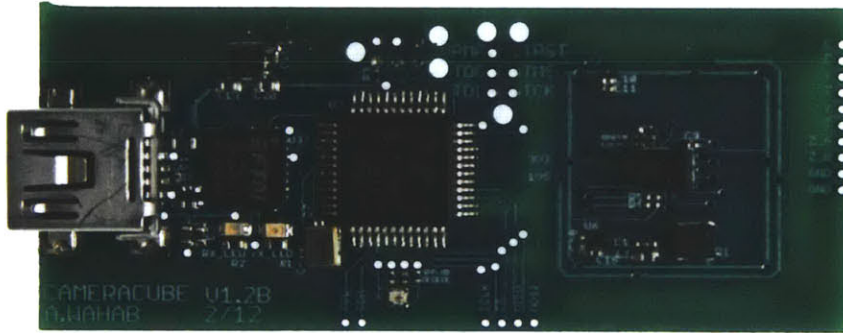


Figure 7-10: Imaging system hardware prototype (20 mm \times 50 mm). The camera module is located on the far right-hand side of the PCB. The FPGA is located on the reverse side, directly opposite the camera.

While the above approach would serve as a relative positioning scheme, it may be extended to allow for absolute positioning. Consider a workspace surface patterned with sufficiently small and spatially unique features. Given *a priori* knowledge of the aforementioned pattern design, cross-correlations performed between acquired frames of the workspace surface and the surface “map”.

THIS PAGE INTENTIONALLY LEFT BLANK

Chapter 8

Conclusions

The development of a microrobotic tool for micro/nanoscale positioning, a novel capacitive sensor, and a flexible, platform-independent software interface have been presented. The following sections provide a summary of key contributions along with some suggested directions for future work.

8.1 Contributions

Below is a brief summary of some noteworthy contributions that resulted from the ANTs project.

ANTs System An untethered mesoscale instrument capable of holonomic motion using legged locomotion with controllable step-size ranging from several micrometers to tens of nanometers. ANTs were designed with manufacturability in mind, with the goal of serving as a platform upon which low-cost alternatives to more expensive conventional laboratory instruments.

Fabrication Several hardware prototypes were designed and constructed for the purpose of demonstrating and refining various subsystem designs, fabrication techniques, and stepping performance.

Step Generation A simple approach to generating variable step size via frequency modulation was devised and implemented in hardware using compact and efficient circuit designs for generating and switching high voltages.

Stepping Characteristics A cursory examination of stepping resolution and performance provided empirical data, which corroborated with analytical and numerical models.

Capacitive Probe A novel capacitive sensor probe was realized. The design exploits emerging TDC technology as a single chip alternative to less efficient conventional multi-stage analog designs, which typically require excitation and measurement.

Positioning Several architectures for performing closed-loop positioning were described, including a distributed vision-based approach. A pair of specialized processors (8-bit and 1-bit) for performing hardware accelerated two-dimensional cross-correlations were designed, synthesized, and tested.

Server/UI Software An open-source, platform independent software interface was developed for control and data acquisition. A touch-enabled web-based UI was created in order to demonstrate system versatility and accessibility.

8.2 Next Steps: Considerations for Future Work

The aforementioned contributions are only the beginning. A number of suggested refinements and extensions to this body of work are listed below.

High-Voltage Supply The design of the high voltage supply electronics may be modified to permit low-frequency modulation of the output potential as an alternate means of adjusting step size and to reduce power consumption, especially when the desired step sizes are relatively small. The boost controller feedback voltage divider may be augmented with a digital potentiometer.

Adjusting the potentiometer set point would provide coarse control of the output potential set point over a limited range of voltages. Another option would be to connect the output terminal from a current-mode DAC to the boost controller feedback node, thus providing a means of biasing the feedback current. Alternatively, a voltage output multiplying DAC may be used to scale the feedback voltage divider output.

Bipolar Excitation A bipolar excitation scheme may be implemented to counter the effects of hysteresis inherent in piezoelectric materials, especially when ceramics with high voltage-strain coefficients are used (*e.g.*, PZT-5H). Two high voltage rails may be produced by either adding an inverting high voltage supply (*e.g.*, Ćuk converter) to the existing design, or by using a single flyback converter to generate both positive and negative rails. The latter would require the more modifications to the switching electronics in order to accommodate the presence of a floating ground.

Wireless Charging Highly integrated inductive charging controllers are now available (*e.g.*, Texas Instruments[®] BQ5101x/BQ5105x series) in ANT-compatible chip scale packages. The ability to wirelessly recharge the onboard battery would allow for extended, uninterrupted operations or even the possibility autonomous charging.

Time-of-Flight Positioning Time-of-Flight (TOF) measurements may be used to determine both position and orientation of one or more ANTs within a given workspace. One or more stationary beacons positioned along the periphery of the workspace envelope could emit either acoustic or optical pulses. A radial array of three or more MEMS microphones, or miniature photodetectors, equally spaced around the center of an ANT, paired with high-speed, high-resolution timers, much like the TDC used in this work, may be used to measure the propagation delay of the incident pulses. A comparison of the propagation delays among sensors within the array may be used to estimate a pulse's point of origin, and thus the position and origin of the ANT with respect to the beacon from which the pulse was emitted.

Atomic Force Microscope Active AFM cantilevers, which incorporate thermal or piezo actuation and integrated strain gauges [20, 21], may be used to functionalize ANTs for large format atomic force microscopy. Despite the high level of integration, such cantilevers still depend extensively on precision analog electronics to measure the minute levels of strain that result as the cantilever deflects while imaging. Replacing the analog circuitry with a single-chip TDC-based IC (*e.g.*, acam[®] PICO STRAIN) may result in a potentially more compact, lower power, solution.

System Integration The ANT design includes a relatively large number of parallel signals that require active control. When walking, communication, data acquisition, and positioning tasks are interrupted at high frequency in order to update the states of the high voltage switches. Migration of some, or all, control systems from a microcontroller to an FPGA would allow for uninterrupted, parallel execution of multiple functions. Aside from performance improvements and greater design flexibility, it is likely that a reduction in power consumption and part count may result.

Gaits Further study of gait design and efficiency would be informative. A means of programmatically generating leg excitation vectors could replace the predefined motion primitive vectors, allowing users to take full advantage of the platform's holonomic locomotion capability. Aside from being an interesting exercise in controls, such an implementation would likely extend the useful operating time between charges.

Adaptive Locomotion The three piezo electric legs could potentially be used to characterize the contact mechanics of the foot-surface interface. System identification techniques may be applied to relate, for example, the commanded leg deflections to the resulting body displacement. Stochastic system identification techniques may permit such experiments to be conducted while ANTs are online performing tasks. Insight garnered from such studies may be useful in optimizing stepping parameters according to work surface characteristics in order to maximize locomotion efficiency or positioning performance.

Closed-loop Position Control With only a moderate amount of effort, the positioning schemes described in this work may be implemented to permit fully-autonomous closed-loop control of one or more ANTs. Additionally, heading measurements obtained by the onboard IMU may be used to provide a more intuitive manual control scheme. When a user is manually controlling an ANT via a mobile handheld device containing an internal compass, positioning commands may be interpreted in a manner that the resulting motions are executed with respect to the user’s current orientation in space, rather than within the absolute frame of reference.

Active Instrument Axis The addition of an active “fourth leg” was previously considered in [35]; a fourth piezoelectric scanning tube extending below the body center would permit fine motions of an attached instrument. A flexure-based inchworm mechanism would allow the tube to extend and retract with respect to the work surface. A number of alternative designs were considered in this work (see Appendix B), though none were integrated into an ANT prototype.

THIS PAGE INTENTIONALLY LEFT BLANK

Appendix A

Tapped Inductor Boost Converter

The input/output voltage relationship for a tapped-inductor boost converter may be approximated via the following

$$\frac{V_{HV}}{V_{in}} = \frac{V_{in} t_{on}^2}{2T i_{out} L_p}, \quad (\text{A.1})$$

where V_{in} is the low voltage input, V_{HV} is the high voltage output (less the free-wheeling diode forward voltage drop), t_{on} is the input switch on time, T is the switching interval, i_{out} is the converter output current, and L_p is the primary winding inductance.

Figure A-1 contains time series representations of voltage and current within the two sets of inductor windings throughout one switching cycle. The winding ratio N is defined as the ratio of the number of secondary windings to the number of primary windings.

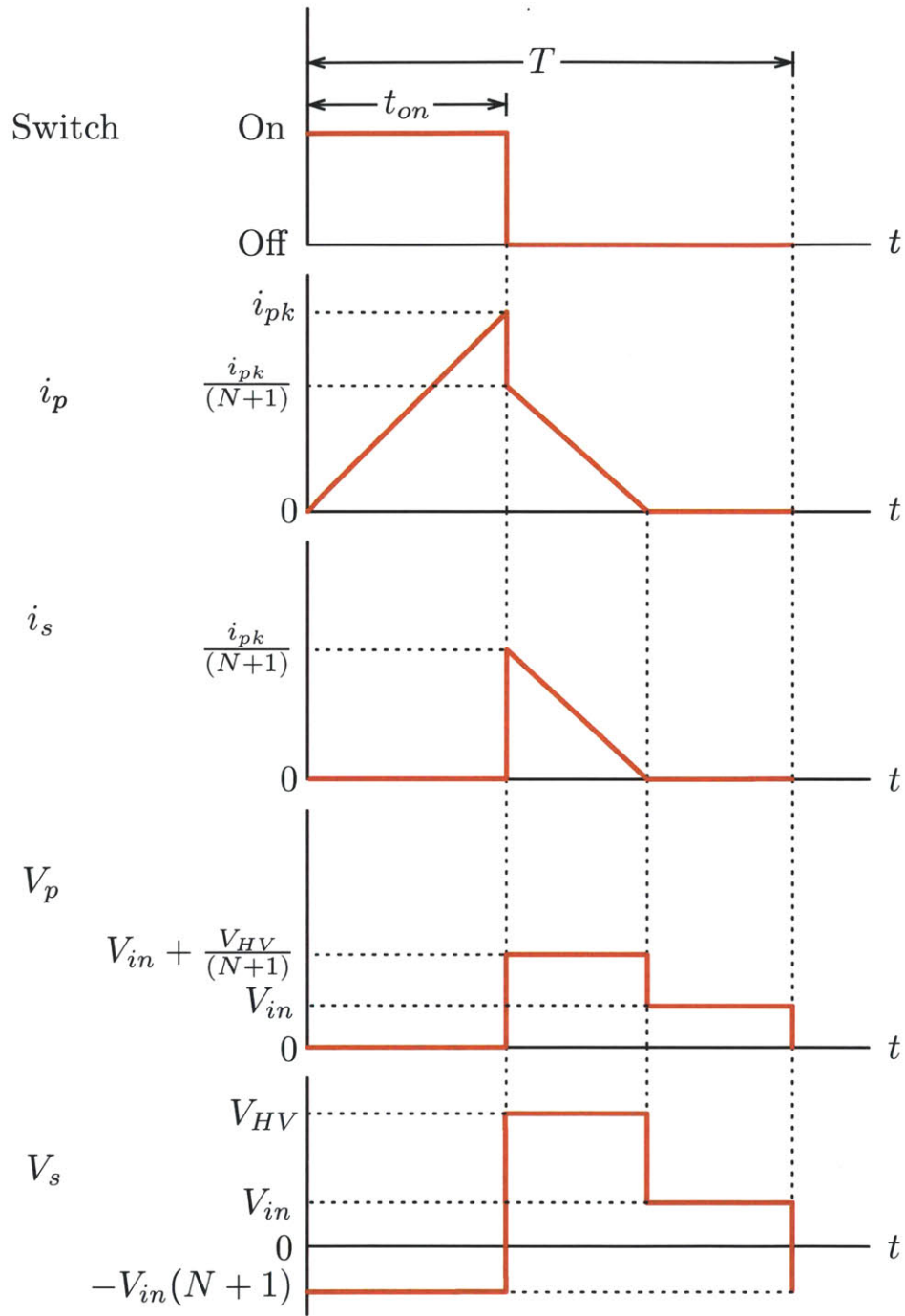


Figure A-1: Characteristic time series representations of primary inductor current i_p and voltage V_p and secondary inductor current i_s and voltage V_s during a single switch cycle at steady state. Adapted from [28].

Appendix B

Linear Actuator

B.1 Lorentz Force Linear Motor

A miniature Lorentz force linear motor was considered as a potential means of actuating the instrumentation axis. Concept designs consisted of a moving-coil wound around a thin-walled polyimide tube. A cylindrical permeant magnet, mounted in the center of a U-shaped steel field yoke, provided the bias magnetic field and served as a linear bearing for the coil. Simulation results (COMSOL Multiphysics[®]) of one geometry depicting the magnetic field flux density within the motor midplane is provided in Figure B-1.

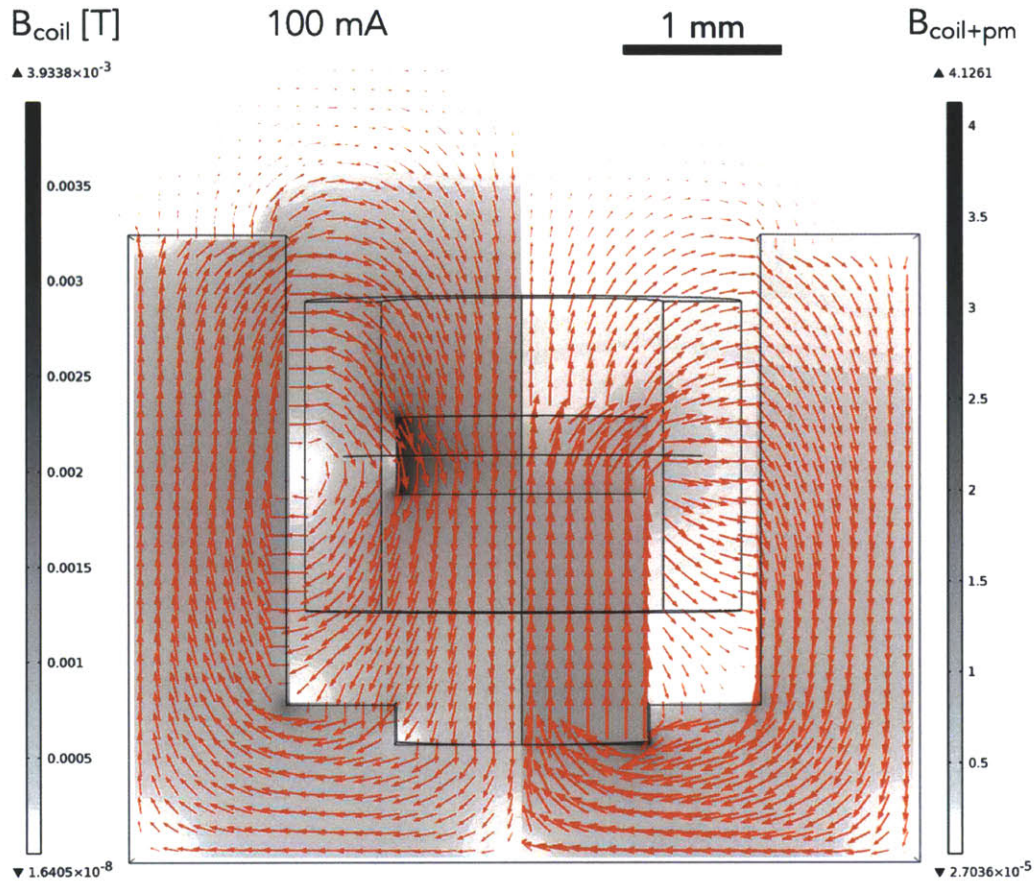


Figure B-1: Simulation results depicting the magnetic flux for a potential actuator geometry: C-frame (4 mm \times 5 mm \times 2 mm), cylindrical NdFeB magnet (N42, ϕ 1.5 mm). The left-hand side illustrated the flux density when a 100 mA current is passed through the coil.



Figure B-2: A collection of experimental coils wound to test various fabrication techniques and examine feasibility. The leftmost two coils were wound with 150 μ m diameter wire, while the two on the right were wound with 50 μ m diameter wire. A ϕ 1.5 mm permanent magnet is included on the left-hand side for scale.

Appendix C

ANT Revision 1K Schematic

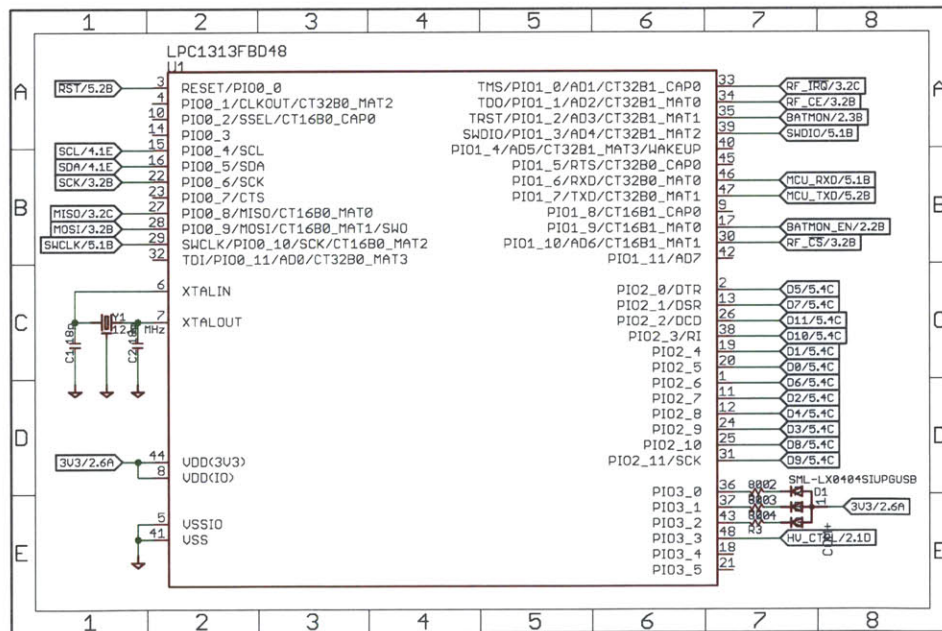


Figure C-1: Microcontroller, oscillator, and LEDs.

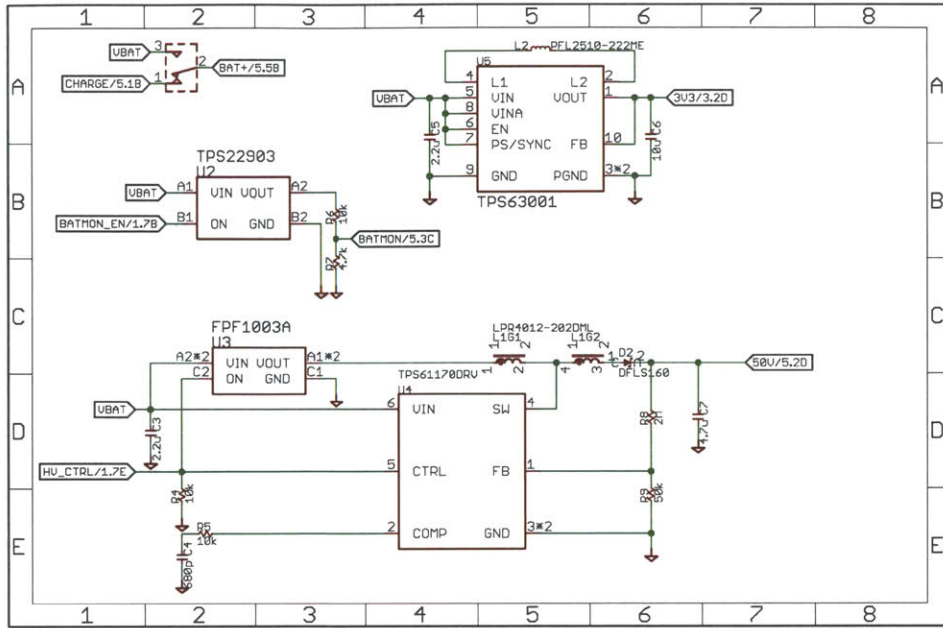


Figure C-2: Switching regulators and load switches.

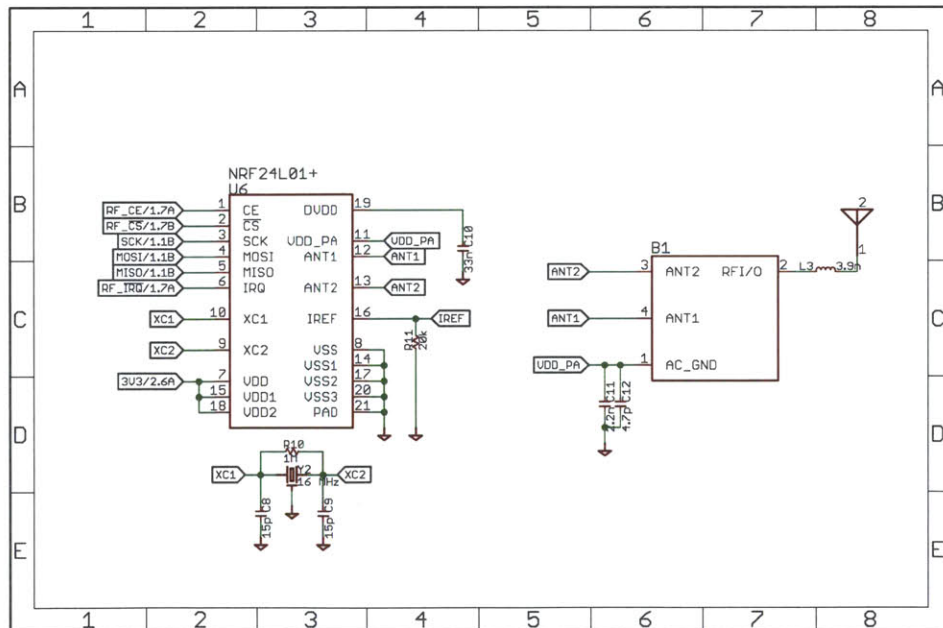


Figure C-3: Radio transceiver.

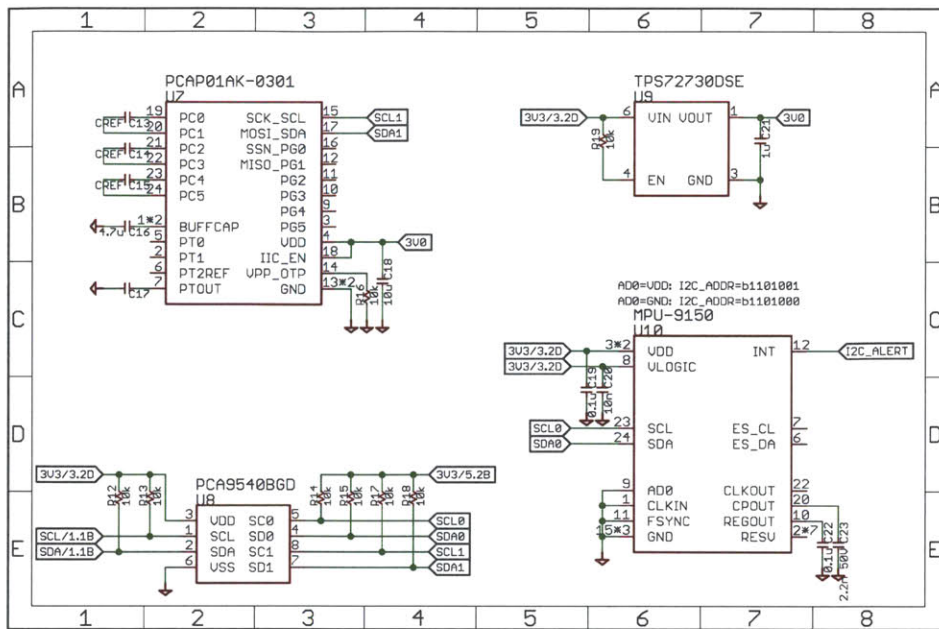


Figure C-4: IMU, I²C switch, CDC, and regulator.

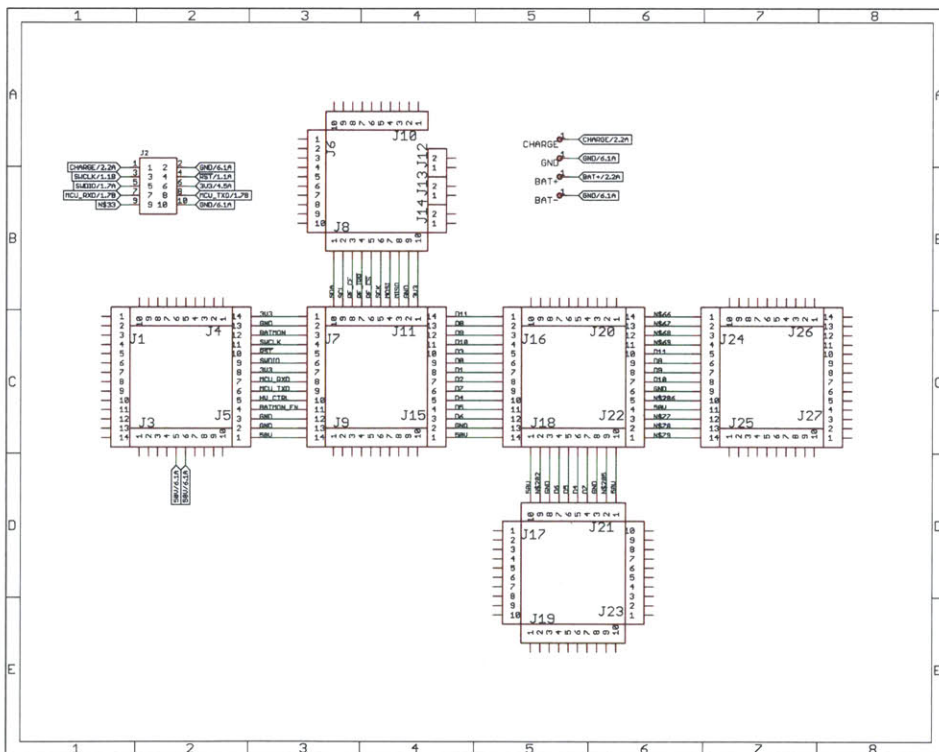


Figure C-5: PCB module interconnects.

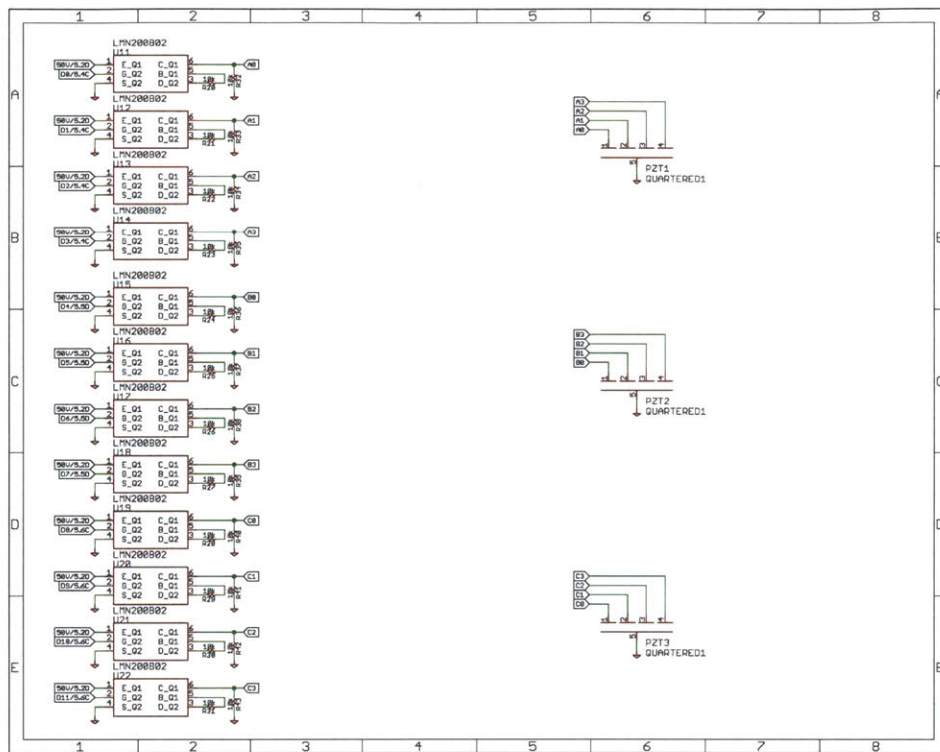


Figure C-6: High voltage switches and piezoelectric load connections.

Bibliography

- [1] IEEE Standard on Piezoelectricity. *ANSI/IEEE Std 176-1987*, 1988.
- [2] Socket.io. <http://socket.io>, 2012.
- [3] COMSOL multiphysics. <http://www.comsol.com>, 2013.
- [4] IAR embedded workbench for ARM. <http://www.iar.com>, 2013.
- [5] jQuery. <http://jquery.com>, 2013.
- [6] jQuery mobile. <http://jquerymobile.com>, 2013.
- [7] MATLAB. <http://www.mathworks.com>, 2013.
- [8] node-serialport. <https://github.com/voodootikigod/node-serialport>, 2013.
- [9] node.js. <http://nodejs.org>, 2013.
- [10] H. Adriaens, W. L. De Koning, and R. Banning. Modeling piezoelectric actuators. *Mechatronics, IEEE/ASME Transactions on*, 5(4):331–341, Dec 2000.
- [11] H. Aoyama and O. Fuchiwaki. Flexible micro-processing by multiple microrobots in sem. In *Proceedings of the IEEE International Conference on Robotics and Automation*, volume 4, pages 3429–3434, 2001.
- [12] APC International, Ltd. *Piezoelectric Ceramics: Principles and Applications*. Second edition, 2011.
- [13] K.-H. Besocke. Kinematic arrangement for the micro-movements of objects, November 1988.
- [14] J.-M. Breguet, S. Johansson, W. Driesen, and U. Simu. A review on actuation principles for few cubic millimeter sized mobile micro-robots. In *Proceedings of the 10th International Conference on New Actuators (Actuator 2006)*, pages 374–381, 2006.
- [15] CadSoft. CadSoft EAGLE PCB design software. <http://www.cadsoftusa.com>, 2013.
- [16] C. J. Chen. Electromechanical deflections of piezoelectric tubes with quartered electrodes. *Applied Physics Letters*, 60(1):132–134, January 1992.

- [17] A. K. Eigoli and G. Vossoughi. Dynamic modeling of stick-slip motion in a legged, piezoelectric driven microrobot. *International Journal of Advanced Robotic Systems*, 7(3):201–208, 2010.
- [18] EL-CAT Inc. Properties of silicon and silicon wafers. <http://www.el-cat.com/silicon-properties.htm>, 2013.
- [19] O. M. El Rifai and K. Youcef-Toumi. Modeling of piezoelectric tube actuators. *Innovation in Manufacturing Systems and Technology (IMST)*, January 2004. Found on DSpace@MIT.
- [20] G. E. Fantner, D. J. Burns, A. M. Belcher, I. W. Rangelow, and K. Youcef-Toumi. Dmcmn: In depth characterization and control of afm cantilevers with integrated sensing and actuation. *Journal of Dynamic Systems, Measurement, and Control*, 131, November 2009.
- [21] G. E. Fantner, W. Schumann, R. J. Barbero, A. Deutschinger, V. Todorov, D. S. Gray, A. M. Belcher, I. W. Rangelow, and K. Youcef-Toumi. Use of self-actuating and self-sensing cantilevers for imaging biological samples in fluid. *Nanotechnology*, 20, October 2009.
- [22] S. Fatikow, C. Edeler, C. Diederichs, M. I., and D. Jasper. Design and control of a nanohandling robot. In *13th World Congress in Mechanism and Machine Science*, June 2011.
- [23] R. S. Fearing. Powering 3 dimensional microrobots: Power density limitations. In *IEEE International Conference on Robotics and Automation*, May 1998.
- [24] U. Finkelstein, K. E. Fleming, D. Baltus, T. Gingold, T. Sailer, and A. Hidyat. Gtwave. <http://gtkwave.sourceforge.net>, 2013.
- [25] I-SWARM Consortium. Periodic activity report. Technical Report 3, Information Society Technologies Project No. 507006, July 2007.
- [26] I-SWARM Consortium. Periodic activity report. Technical Report 4, Information Society Technologies Project No. 507006, May 2008.
- [27] K. Johnson. *Contact Mechanics*. Cambridge University Press, 1985.
- [28] M. Karpelson, G.-Y. Wei, and R. J. Wood. Milligram-scale high-voltage power electronics for piezoelectric microrobots. In *Robotics and Automation, 2009. ICRA '09. IEEE International Conference on*, pages 2217–2224, 2009.
- [29] J. Kim, B. L. Grisso, J. K. Kim, D. S. Ha, and D. J. Inman. Electrical modeling of piezoelectric ceramics for analysis and evaluation of sensory systems. *IEEE Sensors Applications Symposium*, pages 122–127, February 2008.
- [30] S. Martel. Cooling strategies for high performance miniature wireless robots designed to operate at the nanoscale. *Nanotechnology, 2003. IEEE-NANO 2003. 2003 Third IEEE Conference on*, 1:148–151 vol.2, 2003.
- [31] S. Martel. Special surface for power delivery to wireless micro-electro-mechanical systems. *Journal of Micromechanics and Microengineering*, 15(10):251–258, 2005.

- [32] S. Martel and I. Hunter. Nanofactories based on a fleet of scientific instruments configured as miniature autonomous robots. *Journal of Micromechatronics*, 2:201–214, December 2002.
- [33] S. Martel, A. Schindler, G. Baumann, S. Riebel, and T. Boitani. Cooling platform for an automated nanofactory based on a fleet of miniature robots designed for atomic scale operations. *Automation*, September 2003.
- [34] S. M. Martel and I. W. Hunter. Piezo-drive circuits for amplitude-modulated locomotion for miniature wireless robots. *Microrobotics and Microassembly III*, 4568(1):199–209, October 2001.
- [35] S. M. Martel, T. Koker, and I. W. Hunter. Main design issues for embedding onto a wireless miniature robot a scanning tunneling positioning system capable of atomic resolution over a half-meter-diameter surface area. *Microrobotics and Microassembly III*, 4568(1):68–77, October 2001.
- [36] S. M. Martel, T. Koker, S. Riebel, M. Sherwood, J. Suurkivi, and I. W. Hunter. Infrastructure suited for supporting a fleet of wireless miniature robots designed for atomic-scale operations. *Microrobotics and Microassembly III*, 4568(1):221–230, October 2001.
- [37] S. M. Martel, P. G. Madden, L. Sosnowski, I. W. Hunter, and S. Lafontaine. Nanowalker: a fully autonomous highly integrated miniature robot for nanoscale measurements. *Microsystems Metrology and Inspection*, 3825(1):111–122, September 1999.
- [38] S. M. Martel, O. Roushdy, M. Sherwood, and I. W. Hunter. High-resolution optical positioning system for miniature instrumented robots. *Microrobotics and Microassembly II*, 4194(1):121–128, October 2000.
- [39] MiCRoN Consortium. Public final report: MiCRoN. Technical report, IST-2001-33567, February 2006.
- [40] Microsemi. Libero SoC. <http://www.microsemi.com>, 2013.
- [41] Moser Company. Technical data properties of synthetic sapphire and ruby. <http://www.mosercompany.com/saphirespec.htm>, 2013.
- [42] T. Ozyagcilar. Implementing a tilt-compensated ecompass using accelerometer and magnetometer sensors. Technical Report AN4248, Freescale Semiconductor, 01 2012.
- [43] M. G. Rozman, M. Urbakh, and J. Klafter. Stick-slip dynamics of interfacial friction. *Physica A: Statistical and Theoretical Physics*, 249(1-4):184–189, 2 1998.
- [44] F. Schmoeckel and S. Fatikow. Smart flexible microrobots for scanning electron microscope (sem) applications. *Journal of Intelligent Material Systems and Structures*, 11(3):191–198, 3 2000.
- [45] P. Smith. Comparisons between low power wireless technologies. White paper, CSR, May 2011.

- [46] D. Systèmes. Solidworks. <http://www.solidworks.com>, 2013.
- [47] N. Vazquez, L. Estrada, C. Hernandez, and E. Rodriguez. The tapped-inductor boost converter. In *Industrial Electronics, 2007. ISIE 2007. IEEE International Symposium on*, pages 538–543, 2007.
- [48] S. Williams. Icarus verilog. <http://iverilog.icarus.com>, 2013.
- [49] H. Zhang, S.-y. Zhang, and L. Fan. Effects of stick-slip motions on besocke-style scanners in scanning probe microscopes. *Journal of Physics D: Applied Physics*, 45(3):035303, 2012.

